NASA Technical Paper 2088

January 1983

Semiconductor Photoelectrochemistry

A. Martin Buoncristiani
and Charles E. Byvik

NASA

NASA
Technical
Paper
2088

1983

Semiconductor Photoelectrochemistry

A. Martin Buoncristiani
Christopher Newport College
Newport News, Virginia

Charles E. Byvik
Langley Research Center
Hampton, Virginia

NASA
National Aeronautics
and Space Administration

**Scientific and Technical
Information Branch**

CONTENTS

1. SUMMARY

The photoelectrochemical effects that occur at an illuminated semiconductor-liquid interface may provide a unique means of energy conversion and storage. A semiconducting electrode illuminated by light with energy greater than the semiconductor bandgap energy may induce a chemical reaction among the constituents of the interfacial region. A model of the charge transport processes in the semiconductor is presented in this report. This model is based upon semiconductor device theory, and it incorporates, in an essential way, the nonlinear processes characterizing the diffusion and reaction of charge carriers in the semiconductor. The model is used to study conditions limiting useful energy conversion, specifically the saturation of current flow due to high light intensity. Numerical results describing charge distributions in the semiconductor and its effects on the electrolyte are obtained.

Results of experimental efforts are also summarized. These results include the following:

1. An estimate based on experiments of the maximum rate at which a semiconductor photoelectrode is capable of converting electromagnetic energy into chemical energy

2. The effect of cell temperature on the efficiency of a photoelectrochemical cell

3. A method for determining the point of zero zeta potential (pzzp) for macroscopic semiconductor samples

4. A new technique using platinized titanium dioxide powders and ultraviolet radiation to produce chlorine, bromine, and iodine from solutions containing their respective ions

5. The results of experiments characterizing a new class of layered compounds called transition-metal thiophosphates for use as photoelectrodes in photoelectrochemical cells

6. A discussion of a technique used to produce high conversion efficiency from laser radiation to chemical energy.

2. INTRODUCTION

In 1972, Fujishima and Honda (refs. 1 and 2) demonstrated that sunlight, incident upon an n-TiO_2 electrode, would catalyze the electrolysis of water. This research stimulated much more study (refs. 3 through 7) of the photoelectrochemical processes occuring at a semiconductor-electrolyte interface and led to the discovery of a variety of useful chemical reactions stimulated at the surface of a photosensitive electrode. There is a growing body of evidence to suggest the possibility of developing a semiconductor electrode device capable of converting radiant energy into electrical energy or into a chemical fuel. If such a device could operate efficiently and on a large scale, there would be important applications both on Earth and in space. Specifically, there may be some unique applications of these devices in

the environment of space, where they can be used as a power supply or as part of a propulsion system. One particularly interesting concept is that hydrogen and oxygen produced from solar radiation by a semiconducting electrode cell may be used to replenish the stores of these chemicals consumed in a fuel cell. This would provide a closed-cycle solar-energy system. It is also interesting to conceive of this type of cell as a receptor of energy transmitted from one point in space to another by a laser beam as part of a space energy-distribution network.

Figure 1 is a representation of a semiconductor-electrode electrochemical cell. The critical element in such a cell is the combination of the photosensitive semiconductor electrode and the semiconductor-electrolyte interfacial region. It is within this region that the incident photon energy is transferred through various energy levels in the semiconductor and in the electrolyte, until it eventually appears in a useable form as chemical or electrical energy. The overall process of converting the incident radiant energy to its final form is the result of a series of simpler processes of a physical or chemical nature. In order to understand the operation of a complete photoelectrochemical cell, it is necessary to understand the individual processes which occur, as well as the way each of the separate processes affect each other. In this report, a theoretical treatment of the relevant processes taking place within the semiconductor electrode and at its interface with the electrolyte is described. This treatment is based upon a rigorous application of the macroscopic theory of charge generation, recombination, and transport in semiconductors. The equations which are derived for charge transport in a semiconductor electrode are nonlinear. Therefore, an exact solution was not obtained. A systematic procedure for obtaining approximate solutions to them are developed, and numerical results based upon the approximations are presented. The previous theoretical work was developed from a linearized theory. There is an inherent limitation in this approach, in that results from the linearized theory do not apply in all situations. There are some circumstances where the nonlinearity of the processes is important, and one can hope to glean some information about these circumstances from the more rigorous development presented herein. Treatment of the saturation of photoeffects in the semiconductor at high light intensity is one illustration of this point. An alternative method for discussing the transport of excess charge carriers is presented in references 7 and 8. It should also be noted that although the specific case of a semiconductor electrode is addressed, the theory developed herein is applicable, with minor modifications, to other semiconductor devices.

The major regions of interest within an electrochemical cell are shown in the schematic in figure 1. The phenomena responsible for photostimulated catalysis or for the production of electricity in a semiconductor-electrode cell are controlled by processes taking place in the semiconductor-electrolyte interfacial region. A detailed and thorough understanding of all these interrelated processes is lacking at present, but the following description provides a sketch of the probable events occurring in the interfacial region. When a semiconductor electrode is brought into contact with an electrolyte, there is a redistribution of the mobile charge within the semiconductor and of the ionic charge within the electrolyte. These redistributions result in a steady-state space-charge distribution throughout the interfacial region. The space-charge distribution within the electrolyte interfacial region has been studied extensively (refs. 9 through 12) and can be described adequately by the Gouy-Chapman-Stern theory of ionic-charge distribution at solid-liquid interfaces. The extent of this charge distribution and the net charge contained in it determine the net charge on the semiconductor. The space-charge distribution within the semiconductor is the source of an electric field near the surface, and this field plays an important role in the photosensitivity of the cell. Illumination of the semiconductor by light of sufficiently high energy produces electron-hole pairs in the semi-

conductor. These pairs are then separated by this space-charge field. Part of the photoproduced charge is drawn to the surface of the semiconductor, where it can interact (via electron transfer) with the electrolyte. This interaction causes a chemical reaction among the constituents of the interfacial region.

The effect of the redistribution of charge in the semiconductor electrode when it is placed in contact with the solution is to produce an electric field near the surface. This field gradient alters the semiconductor energy bands near the surface (ref. 13). If the electrode and the electrolyte are placed in contact, the energy levels are as shown in figure 2(a). This figure illustrates the case of an n-type semiconductor electrode. The Fermi energy of the electrolyte $E_{F,REDOX}$ (chemical potential) is determined by the solvent and the ionic species in it. When the semiconductor electrode and the electrolyte are placed in contact, there is a readjustment in charge which brings the two Fermi energy levels together at a value extremely close to $E_{F,REDOX}$. The surface values of the conduction band edge E_C and the valence band edge E_V remain fixed, and the final energy-band picture is shown in figure 2(b). An important special value of $E_{F,REDOX}$ is that for which the band bending is zero, the flat band energy $E^0_{F,REDOX}$. The difference between $E^0_{F,REDOX}$ and $E_{F,REDOX}$ is the amount of band bending induced by the electrolyte. By using this band-bending picture, the operation of a photoelectrochemical cell can be represented as in figure 3. A photon, absorbed by the semiconductor, promotes an electron from the valence band to the conduction band and leaves a hole in the valence band. The photoproduced charges are separated by the semiconductor space-charge field. The electron moves through the bulk of the semiconductor to the external circuit, and the hole moves to the surface, where it can interact with the electrolyte in an oxidation reaction. The current due to the electron motion through the circuit is compensated by an ionic current in the electrolyte to the counter electrode, where it participates in a reduction reaction.

The electronic states of ions in solution can be represented as electron energy levels, subject to fluctuations in time due to the thermal motions of polar molecules in the solution (ref. 14). Thus, there are at least two broadened electronic levels in the electrolyte corresponding to redox reactions within the cell. There may be additional energy levels corresponding to electronic states within the semiconductor. One level represents the energy of dissociation, E_D, and the other levels may represent possible surface states. All these energy levels in the interfacial region are shown in figure 4. Although some semiconductor-electrode electrochemical cells may produce relatively large photocurrents, others decompose irreversibly because of the redox reactions at their surface. This decomposition occurs when the energy of dissociation E_D is more negative than $E_{F,REDOX}$, so that the dissolution of the electrode is energetically possible. The electrode shown in figure 4 will not dissolve. There are certain semiconducting metal-oxide photoelectrodes that are inherently stable (refs. 3 through 5). Unfortunately, some of the stable semiconducting photoanode materials (TiO_2 and $SrTiO_3$, e.g.) have bandgaps so large that only ultraviolet radiation ($\approx$3 percent of the solar spectrum) is absorbed. However, the energy conversion efficiency (photo-to-chemical) is quite high. It has been found recently that an appropriate electrolyte often stabilizes semiconducting electrodes that were thought to be unstable (ref. 3). Consequently, electrodes with better response to the solar spectrum might be developed. These stabilized semiconductor-electrolyte junctions have not yet stimulated electrolysis.

3. SYMBOLS

A	cross-sectional area of electrode, m^2; also a matrix of constants, s^{-2}
a	dimensionless parameter characterizing bulk concentrations of electrons and holes in semiconductors; also an arbitrary parameter
B	numerical index
c	speed of light, $m\text{-}s^{-1}$
D	matrix with diffusion coefficients as elements, $m^2\text{-}s^{-1}$
D_n	diffusion coefficient for electrons, $m^2\text{-}s^{-1}$
D_p	diffusion coefficient for holes, $m^2\text{-}s^{-1}$
E	energy, eV
EA	electron affinity, eV
E_A	energy level of an acceptor atom, eV
E_A^*	effective ionization energy of an acceptor atom referred to vacuum energy, eV
E_C	lowest energy in conduction band, eV
E_D	energy of dissociation, eV
E_D^*	effective ionization energy of a donor atom referred to vacuum energy, eV
E_F	Fermi energy in a semiconductor, eV
$E_{F,I}$	Fermi energy of an intrinsic semiconductor, eV
$E_{F,REDOX}$	Fermi energy in electrolyte at flatband condition, eV
E_G	bandgap energy, eV
E_I	energy of bent bands, eV
E_I^*	effective energy of bent bands, eV
E_{ph}	photon energy, eV
E_s	energy level of single electronic state, eV; also magnitude of electric field strength at semiconductor surface, $V\text{-}m^{-1}$
E_s^*	effective energy level of single electronic state, eV
E_{SS}	energy of surface states, eV
E_V	highest energy in conduction band, eV

$E(k)$ electronic energy, eV

$E(x)$ electric field strength, $V\text{-}m^{-1}$

e electronic charge, C

FF fill factor, dimensionless

F_n net source of electrons, $m^{-3}\text{-}s^{-1}$

F_p net source of holes, $m^{-3}\text{-}s^{-1}$

$F(u)$ matrix with elements giving net source of charge carriers in a semiconductor, $m^{-3}\text{-}s^{-1}$

$F_{1/2}( )$ Fermi integral, dimensionless

$F( )$ Fermi distribution, dimensionless

G_n net rate of generation of electrons, $m^{-3}\text{-}s^{-1}$

G_p net rate of generation of holes, $m^{-3}\text{-}s^{-1}$

g number of degenerate states of a vacant electronic level

g^* number of degenerate states of an occupied electronic level

g_{I_0} rate of photoinduced generation of charge carriers, $m^{-3}\text{-}s^{-1}$

g_0 rate of thermal generation of charge carriers, $m^{-3}\text{-}s^{-1}$

$H(,)$ first integral of Poisson-Boltzmann equation, dimensionless

h Planck constant, eV-s

I electric current, A

$I( )$ matrix giving inhomogeneous part of transport equation, $C\text{-}s\text{-}m^{-2}$

I_n inhomogeneous term in transport equation for electrons, $C\text{-}m^{-4}$

I_p inhomogeneous term in transport equation for holes, $C\text{-}m^{-4}$

I_{ph} photocurrent, A

I_0 intensity of incident light, $m^{-2}\text{-}s^{-1}$

$I_{0,s}$ saturation level of incident light intensity, $m^{-2}\text{-}s^{-1}$

J_n electron current density, $C\text{-}m^{-2}\text{-}s^{-1}$

J_p hole current density, $C\text{-}m^{-2}\text{-}s^{-1}$

J_u current density due to absorption in the Urbach region, $C\text{-}m^{-2}\text{-}s^{-1}$

k	Boltzmann constant, $J\text{-}K^{-1}$; also particle wave number, m^{-1}
L_D	Debye length, m
L_n	electron diffusion length, m
L_p	hole diffusion length, m
L_∞	effective Debye length, m
$\ell(\ )$	linear functional
m^*	effective mass, kg
m_n^*	electron effective mass, kg
m_p^*	effective hole mass, kg
NHE	normal hydrogen electrode
N_A	concentration of acceptor atoms, m^{-3}
N_C	conduction band concentration factor, m^{-3}
N_D	concentration of donor atoms, m^{-3}
N_V	valence band concentration factor, m^{-3}
n	electron concentration, m^{-3}
n_b	bulk value of electron concentration, m^{-3}
n_D	concentration of electrons in donor atoms, m^{-3}
n_i	intrinsic concentration, m^{-3}
p	hole concentration, m^{-3}
p_A	concentration of holes in acceptor atoms, m^{-3}
p_b	bulk value of hole concentration, m^{-3}
$Q^{\pm}$	surface charge excess, $C\text{-}m^{-2}$
q	electronic charge, C
R	gas constant, $J\text{-}kmol^{-1}\text{-}K^{-1}$
R_n	rate of recombination of electrons, $m^{-3}\text{-}s^{-1}$
R_p	rate of recombination of holes, $m^{-3}\text{-}s^{-1}$
SC	semiconductor
SCE	saturated calomel electrode

T	temperature, K
t	time, s
u	normalized electron energy, dimensionless; also matrix with charge carrier concentration as elements, m^{-3}
u_b	bulk value of normalized electron energy, dimensionless
$u_0, u_1, \ldots$	iterated solutions to transport equation, m^{-3}
V	potential difference, V
V_{app}	applied potential difference, V
V_{bb}	potential of bent bands, V
V_{ext}	potential supplied by external source, V
V_F	potential of the Fermi level, V
V_{FB}	flatband potential, V
V_H	potential across Helmholtz layer, V
V_n	electron velocity, $m\text{-}s^{-1}$
V_{op}	onset potential, V
V_p	hole velocity, $m\text{-}s^{-1}$
V_{prod}	difference in redox potential of half-cell reactions, V
V_s	surface potential, eV
V_0	surface potential, V; also redox level for hydrogen, V
V_∞	bulk potential, eV
W	depletion width, m
X, X_0	dimensionless parameters
x	distance within semiconductor, m
y	penetration parameter, dimensionless
$y_{1/2}$	special value of penetration parameter, dimensionless
α	absorption length for incident radiation, m^{-1}
α_n	electron drift parameter, m^2
α_p	hole drift parameter, m^2

α_0	Urback absorption length, m^{-1}
β	thermal energy factor, $C\text{-}J^{-1}$
Δ	normalized electron potential, dimensionless
ΔE	change in energy, J
Δ_{FC}	position of Fermi level with respect to the conduction band edge, J
ΔG	change in Gibbs free energy, J
ΔT	change in temperature, K
ΔV	change in potential, V
ΔV_{FB}	change in flatband potential, V
δ	normalized electron energy, dimensionless
ε	electrostatic permativity, $V^{-1}\text{-}m^{-1}$
$\varepsilon_1, \varepsilon_2$	numerical parameters
η	electrochemical cell efficiency, dimensionless
η_{max}	maximum value of electrochemical cell efficiency, dimensionless
λ	wavelength, m; also a dimensionless parameter
μ	chemical potential, eV; also drift mobility, $m^2\text{-}V^{-1}\text{-}s^{-1}$
μ_n	electron drift mobility, $m^2\text{-}V^{-1}\text{-}s^{-1}$
μ_p	hole drift mobility, $m^2\text{-}V^{-1}\text{-}s^{-1}$
ν	photon frequency, Hz
ρ	charge distribution, $C\text{-}m^{-3}$
$\rho_C(E)$	density of electronic states in the conduction band, $m^{-3}\text{-}eV^{-1}$
$\rho_V(E)$	density of electronic states in the valence band, $m^{-3}\text{-}eV^{-1}$
τ_n	electron lifetime, s
τ_p	hole lifetime, s
ϕ	electrostatic potential, V
ϕ_b	bulk value of electrostatic potential, V

χ electron affinity, eV

ω_n electron transport parameter, dimensionless

ω_p hole transport parameter, dimensionless

Prime indicates derivative with respect to x.

An arrow over a symbol indicates a vector quantity.

4. SPACE-CHARGE DISTRIBUTION IN A SEMICONDUCTOR ELECTRODE

4.1 General Description of Electrode

In this section, a foundation is laid for a semiclassical analysis of the physical processes occurring in an illuminated semiconductor electrode. The basic system under investigation is depicted in figure 5, which schematically represents the semiconductor-electrolyte interfacial region. The presence of ionic charge in the electrolyte and possibly a distribution of charge on the semiconductor surface cause the mobile charge within the semiconductor interfacial region to be displaced, leaving a distribution of fixed ionic charge. These distributions of fixed and mobile charges near the semiconductor surface are the source of an electrostatic field. In the sections which follow, we examine the form of this field and subsequently study the role of this field in the photoeffects occurring at the junction. The assumptions which underlie our analysis are as follows:

1. The semiconductor is a single-crystal cylinder with one base plane of surface area A in contact with the electrolyte and with the opposite base plane in ohmic contact with the metallic counter electrode of the cell. The diameter of the crystal base is much larger than the crystal thickness. Thus, the variables that characterize the electrical properties of the crystal depend upon a single spatial parameter, the depth from the semiconductor-liquid junction. An n-type semiconductor is assumed; this is most frequently the case in practice. It is a simple matter to adjust the results to apply to a p-type material.

2. The doping of the semiconductor is attributed to a concentration of acceptor and donor ions N_A and N_D distributed uniformly throughout the crystal. Furthermore, the separation between acceptor and donor ions is large enough to be able to ignore interaction between ions. On the other hand, the spacing between acceptor and donor ions is small enough, compared with the space-charge penetration depth, that the discrete ionic-charge distribution can be represented as a continuous distribution.

3. If a surface state is charged, it resides on the surface and not within the semiconductor. This implies that the space-charge distribution is caused by fixed ionic charge and mobile charge carriers only.

4. The semiconductor is nondegenerate; that is, the Fermi energy differs from the conduction and valence band energies by at least 3kT. This assumption is discussed more fully in the appendix. The most prominent effect of this assumption is

that the concentration of electrons and holes can be described by a Boltzmann distribution. Namely, the concentration of electrons is given by

$$n = N_C \exp\left(-\frac{E_C - E_F}{kT}\right) \tag{4.1}$$

where

$$N_C = 2\left(\frac{2\pi m_n^* kT}{h^2}\right)^{3/2}$$

and the concentration of holes is given by

$$p = N_V \exp\left[-\frac{(E_F - E_V)}{kT}\right] \tag{4.2}$$

where

$$N_V = 2\left(\frac{2\pi m_p^* kT}{h^2}\right)^{3/2}$$

If the semiconductor is maintained in thermal equilibrium, the Fermi energy E_F maintains a constant value at all points. Consequently, if the concentration of carriers n and p changes from point to point in the semiconductor as it does near the semiconductor electrolyte junction, this variation must mean a local change in E_C and E_V. That is, the energy bands are bent. This bending is represented schematically in figure 6, which depicts the band bending of an n-type semiconducting electrode. The band bending is a result of various mobile charges in the junction region coming into electrostatic equilibrium. This charge distribution is described in the following section.

4.2 Derivation of Conditions of Electrostatic Equilibrium - Poisson-Boltzmann Equation

Let the uniform concentration of acceptor and donor atoms be represented by N_A and N_D, respectively. Assume that these atoms are completely ionized, a circumstance readily satisfied at room temperature. (See appendix.) Then, if $n(x)$ and

$p(x)$ represent the carrier concentrations as a function of depth in the semiconductor, the net charge distribution within the semiconductor is given by

$$\rho(x) = e\left[p(x) - n(x) + N_D - N_A\right] \tag{4.3}$$

Deep within the semiconductor, the charge carrier distributions achieve their bulk values, and charge neutrality obtains. This limiting behavior is expressed by

$$\lim_{x\to\infty} n(x) = n_b$$

$$\lim_{x\to\infty} p(x) = p_b$$

and

$$\lim_{x\to\infty} \rho(x) = 0$$

Combining the results, we find that the charge neutrality condition away from the junction requires that

$$p_b - n_b + N_D - N_A = 0 \tag{4.4}$$

Using this last result, we can express the net charge distribution in terms of the carrier excess over its bulk value by

$$\rho(x) = e\left\{\left[p(x) - p_b\right] - \left[n(x) - n_b\right]\right\} \tag{4.5}$$

This charge distribution is taken to be the source of the equilibrium electrostatic field within the semiconductor.

Whenever the Fermi energy level within the semiconductor differs by more than 3kT from either band edge, the electron and hole concentrations at any point must conform to the Boltzmann distribution (eqs. (4.1) and (4.2)). By multiplying the two distributions together, we obtain the equation

$$np = N_C N_V \exp\left(-\frac{E_G}{kT}\right) \tag{4.6}$$

Since the right-hand side of this expression is constant (for a fixed temperature), the product of $n(x)$ and $p(x)$ must also be constant. Equation (4.6) can be used

to introduce a convenient normalization for these concentrations. In the special case of the bulk region of an intrinsic semiconductor where there is no ionic charge, the condition of charge neutrality requires that electron and hole concentrations be equal, and the concentration in this case n_i is used as a norm. Since equation (4.6) holds in all cases (including this special one), n_i is given by

$$n_i^2 = N_C N_V \exp\left(-\frac{E_G}{kT}\right) \tag{4.7}$$

Using n_i as defined above, the concentration of electrons and holes in the general case can be normalized as

$$n = n_i \exp\left[\frac{E_F - E_I^*(x)}{kT}\right] \tag{4.8}$$

and

$$p = n_i \exp\left[-\frac{E_F - E_I^*(x)}{kT}\right] \tag{4.9}$$

where

$$E_I^* \equiv \frac{1}{2}(E_C + E_V) + \frac{kT}{2} \ln\left(\frac{N_V}{N_C}\right) \tag{4.10}$$

The relation between E_I^* and the bent energy bands is shown in figure 6. The electrostatic energy of an electron within the semiconductor relative to an electron in the intrinsic bulk is given by

$$e\phi(x) = E_F - E_I^*(x) \tag{4.11}$$

In terms of this electrostatic energy, the expressions for the carrier concentration become

$$n(x) = n_i \exp\left[\frac{e\ \phi(x)}{kT}\right] \tag{4.12}$$

and

$$p(x) = n_i \exp\left[-\frac{e\ \phi(x)}{kT}\right] \tag{4.13}$$

Now the limiting value of the electrostatic potential within the semiconductor defines the bulk value ϕ_b as

$$\lim_{x\to\infty} \phi(x) = \phi_b = E_F - E_I^*(\infty)$$

Comparing this value to the bulk values of the concentrations yields

$$n_b = n_i \exp\left(\frac{e\phi_b}{kT}\right) \tag{4.14}$$

and

$$p_b = n_i \exp\left(-\frac{e\phi_b}{kT}\right) \tag{4.15}$$

The electron and hole concentrations can also be expressed in terms of the bulk values by means of the equations

$$n(x) = n_b \exp\left[\frac{e(\phi - \phi_b)}{kT}\right] \tag{4.16}$$

and

$$p(x) = p_b \exp\left[-\frac{e(\phi - \phi_b)}{kT}\right] \tag{4.17}$$

By using the expressions for $n(x)$, $p(x)$, n_b, and p_b, normalized by the intrinsic concentration n_i, the concise expression is obtained for the charge distribution in terms of the electrostatic potential, namely

$$\rho(\phi) = 2en_i\left[\sinh\left(\frac{e\phi_b}{kT}\right) - \sinh\left(\frac{e\phi}{kT}\right)\right] \tag{4.18}$$

The condition for electrostatic equilibrium (Poisson equation) becomes in this case the second-order, nonlinear differential equation

$$\phi'' = -\frac{\rho(\phi)}{\varepsilon} = \frac{2en_i}{\varepsilon}\left[\sinh\left(\frac{e\phi}{kT}\right) - \sinh\left(\frac{e\phi_b}{kT}\right)\right] \tag{4.19}$$

sometimes referred to as the Poisson-Boltzmann equation. By means of the following changes in variables

$$u = \frac{e\phi}{kT}$$

and

$$u_b = \frac{e\phi_b}{kT}$$

this equation is written in the form

$$u'' = \frac{1}{L_D^2}(\sinh u - \sinh u_b) \tag{4.20}$$

where L_D is the Debye length given by the relation

$$\frac{1}{L_D^2} = \frac{2e^2n_i}{\varepsilon kT} \tag{4.21}$$

4.3 Solutions to Poisson-Boltzmann Equation

This section contains a description of the properties of solutions to the non-linear differential equation

$$u''(x) = \frac{1}{L_D^2}\{\sinh[u(x)] - \sinh(u_b)\} \tag{4.22}$$

defined for $0 \leq x \leq \infty$ and satisfying the limiting conditions

$$u(0) = u_0$$

and

$$\lim_{x\to\infty} [u(x) - u_b] = 0$$

To examine the asymptotic behavior of solutions to equation (4.22), the function δ, as defined by the equation $\delta = u(x) - u_b$, is introduced. The equation satisfies the differential equation

$$\delta'' = \frac{\cosh(u_b)}{L_D^2}\sinh(\delta) + \frac{\sinh(u_b)}{L_D^2}[\cosh(\delta) - 1]$$

For small values of δ, this equation assumes the linear form

$$\delta'' = \frac{\cosh(u_b)}{L_D^2}\delta$$

and has a bounded exponential solution with a characteristic asymptotic length given by

$$L_\infty^2 = \frac{L_D^2}{\cosh(u_b)} \tag{4.23}$$

Thus, bounded solutions to equation (4.22) display an asymptotic behavior of the form

$$u(x) \to u_b + A \exp\left(-\frac{x}{L_\infty}\right)$$

A first integral (energy integral) to the Poisson-Boltzmann equation can be obtained directly and leads to the first-order equation of the form

$$[\delta'(x)]^2 = \frac{2}{L_\infty^2}\{\cosh(\delta) - 1 + a[\sinh(\delta) - \delta]\} \tag{4.24}$$

where

$$a = \tanh(u_b) = \frac{n_b - P_b}{n_b + P_b} \tag{4.25}$$

The right-hand side of equation (4.24) is positive for $x > 0$, and it has a single zero at $x = 0$; the root of that equation thus yields the equation

$$\delta'(x) = \pm \frac{1}{L_\infty} H[\delta(x),a] \tag{4.26}$$

The function $H(\delta,a)$ is given by the expression

$$H(\delta,a) = \left(2\{\cosh(\delta) - 1 + a[\sinh(\delta) - \delta]\}\right)^{1/2} \tag{4.27}$$

The ambiguity in sign resulting from the square-root function can be resolved as follows. Since $H(\delta,a)$ is positive or zero for values of δ and a within their appropriate range of variation, the sign in equation (4.26) determines the slope of δ, and this slope maintains the same sign for all values of δ. Furthermore, the value of δ must approach zero within the bulk. Thus, in the case of the plus sign, δ approaches zero monotonically with increasing y from a negative surface value, as occurs in a p-type material depletion region. In the case of the minus sign, δ approaches zero monotonically with increasing y from a positive surface value, as occurs in an n-type material depletion region.

By making a scale change to the dimensionless independent variable $y = x/L_\infty$, so that $\delta(x)$ becomes $\delta(L_\infty y) = \Delta(y)$, one of the two remaining parameters in this equation can be eliminated, and the following equation can be obtained.

$$\Delta'(y) = \pm H[\Delta(y),a] \tag{4.28}$$

This equation depends upon the single parameter a. Integrating equation (4.28) yields

$$\int_{\Delta(0)}^{\Delta(y)} \frac{ds}{H(s,a)} = \pm y \tag{4.29}$$

This integral gives the value of Δ as an implicit function of the penetration parameter y in terms of the two parameters $\Delta(0)$, which specifies the potential drop across the semiconductor normalized to mean thermal energy

$$\Delta(0) = \frac{e}{kT}\left[\phi(0) - \phi(\infty)\right] \tag{4.30}$$

and a, which specifies the doping fraction and is defined in equation (4.25). The penetration parameter gives the actual penetration depth in units of the asymptotic length given in equations (4.21) and (4.23).

Results of a numerical evaluation of equation (4.29) are shown in figure 7. The dimensionless penetration parameter is plotted along the abscissa. No origin of this coordinate is defined in the graph, so that the zero value of y can be established beneath any specified initial value of $\Delta(0)$. The values of $\Delta(y)$ are plotted along the ordinate in a logarithmic scale increasing away from a central zero value in both directions. Naturally, the actual value of zero does not appear in the graph. Curves shown on the upper half of the figure are associated with the minus sign in equation (4.28) and represent a depletion region; curves in the lower half are associated with the plus sign and represent an accumulation region.

Under special circumstances, the solution to the Poisson-Boltzmann equation given by equation (4.29) takes on a simple form. For example, if the parameter a is equal to zero, the integral in equation (4.29) can be evaluated analytically to obtain the expression

$$\tanh\left[\frac{\Delta(y)}{4}\right] = \exp(\pm y)\ \tanh\left[\frac{\Delta(0)}{4}\right] \tag{4.31}$$

When Δ is either extremely small or extremely large, approximate values of the integrand can be developed which can be evaluated analytically. If, for example, $|x| \ll 1$, $H(x,a)$ can be approximated by

$$H(x,a) \approx x$$

and the resulting integral in equation (4.29) can be evaluated over intervals where $|\Delta| \ll 1$ to yield

$$\int_{\varepsilon_1}^{\varepsilon_2} \frac{ds}{H(s,a)} = \ln\left(\frac{\varepsilon_2}{\varepsilon_1}\right)$$

then for small initial values of $\Delta(0)$, $\Delta(y)$ changes exponentially to yield

$$\Delta(y) \approx \exp(\pm y)$$

Thus, all the curves in figure 7 approach a straight line with a slope of ± 1 as y decreases to zero. Similarly, if $|x| > 5$, the value of $H(x,a)$ becomes

$$H(x,a) \approx (1 + a)^{1/2} \exp\left(\frac{x}{2}\right)$$

Integrating this function over an interval where $|\Delta| > 5$ yields

$$\exp\left[-\frac{\Delta(0)}{2}\right] - \exp\left[-\frac{\Delta(y)}{2}\right] = \pm(1 + a)^{1/2} \frac{y}{2}$$

This explains the steep descent or ascent of the curves in figure 7 for large values of Δ. These curves are descending or ascending from an initial value $\Delta(0)$ with a half-length of

$$y_{1/2} \approx \exp\left[-\frac{|\Delta(0)|}{2}\right]$$

4.4 Abrupt Approximation

The solutions to the Poisson-Boltzmann equation indicate that the electrostatic potential in the space-charge region of the semiconductor decreases monotonically (or increases monotonically in the case of an accumulation layer) from its surface value to its value in the bulk over distances comparable to L_∞. For some analyses, it is convenient to approximate the electrostatic properties of the space-charge region still further by assuming that the electrostatic field changes linearly from its value at the surface to zero at a fixed depth W within the semiconductor and that the field remains zero throughout the bulk. In this abrupt approximation, the field strength is nonzero only within the region of width W, called the depletion width, at the surface. (See fig. 8.) Again, the depletion region of an n-type semiconductor is considered. The source of the space-charge field is the ionic charge distri-

bution ρ, exposed by the depleted majority carriers. From the assumed field distribution (fig. 8) and from the Poisson equation, it can be seen that

$$\frac{dE}{dx} = \frac{E_s}{W} = -\frac{\rho}{\varepsilon}$$

From this, the shape of the charge distribution is obtained as

$$\rho = -\frac{\varepsilon E_s}{W} \tag{4.32}$$

for $0 \leq x \leq W$ and $\rho = 0$ elsewhere. The potential drop across the depletion layer is then given by

$$\Delta V = -\frac{E_s}{2} W \tag{4.33}$$

Eliminating E_s from the two previous equations shows that the depletion width is determined by the potential drop across the depletion layer

$$W^2 = \frac{2\varepsilon\Delta V}{\rho} \tag{4.34}$$

If it is further assumed that all donor atoms are ionized (a reasonable assumption for temperatures near 300 K), then

$$\rho = eN_D = en_b$$

Finally, the following expression relates the depletion width W to the potential drop ΔV:

$$W = W_0(\Delta V)^{1/2} \tag{4.35}$$

where

$$W_0 = \left(\frac{2\varepsilon}{en_b}\right)^{1/2}$$

It follows that the mean electric field in the depletion region is given by

$$E = \frac{|E_s|}{2} = \frac{\Delta V}{W} = \frac{(\Delta V)^{1/2}}{W_0} \tag{4.36}$$

In this abrupt approximation, the mean space-charge field varies as the square root of the potential drop across the region, and it penetrates to a depth W_0 when the potential drop equals 1 V.

In some of the analyses which follow, it is expedient to use the abrupt approximation for the space-charge field of a depletion region instead of a field derived from the more general conditions of electrostatic equilibrium. It is of interest to compare the measure of field width in the abrupt approximation W_0 with the corresponding measure of the Poisson-Boltzmann field L_∞. As shown previously, L_∞ is given by

$$L_\infty^2 = \frac{\varepsilon kT}{2e^2 n_i}(\cosh u_b)^{-1}$$

where, from equation (4.14)

$$\cosh u_b = \frac{n_b + p_b}{2n_i}$$

In the depletion region of an n-type semiconductor $n_b \gg p_b$; therefore, L_∞ is relative to W_0 through the relation

$$\frac{L_\infty}{W_0} = \left(\frac{kT}{2e}\right)^{1/2} \tag{4.37}$$

At room temperature, this relation implies that $W_0 \approx 9L_\infty$.

5. CHARGE TRANSPORT IN A SEMICONDUCTOR ELECTRODE

5.1 Transport Equations

As shown in the preceding section, there are three interdependent variables involved in the macroscopic description of current flow in a semiconductor. Two of these are the concentrations of mobile charge carriers $n(x,t)$ and $p(x,t)$, representing the local concentration of electrons and holes, respectively. The third is the local electric-field intensity $\vec{E}(x,t)$. The electric field within the semiconductor is composed of two parts - the external field imposed from outside the system, and the internal field whose source is the internal charges (both fixed and mobile)

within the semiconductor-liquid interfacial region. These three quantities vary most in the interfacial region, and within the bulk of the semiconductor assume constant limiting values. The bulk electric-field intensity is taken to be zero, as its value is small compared with field values near the surface. The bulk values for the electron and hole concentrations are given by n_b and p_b, respectively.

The free charges move under the influence of local electric fields (drift) and local concentration gradients (diffusion), so that the current density for each carrier is given by

$$\vec{J}_n = e\left(n\vec{V}_n + D_n \vec{\nabla}n\right) \tag{5.1}$$

and

$$\vec{J}_p = e\left(p\vec{V}_p - D_p \vec{\nabla}p\right) \tag{5.2}$$

In these expressions, D_n and D_p are diffusion coefficients for the indicated carriers, and $\vec{V}_n$ and $\vec{V}_p$ are corresponding drift velocities. Throughout this discussion, it is assumed that the field intensity is small enough to allow the linear approximation given by

$$\vec{V}_n = \mu_n \vec{E} \tag{5.3}$$

and

$$\vec{V}_p = \mu_p \vec{E} \tag{5.4}$$

The carrier mobilities μ_n and μ_p are thus related to the diffusion coefficients through the Einstein relations

$$\frac{\mu_n}{D_n} = \beta = \frac{\mu_p}{D_p} \tag{5.5}$$

where

$$\beta = \frac{e}{kT}$$

The continuity relations for the carrier transport are

$$\frac{\partial n}{\partial t} - \frac{1}{e}\vec{\nabla} \cdot \vec{J}_n = G_n - R_n \tag{5.6}$$

and

$$\frac{\partial n}{\partial t} + \frac{1}{e} \vec{\nabla} \cdot \vec{J}_p = G_p - R_p \tag{5.7}$$

The terms on the right-hand side of each of these formulae represent the net local source of carriers; G_n and G_p represent the rate of carrier generation, and R_n and R_p represent the rate of recombination. These factors each depend upon the details of the structure of the semiconductor, such as the location and nature of imperfections or the distribution of donor and acceptor ions. Information about these structural features is scarce at present, mainly because the most successful semiconductor-electrode materials are metal-excess semiconductors derived from perovskite compounds which have not been well studied. To circumvent this lack of detailed information, a series of approximations to the carrier source term are described. The most significant of these approximations is the use of a mean carrier lifetime which is constant over a variety of different conditions.

First, consider that carriers are generated in pairs. That is, each carrier is produced by the excitation of an electron from the valence band to the conduction band. Consequently, a hole is created in the valence band, and the rate of electron generation equals that of hole generation. Furthermore, pairs are generated thermally at a rate given by g_0, and they may be photogenerated by light of intensity I_0 at a rate of g_{I_0}. Thus, we have a net carrier generation rate

$$G_n = g_0 + g_{I_0} = G_p \tag{5.8}$$

The thermal generation rate for electrons and holes in the bulk of the semiconductor, where there is no illumination, should equal the corresponding equilibrium recombination rates. These rates in turn depend upon the bulk concentrations and the thermal equilibrium value of the mean carrier lifetime. The thermal generation rate throughout the semiconductor and under all conditions of illumination are given by

$$n_b/\tau_n = g_0 = p_b/\tau_p \tag{5.9}$$

Also, assume that recombination of the charge carriers occurs in pairs within the semiconductor. No other mechanisms are considered which provide a sink of carriers such as trapping and surface recombination. The recombination rate is then given by

$$R_n = n/\tau_n = p/\tau_p = R_p \tag{5.10}$$

Also, in the sequel assume that the carrier lifetimes τ_n and τ_p are constant and represent the average values of lifetime for all recombination processes occurring in the semiconductor. Combining the results of equations (5.8) through (5.10) yields the net carrier sources as

$$G_n - R_n = g_{I_0} - (n - n_b)/\tau_n \tag{5.11}$$

and

$$G_p - R_p = g_{I_0} - (p - p_b)/\tau_p \tag{5.12}$$

Combining the expressions for the current densities with the continuity equations yields the carrier transport equation. This equation is most succinctly given in matrix form. To do this, the following terms are defined:

$$u = \begin{Bmatrix} n \\ p \end{Bmatrix} \qquad \mu = \begin{bmatrix} \mu_n & 0 \\ 0 & \mu_p \end{bmatrix}$$

$$D = \begin{bmatrix} D_n & 0 \\ 0 & D_p \end{bmatrix} \qquad F(u) = \begin{Bmatrix} F_n \\ F_p \end{Bmatrix} = \begin{Bmatrix} g_{I_0} - (n - n_b)/\tau_n \\ g_{I_0} - (p - p_b)/\tau_p \end{Bmatrix}$$

The transport equation is then expressed as follows:

$$\frac{\partial u}{\partial t} - D\nabla^2 u - \mu\vec{\nabla} \cdot (u\vec{E}) = F(u) \tag{5.13}$$

In this equation, the first two terms describe the diffusion of charge carriers, the next term accounts for their drift in the electric field, and the last term describes the reaction (generation and recombination) of the carriers.

5.2 Transport in Semiconductor Electrode

The general transport equation (5.13) is used to describe the behavior of the photoproduced excess charge carriers in a semiconductor electrode. As described in section 4, consider a semiconducting cylinder of cross-sectional area A oriented so that the liquid junction is perpendicular to the x-axis at $x = 0$. The concentrations of free carriers are defined for $x \geq 0$ and $t \geq 0$ and are given by the functions $n(x,t)$ and $p(x,t)$. Within the bulk of the semiconductor, these concentrations have the constant values n_b and p_b, respectively. The charge distribution in the semiconductor is due to the free carriers and to the distribution of ionic charge (assumed to be uniform throughout the semiconductor), so that

$$\rho(x,t) = e\left[p(x,t) - n(x,t) - (p_b - n_b)\right] \tag{5.14}$$

This charge distribution is the source of an internal electric field $E(x,t)$, as determined by the Poisson equation

$$\varepsilon \vec{\nabla} \cdot \vec{E} = \rho(x,t)$$

It is this field which is responsible for the drift in equation (5.13).

The inherent nonlinearity in this system arises from the fact that the field which causes the mobile carriers to separate depends upon the local distribution of carriers, as shown in equation (5.14). To gain some insight into the effect of this nonlinearity, we first examine the sourceless ($F \equiv 0$) and purely kinetic ($D \equiv 0$) case. In this way information is obtained about the possible stable asymptotic (in time) states. Equation (5.13) with $F = 0 = D$ becomes

$$\frac{\partial u}{\partial t} = \frac{u}{\varepsilon}\, u\, \rho(u) \tag{5.15}$$

As shown subsequently, the concentration for each of the charge species satisfies an equation displaying a quadratic nonlinearity which can be approximated by the form

$$z_t = a(z_0 - z)z \tag{5.16}$$

The phase portrait for this ordinary differential equation (shown in fig. 9) displays two asymptotic states: $z = z_0$ and $z = 0$. The asymptotic state $z = z_0$ is the only stable one, so any (nonzero) concentration tends to this state. We conjecture that this situation pertains to all cases where $t > 0$, even when sources and diffusion are present. As a consequence there is a stable asymptotic (steady-state) solution to equation (5.15). One way to test this conjecture would be to study the transient response of this system for different illuminations. What we shall do instead is examine the limiting case of very intense illumination and estimate values of the incident intensity which lead to saturation of the photoeffects.

Under steady-state conditions, the transport equation (5.13) becomes

$$\nabla^2 u + D^{-1}\mu\, \vec{\nabla} \cdot (\mu \vec{E}) + D^{-1}F = 0 \tag{5.17}$$

Although unnoticed by many researchers, the system of equations (5.17) and (5.14) posseses a first integral. This fact can be used to eliminate the nonlocality of the system. The local charge excess distributions are as follows:

$$Q^{+}(x) = e\int_0^x dx\left[p(x) - p_b\right] \tag{5.18}$$

and

$$Q^{-}(x) = -e\int_{0}^{x} dx\left[n(x) - n_b\right] \tag{5.19}$$

The local field can be expressed as

$$E(x) = E(0) + \frac{1}{\varepsilon}\left[Q^{+}(x) + Q^{-}(x)\right] \tag{5.20}$$

while the steady-state equation (5.17) becomes

$$u'' - \beta E(x) B \cdot u' + Au = I(x) \tag{5.21}$$

with

$$u = \left[Q^{+}(x),\ Q^{-}(x)\right]$$

and

$$B = \begin{bmatrix} 1 & 0 \\ 0 & -1 \end{bmatrix}$$

$$A = \begin{bmatrix} \omega_p^{\,2} & \alpha_p L_p^{\,2} \\ \alpha_n L_n^{\,2} & \omega_n^{\,2} \end{bmatrix}$$

$$I(x) = \begin{Bmatrix} I_p(x) \\ I_n(x) \end{Bmatrix}$$

where

$$I_p(x) = \frac{1}{L_p^2}\left[\alpha_p \varepsilon\, E(0) - Q^+(\infty)\right] + \frac{e}{D_p} I_0 \exp(-\alpha x)$$

$$I_n(x) = \frac{1}{L_n^2}\left[\alpha_n \varepsilon\, E(0) - Q^-(\infty)\right] - \frac{e}{D_n} I_0 \exp(-\alpha x)$$

$$\omega_p^2 = \frac{1}{L_p^2}(1 + \alpha_p) \qquad \alpha_p = \beta \frac{e}{\varepsilon} p_b L_p^2$$

$$\omega_n^2 = \frac{1}{L_n^2}(1 + \alpha_n) \qquad \alpha_n = \beta \frac{e}{\varepsilon} n_b L_n^2$$

Equation (5.17) describes a system with a quadratic nonlinearity and suggests an iterative scheme for solving the system. Let u_0 be the solution to

$$u_0'' - Au_0 = I(x)$$

and from this solution form the drift field

$$E(x) = E(0) + \ell(u_0)$$

where $\ell(\ )$ is a linear functional. Next, solve equation (5.17) with this drift field. In other words, u_0 is the first solution in a sequence generated by the progression

$$u_n = u_{n-1} + \delta u_{n-1} \qquad (n = 1, 2, 3, \ldots)$$

where each solution satisfies the linear differential equation

$$u_n'' - Au_n = I(x) + \beta\left[E(0) + \ell(u_{n-1})\, u_{n-1}'\right] \tag{5.22}$$

By analogy with the sourceless kinetic case described by equation (5.15), equation (5.22) is expected to possess one stable solution which will be reached after a sufficient number of iterations.

5.3 The Effect of High-Intensity Light

Examine the first-order solution to the system of equation (5.17) subject to boundary conditions at $x = 0$ of the following form:

$$n(0) = n_b \exp(\beta\Delta V)$$

and

$$p(0) = p_b \exp(-\beta\Delta V)$$

where ΔV is the potential drop across the semiconductor. This solution leads to a relationship between the potential ΔV and the incident light intensity of the form

$$\frac{\Delta V}{V_0} - \exp(-\beta V) + \left(1 - \frac{I_0}{I_{0,s}}\right) = 0 \tag{5.23}$$

where

$$V_0 = \frac{e}{\varepsilon} n_b L_n^2$$

and

$$I_{0,s} = \alpha n_b D_n$$

Equation (5.23) can be rewritten in terms of $X = \beta\Delta V$ as

$$\frac{I_0}{I_{0,s}} = \lambda(X, X_0) = \frac{X}{X_0} + 1 - \exp(X)$$

and it gives the ratio of I_0 to $I_{0,s}$ in terms of a single parameter $X_0 = \beta V_0$. Figure 10 depicts this relationship. There are two zeros for $\lambda(X,X_0)$: one at $X = 0$ and the other at $X = -X_0$. Only one of these can correspond to a stable asymptotic state, and the well-known behavior of V for low to moderately high

intensity suggests $X = -X_0$. Thus, V_0 is identified with the dark bent-band potential as

$$V_0 = V_{bb} = V_F - V_{REDOX}$$

Inverting $\lambda(X,X_0)$ and taking the stable branch indicated by the solid line in figure 9, the bent-band potential is found as a function of light intensity. This curve maximizes for

$$\left(\frac{I_0}{I_{0,s}}\right)_{max} = 1 - \frac{\ln X_0 + 1}{X_0}$$

as shown in figure 11. For $\lambda \approx 1$ near the saturation point, equation (5.23) can be approximated by

$$\Delta V \approx V_0\left(1 - \frac{I_0}{I_{0,s}}\right) \tag{5.24}$$

Thus, an estimate for the intensity of the incident photon flux at which saturation occurs is obtained as follows:

$$I_{0,s} = \alpha n_b D_n \tag{5.25}$$

To make a general estimate of saturation levels, take $\alpha = 10^6\ m^{-1}$, $n = 10^{24}\ m^{-3}$, and $D = 10^{-3}\ m^2/s$ to obtain

$$I_{0,s} \approx 10^{27}\ \text{photons/m}^2\text{-s}$$

This corresponds to an energy flux of $10^4\ W/cm^2$ for monochromatic light at wavelength 0.55μ. This is a conservative estimate, since the quantum efficiency of the process, other charge sinks, and the nonlinearity in the recombination process that would require increased flux have been neglected.

6. SATURATION OF PHOTOELECTROLYSIS OF WATER USING A PHOTOELECTROCHEMICAL CELL

In recent investigations of photoelectrochemical cells with semiconductor electrodes, there appears to be no evidence of saturation of the energy conversion process (refs. 15 through 18). The photocurrent at a fixed cell voltage increases linearly with light intensity up to 380 W/cm^2 (ref. 13). The energy flux level at which saturation occurs is an important parameter which is needed in order to understand the processes governing the operation of the cell. In addition, the saturation

flux level is a critical parameter for the design of effective energy conversion devices. In the theoretical study of nonlinear effects of charge transport processes within the semiconductor electrode, it was found that the light intensity which causes saturation varies directly with the charge carrier concentration (eq. (5.25)). An experimental search for saturation effects using $SrTiO_3$ crystals was undertaken. These crystals were slightly reduced to form a metal excess semiconductor of high resistivity (low carrier concentration). The $SrTiO_3$ electrodes were illuminated with the 351-nm and 364-nm radiation from an argon-ion laser with a maximum intensity of 60 mW/cm^2. A nonlinear variation of the photocurrent with light intensity and the evidence for complete saturation of the photoprocesses in $SrTiO_3$ at a light intensity near predicted values were observed. This experiment is discussed in the following paragraphs.

Single-crystal wafers of $SrTiO_3$ were cut from a boule and polished. The grit size of the final polish was 0.05 μm. The crystals were reduced in a hydrogen atmosphere at about 700°C for less than 1 minute. The conductivity was estimated by measuring the current as a function of applied voltage for a fixed electrode separation using a curve tracer. An attempt to determine the resistivity of the samples by the four-point probe technique (ref. 19) proved unsuccessful because of high sample resistivity. Ohmic contacts were made using an indium alloy rubbed on one side of the crystals and a copper wire attached to this contact with a silver paste. The sample was mounted on a glass tube with a silicone-based adhesive. The electrolytic cell was a stainless-steel vessel with a quartz window and consisted of the $SrTiO_3$ photoanode, a platinum counter electrode, a saturated calomel reference electrode (SCE), and a buffered solution of NaOH adjusted to pH-13. During the experiment, hydrogen gas was bubbled across the platinum electrode and, using a potentiostat, the photoanode was maintained at zero volts with respect to the SCE. The level of uv radiation from the argon-ion laser was controlled using neutral density filters calibrated for uv radiation. The laser output was continuously monitored by reflecting part of the laser beam into a power meter.

Thirty-two crystal samples were prepared as described above and used to form the photoanode of an electrolytic cell. Characteristic current-voltage data were taken at fixed light intensity values to insure that each cell was operating properly. Then, while the cell remained at a fixed bias of zero volts relative to the SCE, the intensity of the incident radiation was varied, and the photocurrent was measured for each light intensity. The results of these measurements separated the crystal samples into three categories, distinguished generally by crystal resistivity. Three of the samples had a very high resistivity (on the order of 10^6 ohm-cm), and each of these exhibited a saturation in photocurrent with light intensity. A typical saturation curve for a crystal in this category is shown in figure 12. Several samples had resistivities varying from 10^4 to 10^3 ohm-cm. For these samples the photocurrent versus intensity displayed some curvature, suggesting saturation but not achieving it at the intensities available in this experiment. The remaining category of crystals had resistivities of 10^3 ohm-cm, and for these samples the photocurrent varied linearly with light intensity within the intensity range of this experiment.

The model of excess charge transport processes within the semiconductor developed in the preceding section predicts a saturation for the photon flux given by the expression

$$I_{0,s} = \alpha n_b D_n \tag{6.1}$$

where n_b is the bulk free carrier concentration, D_n is the diffusion constant, and α is the photoabsorption coefficient. Since the semiconductor resistivity ρ is related to the concentration n_b and mobility $\mu_n = \beta D_n$ (where $\beta = e/kT$) of the carrier by $\rho = (en_b\mu_n)^{-1}$, equation (6.1) can be written as

$$I_{0,s} = \frac{\alpha}{e\rho\beta} \tag{6.2}$$

Values for the absorption coefficient of $SrTiO_3$ for radiation in the uv region are not readily available, but an average value of 4.4×10^4 cm^{-1} is quoted by Capizzi and Frova (ref. 20). For a crystal with a resistivity of 10^6 ohm-cm and an incident photon energy equal to that of the argon laser used in this experiment, equation (6.2) gives a saturation flux of 2 mW/cm^2. This value agrees with the order-of-magnitude estimate for the experimental results presented here. A fully reduced crystal of $SrTiO_3$ has a resistivity about 10^6 times lower than the samples used here, so photosaturation at an energy flux of 2 kW/cm^2 would be expected. This high value of radiant energy flux is consistent with the failure to observe saturation in previous experiments.

7. THERMAL PHOTOELECTROCHEMICAL CELL

The solar conversion efficiency of a stable semiconductor-based photoelectrolysis cell is on the order of 1 percent. This is a result of the fact that only the metal-oxide semiconductors are stable to the electrolysis process, and they are photoactive for photon energies around 3 eV or for uv radiation. Decreasing the bandgap of the stable electrodes should increase the efficiency, since more of the solar flux would be utilized. The bandgaps of most semiconductors decrease with increasing temperature, so an experimental thermal photoelectrochemical cell was assembled to assess the effect of temperature on conversion efficiency to broadband radiation. Two temperature effects were anticipated - thermal bandgap narrowing of the photoelectrode and decrease of the potential required for the electrolysis of water (reversible electrolysis potential). Both of these effects should result in an increase in the solar conversion efficiency. Figure 13 shows the effect temperature has on thermoneutral potential and the reversible electrolysis potential for water. It can be seen that the reversible electrolysis potential decreases from 1.23 V at standard conditions as the cell temperature increases. This decrease is due to the increased contribution to the electrolysis reaction made by the thermal energy available in the aqueous solution.

A schematic of the experimental setup is shown in figure 14. The thermal photoelectrochemical cell was a stainless-steel vessel capable of providing temperatures to 200°C. A quartz window mounted on the side of the stainless-steel vessel allowed the photoelectrode to be illuminated by a 150-W xenon lamp. A platinum screen was used as a counter electrode, and mercury-mercuric oxide was used as the reference electrode. Argon was used to pressurize the vessel to prevent the water from boiling at high temperatures. The 0.1-M NaOH electrolyte and the electrodes were contained in a quartz beaker within the stainless-steel pressure vessel. The solution was stirred using a Teflon-coated magnetic stirring bar, and the photocurrent-voltage characteristics of the cell were monitored with a potentiostat and x-y recorder. The photoelectrodes tested were TiO_2 and $SrTiO_3$ single crystals reduced in a hydrogen atmosphere for 2 hours at 800°C. The temperature-induced changes in the photoresponse characteristics of an $SrTiO_3$ based cell are shown in figure 15. Two thermal effects are evident. First, the magnitude of the onset potential (the most negative

potential which produces current) decreases as the cell temperature increases. This decrease is deleterious to the conversion efficiency, because it is necessary for the onset potential to be negative with respect to the redox potential of hydrogen. Second, the photocurrent increases with increasing temperature for cell voltages above about -0.2 V referenced to Hg/HgO. This effect favors the increase in the conversion efficiency. The conversion efficiency η can be obtained from the relation

$$\eta = \frac{I_{ph}(1.23 - V_{app})}{\text{Photon flux}} \tag{7.1}$$

where I_{ph} is the photocurrent, V_{app} is the externally applied voltage, and 1.23 is the reversible electrolysis potential for water. A relative efficiency can be determined by using the efficiency at room temperature as a reference. A plot of the relative efficiency as a function of cell temperature for an $SrTiO_3$ based photoelectrochemical cell is shown in figure 16. The relative efficiency peaks at about 100°C and shows a 50-percent increase in efficiency. The decrease in conversion efficiency above 100°C is caused by the thermally induced decrease in the onset potential for this electrode. The relative efficiency for the $SrTiO_3$ samples peaked at temperatures ranging from 75°C to 100°C. The thermal response of TiO_2 based cells was similar to the $SrTiO_3$ based cells, that is, onset potential decreased with increasing temperature, photocurrent increased with temperature, and the relative efficiency peaked at temperatures ranging from 75°C to 100°C. The rate at which the onset potential decreased with increasing temperature for the TiO_2 samples was smaller than for the $SrTiO_3$ crystals. This effect was investigated and found to be related to the point of zero zeta potential (pzzp) of the material. A discussion of the pzzp results is included in the next section.

The relative photocurrents for both TiO_2 and $SrTiO_3$ at 1.5 V referenced to Hg/HgO as a function of temperature are shown in figure 17. The thermal increases in the relative photocurrent for both the $SrTiO_3$ and TiO_2 correspond to approximately 0.25 percent/K. The thermal enhancement of the photocurrent observed here is attributed to changes in the photoelectronic properties of the semiconductor anodes. The absorption coefficient of the metal oxides is known to be temperature dependent (refs. 20 through 22) and is considered to be the principal cause of the photothermal enhancement observed.

The spectral dependence of the absorption coefficient α for the two semiconductor materials used can be divided into two energy regions. One energy region is below the bandgap and is governed by the Urbach rule (refs. 20, 21, and 23), and the second region of energies is greater than the bandgap energy.

Figure 18 illustrates the two absorption regions as well as the spectral irradiance of the xenon lamp, which is nearly constant in the region between the bandgap of $SrTiO_3$ (400 nm) and 420 nm. The Urbach effects for the two cell-temperature extremes (300 K and 450 K) are shown here and are calculated from

$$\alpha = \alpha_0 \exp\left[-\frac{E_G}{kT}\left(1 - \frac{hc}{\lambda E_G}\right)\right] \tag{7.2}$$

where $\alpha_0 = 4.4 \times 10^4\ \mu m^{-1}$ (ref. 18), T is the absolute temperature, E_G is the bandgap, k is the Boltzmann constant, h is the Planck constant, c is the speed of light, and λ is the wavelength. The temperature dependence of the current density J_u produced by absorption in the Urbach region is $eFI_0\left(\frac{kT}{h}\right)$ where I_0 is the light intensity at the bandgap and F is a constant of order unity. Even though there is a significant change in the absorption coefficient in the Urbach region due to temperature changes, this effect contributes only approximately 1 percent of the total thermal-induced enhancements observed.

Assuming the absorption coefficient is independent of changes in bandgap, the change in the relative photocurrent with temperature is approximately 1 percent/K. To arrive at this figure, the spectral output of the light source and the rate of change of the bandgap with temperature for $SrTiO_3$ (-0.95×10^{-4} eV/K) were used (ref. 24). The results for TiO_2 are expected to be similar. This result is a factor of 4 higher than observed experimentally, but no consideration has been given to the effect of temperature on loss mechanisms such as recombination.

In conclusion, experiments indicate that photocurrent efficiency of broadband radiation for $SrTiO_3$ and TiO_2 based photoelectrochemical cells can be enhanced and that this increase can be attributed to the thermal decrease in bandgap. This technique may also be beneficial in enhancing the solar conversion efficiency for the stabilized liquid junction solar cells.

8. ONSET POTENTIAL AND POINT OF ZERO ZETA POTENTIAL

In the previous section it was noted in the discussion of figure 15 that the onset potential for both TiO_2 and $SrTiO_3$ samples decreased as the cell temperature increased, and that the rate observed for TiO_2 was smaller than that for $SrTiO_3$. The thermal change in the onset potential for single crystals of α-Fe_2O_3 and a polycrystalline WO_3 sample were also investigated.

The onset potential was taken from the photocurrent voltage recordings using a conventional three-electrode system. The experimental apparatus is shown schematically in figure 19. The light from a 150-W xenon lamp was chopped and the photocurrent recorded using a lock-in amplifier. The cell was held inside a stirred and heated water bath. A reversible hydrogen electrode (RHE) was used as a reference electrode for most of the experiments. In some experiments conducted in basic solutions, an Hg/HgO electrode was used as a reference electrode for comparison. Solutions of NaOH (pH-13) and H_2SO_4 (pH-2) were used.

The effect of temperature on the onset potential for these materials at two different solution pH values is shown in figure 20. A linear change of the onset potential with respect to the RHE is observed in all the cases. The slope of the change is different for each electrode material; the highest slopes were observed for Fe_2O_3 and $SrTiO_3$, and the lowest for WO_3. These measurements were repeated with solutions of different pH. From figure 20 it can be seen that the slope of the onset potential versus temperature is about the same for each electrode with solutions of either pH-13 or pH-2.

The relationship between the onset potential (taken to be the flatband potential V_{FB} for the electrode), the redox level for hydrogen V_0, the potential drop across the Helmholtz layer V_H, the electron affinity EA, and the position of the

Fermi level with respect to the conduction band edge Δ_{FC} is shown in figure 21 and is given (refs. 25 through 28) as

$$EA = eV_0 + eV_H + eV_{FB} + \Delta_{FC} \tag{8.1}$$

Changes in temperature can effect Δ_{FC}, V_H, and V_0. It can be shown (ref. 29) that the change in the onset potential with temperature using an RHE as the reference electrode is

$$\frac{\Delta V_{FB}}{\Delta T} = \frac{2.3R}{F} pH_{pzzp} - \frac{R}{F} \ln\left(\frac{n}{N_C}\right) \tag{8.2}$$

where R is the gas constant, F is the Faraday constant, n is the free carrier density in the semiconductor, N_C is the density of states in the conduction band, and

$$pH_{pzzp} = \left[\left(\frac{2.3RT}{F}\right) \log[H^+]_{pzzp}\right]$$

which is the pH at the point of zero zeta potential for the electrode. Equation (8.2) shows that the onset potential of an oxide semiconductor electrode shifts linearly with increasing temperature to a more positive potential with a slope which is independent of the pH of the solution and which is determined by the magnitude of the pH_{pzzp}. The more basic the electrode surface, the higher the pH_{pzzp}, and the result is a larger change in the onset potential with cell temperature. The pH_{pzzp} for each electrode was determined using equation (8.2) and the slopes of the curves in figure 20 for pH-2 and pH-13 solutions. These values are given in table I. Also given in table I are the carrier concentrations and density of states for each of the semiconductor materials used to determine the magnitude of the second term on the right-hand side of equation (8.2). The average value for the pH_{pzzp} of each electrode is shown in figure 22. It should be noted that the tungsten trioxide sample is degenerately doped, and therefore the second term on the right-hand side of equation (8.2) is zero. Also shown in table I and figure 22 are pH_{pzzp} values for these semiconductor materials taken from the literature. The curve drawn in figure 22 is taken from reference 26. There is good agreement between the values obtained in this work and the values taken from the literature. Since equation (8.2) properly describes the observed behavior of the onset potential of the oxide semiconductors reported here, the changes in the onset potential with temperature are attributed to thermal effects on the potential across the Helmholtz layer.

These results lead to two important considerations for choosing semiconducting materials to be used as photoelectrodes in a photoelectrochemical cell. First, the onset potential of the photoelectrode is dependent on the EA of the electrode material and on the potential across the Helmholtz layer. The onset potential is more negative the smaller the EA and the more acidic the electrode surface (smaller pH_{pzzp}). While the EA of the electrode material cannot in principle be changed, the pH_{pzzp} can be changed (ref. 30). It was suggested (ref. 30) that by binding more acidic groups to the surface of TiO_2, for example, the onset potential could be shifted to more negative values. The method described here can be used to evaluate

in a relatively easy way any change in the acidity of the electrode surface following treatment. (The common methods of evaluating the pH_{pzzp} of the materials in the powder form are not applicable here.)

Second, as discussed in the preceding section, there is the possibility of increasing the solar-to-chemical energy conversion efficiency of a photoelectrochemical cell by increasing the cell temperature (refs. 28 and 29). For $SrTiO_3$ and TiO_2, the photocurrent increases by increasing the cell temperature, and the overall efficiency begins to increase. At cell temperatures higher than about 80°C, the efficiency begins to decrease because the onset potential for these materials has shifted to more positive values.

These experiments suggest that by decreasing the value of the pH_{pzzp} (e.g., by binding acidic groups to the surface), the amount of the thermally induced shift in the onset potential of the photoelectrodes may be reduced. This reduction would improve the efficiency of the photoelectrochemical cell by increasing the temperature.

9. PHOTOPRODUCTON OF HALOGENS

To obtain the maximum conversion efficiency for a given semiconductor, and therefore for a fixed bandgap, it is necessary to find a redox couple whose electrolysis potential is slightly less than the bandgap energy and whose redox reactions lie within the bandgap. For example, the maximum efficiency attainable (as shown in section 7) for the electrolysis of water (electrolytic potential of 1.23 V and enthalpy of 1.47 V) by TiO_2 with a bandgap of 3 eV is

$$\eta_{max} = \frac{1.47\ eV}{3.0\ eV} = 0.49 \tag{9.1}$$

The conversion efficiency can be increased, for example, by finding an electrolytic reaction which is driven at about 3 V. In this situation the conversion efficiency would be 1. These efficiencies presume that the incoming radiation is monochromatic and has an energy of 3 eV, which is the bandgap of TiO_2.

An example of one such reaction is the electrolysis of HF. In acid solutions the electrolytic potential is 3 V, and the reactions at the electrodes produce hydrogen and fluorine as

$$2HF \rightarrow H_2 + F_2 \tag{9.2}$$

Experiments were attempted using $SrTiO_3$ and TiO_2 single crystals in aqueous solutions of 0.1 M HF. However, as expected from the corrosive nature of HF, the HF chemically attacked the semiconductor electrodes. Attention was turned to the other halogens: chlorine, bromine, and iodine. The redox levels for these halogens and water in relation to the bandgap of TiO_2 at two acid pH values are shown in figure 23. The photoelectrolysis of these compounds has been analyzed (refs. 31 and 32) for the case of single-crystal TiO_2 photoelectrodes in the standard photoelectrochemical cell. The results of these analyses indicated that chloride, bromide, and iodide ions were oxidized at an illuminated TiO_2 electrode.

Some work has been done using n-type semiconductor powders (refs. 33 through 37) to photocatalyze oxidaton reactions which otherwise would occur at very low rates. The platinized semiconductor powder can be considered to provide many short-circuited, platinum, semiconductor electrodes on which photoassisted reactions can take place, provided the reduction process occurs at a more positive potential than the flatband potential of the semiconductor. To date, most of the reactions at illuminated TiO_2 or Pt-TiO_2 powders are, by their nature, photocatalytic (refs. 33 through 39). The possibility of carrying out photosynthetic reactions is of greater interest (refs. 39 and 40). The experimental results summarized herein deal with the producton of the halogens at TiO_2 powders suspended in aqueous solutions of their respective ions. The reactions investigated were the photoassisted oxidation of the halogens and the reduction of oxygen at TiO_2 particles. The process is shown schematically in figure 24 for chlorine. The two half-reactions assumed are:

$$2X^- + 2h^+ \rightarrow X_2 \tag{9.3}$$

at the illuminated TiO_2 site, and

$$\frac{1}{2} O_2 + 2H^+ + 2e^- \rightarrow H_2O \tag{9.4}$$

at the platinized site. These half-reactions give the overall reaction

$$2X^- + \frac{1}{2} O_2 + 2H^+ \rightarrow X_2 + H_2O \tag{9.5}$$

where H^+ and e^- are the photoproduced hole-electron pair and X is the appropriate halogen. The experimental details can be found in reference 41.

The energetics of the processes described by reactions (9.3) through (9.5) for the three halogens are shown in figure 23. The figure shows that the oxidation of I^- to I_2 by oxygen is a spontaneous reaction. Adding the Pt-TiO_2 photocatalyst, however, was found to enhance the oxidation rate, as shown in table II. More striking is the photo-oxidation of Br^- and Cl^- at the Pt-TiO_2 powder surface. The oxidation of these halides by oxygen is nonspontaneous at pH - 5.5 with ΔG = 8 kcal/mole for Br^- oxidation and ΔG = 21 kcal/mole for Cl^- oxidation. However, these halides were produced in the presence of the platinized titanium dioxide particles and light, and the results are given in table II. These are clear examples of a chemical reaction taking place at the illuminated platinum-semiconductor powder surface in a nonspontaneous (photosynthetic) direction and giving rise to useful chemicals.

The fact that photosynthesis is clearly achieved in this system indicates that charge separation occurs in the semiconductor powder (without external biasing) by introducing the platinum. With pure powder, much smaller rates were found, indicating charge separation was not effective. (See table II.) The effect of platinization is associated with the fact that the overvoltage for oxygen reduction at the particle is lowered (refs. 38 and 42).

It was found that the rate of production of the halogens is in the order $I_2 > Br_2 > Cl_2$. This is because of the difference in the ability of the halide

anions to compete with water for the photoproduced holes in the semiconductor (refs. 31 and 32), and also because of the difference in the ability of oxygen to compete with the halogen for reduction on the platinum site.

The rate of the halogen production was enhanced by lowering the solution pH. (See table II.) This can be understood from reactions (9.3) through (9.5) and figure 23: (a) the oxidation potential of water is more positive at lower pH; therefore, halide oxidation becomes more competitive; and (b) the reduction potential of oxygen is more positive at lower pH; therefore, oxygen becomes more competitive with the halogen molecules for reduction at the platinum sites. In fact, at the lower pH, the oxidation of Br^- becomes photocatalytic as can be seen from figure 23.

For the case of the photosynthetic reactions demonstrated, net conversion of solar energy to chemical energy is also achieved. The efficiency for this conversion can be calculated using the equations

$$\eta = \frac{\text{Energy stored as } X_2 - \text{Energy from power supply}}{\text{Light energy}} \tag{9.6}$$

$$\eta = \frac{I(V_{prod} - V_{ext})t}{\text{Light energy}} \tag{9.7}$$

where t is the illumination time, I is the rate of X_2 production expressed in units of current, V_{prod} is the difference in the redox potentials of the two half-reactions of the cell, and V_{ext} is the voltage supplied from an external source. The photosynthetic reaction is carried out without supplying electrical power from an external source; thus, $V_{ext} = 0$. Taking into consideration only the light absorbed by the TiO_2, the calculated optical power efficiency for the ideal case of Cl_2 production is 3 percent. This is compared with the 1- to 2-percent solar-to-electrical energy conversion efficiency at TiO_2 electrodes (refs. 43 and 44). In the acidic solution where Cl_2 is allowed to accumulate, a power efficiency of 0.03 percent is calculated for the conversion of solar-to-chemical energy. The practical values for the efficiency would be between these values. If the whole spectrum of available light energy is taken into consideration, the efficiencies calculated are lower.

The halogens produced in this way can be used not only as a source of chemical energy in space and on Earth, but also by the chemical industry, which uses these chemicals in large quantities. At the present time, these chemicals are being produced primarily from electrolytic cells using electrical energy to drive the desired reaction. This technique only requires a source of uv radiation which can be supplied by the Sun.

Figure 25 is a schematic of a photoelectrochemical cell as well as a magnified view of the chemical processes taking place on the powder. Solar ultraviolet light absorbed by the platinized TiO_2 powder oxidizes the halide ion to the halogen molecule (e.g., chloride ion from a brine solution to chlorine gas) and reduces oxygen which is supplied by bubbling air through the reaction vessel. The chemical reaction taking place in the presence of the powder and uv light is shown in reaction (9.5). The halogen gas is collected above the brine solution and may be separated from the air by membranes. The TiO_2 powder is inexpensive because it is widely used in paint, and a natural source of brine on Earth could be seawater. The technique of getting

chlorine from seawater is an energy-efficient process capable of producing a product widely used in the chemical industry.

10. LAYERED TRANSITION METAL THIOPHOSPHATES

The search for stable, small-bandgap semiconductor materials for use as electrodes in photoelectrochemical cells has led to the metal chalcogenides, MX_2, such as MoS_2, and WSe_2 (refs. 45 through 51). These materials have a layered crystal structure. In such structures, the chalcogenide bonds within the layer are saturated, and the individual layers are bound to each other by weak van der Waals forces. Electron-hole generation appears to occur because of d-d phototransitions. These transitions do not affect the chemical bonds in the crystal, so the crystal resists photodecomposition.

A new class of layered compounds was recently analyzed for use as photoelectrodes in photoelectrochemical cells (ref. 52). These materials are of the type MPX_3 where M is a transition metal, P is phosphorous, and X is an element of the sulfur series. These materials have been called transition metal thiohypophosphates (refs. 53 and 54).

Single crystals of the transition metal thiophosphate crystals were grown by iodine vapor transport in quartz ampules 10 cm in length and 1.5 cm in diameter (refs. 53 and 54). A 4-g charge consisting of a stoichiometric mixture of the elements, to which 150 mg of iodine was added, was introduced into one end of the ampule, and the ampule was sealed in a nitrogen atmosphere. A tube oven with a horizontal temperature gradient given in table III was used for the growth process. Growth conditions were maintained for about 100 hours, resulting in crystals up to about 10 mm × 10 mm × 0.1 mm.

The photoelectrochemical response of $SnPS_3$, $NiPS_3$, and $FePS_3$ used as electrodes in an aqueous solution containing sulfuric acid at pH-2 is shown in figure 26. The curves labeled (a) are the dark currents, and the curves labeled (b) indicate the photocurrent when the sample was irradiated with the full intensity of the 150-W xenon lamp. The three materials shown have a very low dark current and a clear photoresponse. The $SnPS_3$ sample has a photoanoidic response typical of n-type semiconductor compounds. Single-crystal samples of $SnPS_3$ grown under apparently similar conditions showed photocathodic response as well as a response expected of an intrinsic semiconductor electrode. This suggests that the growth conditions are important in determining the doping characteristics of the $SnPS_3$. Also, two types of $SnPS_3$ crystals were consistently produced. One type was distinctly layered with only a few layers per sample, and the other type was more granular and layered. No effort was made to correlate the growth conditions with the resulting doping characteristics of the $SnPS_3$ crystals. The $FePS_3$ and $NiPS_3$ crystals behave as p-type semiconductor electrodes. Crystals of $FePS_3$ and $NiPS_3$ from different growths all behaved as p-type materials.

Crystals of $SnPSe_3$ and $MnPS_3$ showed n-type response. These two materials were very unstable in both acid and base solutions. The photoresponse of $BiPS_4$ crystals was typical of an intrinsic photoelectrode. This material was also unstable in acid or base electrolytes, and as a result, no bandgap data were obtained. In addition to the above materials, $CoPS_2$, $CrPS_3$, $FePSe_3$, and $GaPS_2$ crystals were grown and gave no photoresponse and were very unstable in acid solutions.

The onset potential in volts for the photocurrent of the $SnPS_3$ samples was 0 referenced to SCE at pH-2. This onset potential is about 850 mV more negative than the reversible potential for oxygen evolution, which indicates a net gain in energy conversion. The onset potential for $FePS_3$ is about 400 mV more cathodic than the reversible potential for hydrogen evolution. This indicates a net gain in energy conversion. The position of the band edges of $SnPS_3$ and iodine redox potentials are shown in figure 27.

Investigations of the stability of these compounds under illumination were made in both acid and base electrolyte. The crystals were very unstable in a high pH environment, and after a short period of time, the photocurrent decayed to zero. Inspection of the crystals indicated that delamination of the layers occurred as well as photocorrosion. All the selenide compounds photocorroded in acid solutions also. The sulfur-based compounds were found to be stable for periods up to an hour in strongly acid solutions. The surface of these materials exposed to the electrolyte showed no signs of degradation when inspected under a light microscope. However, even the sulfur-based crystals were very unstable in acid solutions if the edges of the layers were exposed to the electrolyte.

The photocurrent response as a function of photon energy was determined for some of the layered materials. The photocurrent response for n-type $SnPS_3$ is shown in figure 28. Assuming that a Schottky barrier exists at the electrode-electrolyte interface, then, near the band edge, the photocurrent I_{ph} will have the following dependence on the photon energy E_{ph}:

$$I_{ph} = \left(\frac{A}{E_{ph}}\right)\left(E_{ph} - E_G\right)^{n/2} \tag{10.1}$$

where A is a constant for a fixed applied potential, E_G is the bandgap energy, and n depends on the bandgap optical transitions. That is, $n = 1$ for a direct transition and $n = 4$ for an indirect transition. (See refs. 55 and 56.) A plot of $(E_{ph}I_{ph})^{1/2}$ as a function of E_{ph} for each of the materials examined showed a linear dependence, which indicated an indirect bandgap. An example of this dependence is shown in figures 29 and 30 for n-type $SnPS_3$ and p-type $FePS_3$. The intercept was the bandgap of the material. The bandgaps determined by this method for these crystals are listed in table III.

Experiments to determine the effect of solution pH on the onset potential showed a linear dependence up to PH-6. Figure 31 gives the data for $SnPS_3$. The curve has a slope of 59 mV/pH and indicates approximately Nernstian behavior of the onset potential for these layered materials.

The spectral response of the $SnPS_3$ photoelectrodes was investigated as a function of cell temperature in a pH-2 solution. The layered sample exhibited a broad response centered at 3 eV with a full width at half maximum of 1 eV as shown in figure 28. The granular samples have a much narrower response centered at 2.3 eV with a full width at half maximum of 0.15 eV as shown in figure 32. The effect of cell temperature on the spectral response of a granular $SnPS_3$ sample is also shown in figure 32. There is a dramatic shift of the response toward the red end of the spectrum with increasing temperature. A plot of the peak of the spectrum as a function of cell temperature is shown in figure 33. The shift of the peak is at a rate of

2.4 meV/K. This thermal shift, however, is not due to the change in the bandgap, since no significant change in the bandgap (≈2.1 eV) was observed.

The broadband photocurrent efficiencies of the $SnPS_3$ samples were on the order of 0.01 percent. The monochromatic quantum efficiency for light corresponding to the peak in the spectral responses of the two types of $SnPS_3$ crystals (2.3 eV for the granular $SnPS_3$ and 3.0 eV for the layered $SnPS_3$) was 8 percent and 40 percent, respectively.

Experiments were conducted using the layered crystals as a photosensitive electrode in a liquid-junction photovoltaic cell using a redox couple made up of iodide and tri-iodide in 1 M sulfuric acid. The materials previously found to be unstable were also unstable in the iodide-acid solution. The experimental photocurrent-voltage curve for n-type $SnPS_3$ in a solution of 1 M H_2SO_4, 0.025 M I_3, and 1 M I^- is shown in figure 34. Light from the 150-W xenon lamp was focused on the electrode. The open-circuit voltage was about 0.31 V, the fill factor was 0.38, and there was an efficiency of 4.5×10^{-2} percent. Other crystals showed low fill factors as well as low conversion efficiencies. This may be a result of surface recombination losses, high absorption of the incident radiation by the iodide solution, and high resistance exhibited by the layered materials.

In conclusion, a new class of layered transition metal thiophosphates of the type MPX3 were investigated for use as photoelectrodes in photoelectrochemical cells. Only $SnPS_3$, $NiPS_3$, and $FePS_3$ crystals were stable, and these were stable only in acid solutions. Crystals of $SnPS_3$ exhibited intrinsic and n- and p-type photocurrent characteristics. The iron-based and nickel-based sulfur compounds showed only p-type photocurrent-voltage characteristics. These materials had an indirect bandgap of about 2.1 eV and an onset potential near zero referenced to the SCE at pH-2. The onset potential for the stable materials was Nernstian between pH-0 and pH-7. These materials showed low conversion efficiencies when used as photoelectrodes in liquid-junction photovoltaic cells with iodide and tri-iodide as a redox couple. Based on these results, further research characterizing the growth conditions resulting in n- and p-type crystals, particularly for the sulfur-based crystals, as well as more extensive investigations with other redox couples will determine the utility of this class of compounds as photoelectrodes in photoelectrochemical cells.

11. HIGH-EFFICIENCY PHOTOELECTROCHEMICAL SYSTEM

Laser energy conversion efficiencies of 20 percent for the photoelectrolysis of water to gaseous hydrogen and oxygen in a $SrTiO_3$ based cell with a small applied voltage have been demonstrated by Wrighton et al. (ref. 16). The calculation of the conversion efficiency must account for this applied potential as

$$\eta = \frac{I_{ph}(1.48 - V_{app})}{\text{Light flux}} \tag{11.1}$$

where 1.48 is the reversible potential corresponding to the enthalpy for the reaction

$$2H_2 + O_2 \rightarrow 2H_2O \tag{11.2}$$

Elimination of the applied potential from equation (11.1) increases the conversion efficiency, and, for the case of a light flux from a laser, the efficiency is limited by the quantum efficiency of the particular photoelectrode. Approaching a 40-percent conversion efficiency for this $SrTiO_3$ system is feasible.

One scheme which successfully demonstrates that high laser conversion efficiencies can be achieved is shown in figure 35. Laser energy incident on a photoelectrode must pass through a window in the photoelectrochemical cell. A small portion of this laser energy is reflected from the window and would normally be a loss in the conversion process. However, placing a photovoltaic device, such as a Schottky barrier solar cell, in the reflected beam as shown in the figure can provide the required external bias necessary to achieve saturation and maximum efficiency.

A system, configured as shown schematically in figure 35, consisting of a single crystal of α-Fe_2O_3 as a photoanode in the photoelectrolysis cell and three silicon solar cells was used to demonstrate the principle of high laser-to-chemical energy conversion efficiency. The open-circuit voltage of the silicon solar cells with laser radiation having a photon energy of 2.4 eV was about 0.3 V. Figure 36 is the experimentally obtained photocurrent response of the iron-oxide crystal as a function of voltage. The response is shown as follows: (1) Unilluminated; (2) Illuminated with laser radiation at E_{ph} = 2.4 eV; (3) Illuminated using as a bias the portion of the laser radiation reflected from the cell window and surface of the iron-oxide crystal. The onset of the photocurrent shifts approximately 1 V with respect to the hydrogen half-cell potential. The principle of the technique is, therefore, verified by this result. Not only is the loss inherent in the reflection from the surfaces recovered, but also the photovoltaic cells utilize this energy to provide the bias needed to maximize the conversion efficiency by eliminating the need for externally derived power.

The current efficiency of a photoelectrochemical cell is also a function of externally applied voltage. This is particularly true of indirect bandgap materials such as α-Fe_2O_3 shown in figure 37. Peak current efficiency occurs for an external bias of 2.0 V at a laser photon energy of 3.5 eV. The bottom curve in figure 37 shows the maximum laser conversion efficiency as a function of laser photon energy in eV. The efficiency for converting laser radiation to hydrogen and oxygen peaks at 3.5 eV and is 15 percent if the 2.0-V bias is not accounted for.

The top curve of figure 38 gives the log of the quantum efficiency as a function of photon energy for single-crystal $SrTiO_3$. It should be noted that the quantum efficiency is unity for photon energies near 3.8 eV. Since the technique as demonstrated eliminates the bias previously required to achieve saturation current, laser conversion efficiency for this material and any other material is now determined by its spectral response. In the bottom curve of figure 38, the laser-to-chemical conversion efficiency is plotted as a function of the incident laser photon energy. The efficiency reaches 38 percent for laser photon energies of 3.8 eV.

Single-crystal photoelectrodes give the highest conversion efficiencies. Figure 39 shows that a polycrystalline material (WO_3) can also have reasonably high conversion efficiencies. This material is made by starting with metallic tungsten and then heating the metal in air at about 500°C until the oxide forms. The process is simple and therefore inexpensive. The laser-to-chemical conversion efficiency for this material reaches 6 percent at a laser photon energy of 2.8 eV.

Table IV shows the semiconductor materials that are stable during the photoelectrolysis process. Also included are their respective flatband potentials with respect to a reversible hydrogen electrode and the bias needed to give the maximum conversion efficiency. The last two columns give the energy of the laser photons and the maximum conversion efficiency. In every case, a bias of at least 1.5 V is required to achieve the highest efficiencies, and the energy of the required laser photons is in the ultraviolet. A Schottky barrier zinc-sulfide photovoltaic cell has its peak response in the uv and is capable of supplying the bias required for maximum efficiency. (The efficiencies cited herein are based on the enthalpy or energy evolved in the chemical recombination of hydrogen and oxygen to form water as would be the case, for example, for the combustion process taking place in a rocket engine.)

The highest efficiency, 38 percent, is obtained by an $SrTiO_3$ electrode, and the next highest efficiency (33 percent) is obtained by a TiO_2 electrode. A conversion efficiency of 6 percent can be achieved for a polycrystalline electrode of thermally grown tungsten trioxide.

Unsuccessful efforts were made to construct a ZnS photovoltaic cell to demonstrate the high conversion efficiencies. Therefore, the premise for high laser conversion efficiency with stable photoelectrodes is not fully demonstrated.

12. CONCLUDING REMARKS

An experimental and theoretical investigation of the semiconductor electrode has been carried out, and particular emphasis has been placed on the possibility of its use as part of a space power system. Using a semiclassical analysis, a model of the physical and chemical processes that occur when the electrode is illuminated has been developed. This model describes the static space-charge distribution within the semiconductor and the transport of photogenerated excess charge to the electrode-electrolyte interface, where it is transformed by a chemical reaction. Using an approximation to the charge transport equations, an estimate was made of the intensity of incident illumination at which the photogenerated carrier transport would saturate. Using $SrTiO_3$ electrodes, the saturation of photoeffects was observed with an argon-ion laser.

Experimentation on the temperature dependence of the broadband photocurrent for $SrTiO_3$ and TiO_2 photoelectrochemical cells demonstrates an increased efficiency with increasing temperature. This effect, which is attributed to the fact that the band-gap narrows with temperature, may prove useful in enhancing the solar conversion efficiency for liquid-junction solar cells.

The effect of temperature on the onset potential for the photocurrent was investigated for the metal-oxide electrodes Fe_2O_3, TiO_2, $SrTiO_3$, and WO_3. In aqueous electrolytes, the onset potential decreased linearly with increasing cell temperature. An analysis indicates that the slope of this curve is proportional to the point of zero zeta potential for the particular electrode material. The point of zero zeta potential determined in this way agrees well with the values obtained in the literature. These experiments have resulted in a new and nondestructive method for determining the point of zero zeta potential of macroscopic semiconductor materials.

The effect of platinized powdered TiO_2 on the photoproduction of the halogens from aqueous solutions of their respective ions was investigated. It was found that platinized TiO_2 powder was more effective in enhancing the desired reaction than unplatinized powder, and the reaction rates were higher at lower solution pH. Also, the production rate for the halogens is in the order $I_2 > Br_2 > Cl_2$ and is caused by the difference in the ability of the halide anions to compete with water for the photoproduced holes in the semiconductor. The demonstration of the photocatalytic production of chlorine and bromine from solutions of their ions in the presence of platinized powdered TiO_2 suggests an inexpensive industrial method for producing these chemicals.

Layered transition metal thiophosphate crystals were fabricated and tested for use as photoelectrodes in photoelectrochemical cells. Of the materials fabricated, only $SnPS_3$, $NiPS_3$, and $FePS_3$ were stable, and these were stable only in acid solutions. Crystals of $SnPS_3$ exhibited intrinsic n- and p-type photocurrent response. The iron-based and nickel-based sulfur compounds showed only p-type photocurrent-voltage characteristics. The materials had an indirect bandgap of about 2.1 eV and an onset potential near zero referenced to the saturated calomel electrode (SCE) at pH-2. These materials showed low conversion efficiencies when used as photoelectrodes in liquid-junction photovoltaic cells with iodide and tri-iodide as a redox couple.

The laser conversion efficiency of photoelectrochemical cells was explored using a technique of intercepting the light reflected from the window of the photoelectrochemical cell with a photovoltaic cell to provide the external bias needed to obtain the optimum conditions for conversion. The technique was demonstrated using α-Fe_2O_3 as the photoelectrode and three silicon solar cells with laser radiation energy of 2.4 eV. The silicon solar cells provided an external bias of 1.0 V using only the reflected laser radiation. On the basis of this technique, an efficiency of 38 percent can be achieved for the conversion of laser radiation to storable chemical energy in the form of hydrogen and oxygen. This can be achieved by using $SrTiO_3$ as a photoelectrode, zinc sulfide as the photovoltaic cell, and a laser photon energy of 3.8 eV.

Langley Research Center
National Aeronautics and Space Administration
Hampton, VA 23665
October 29, 1982

APPENDIX

SEMICONDUCTOR ENERGY-BAND MODEL

The simple energy-band model of a semiconductor is outlined in this appendix and provides the background for our treatment of the semiconductor electrode. This outline is included here to provide a concise statement of all the assumptions which underlie this work. Some of the details omitted in this appendix can be found in references 54 through 57.

This model is based upon a simplified view of energy-band structure, which is applicable to all direct bandgap semiconducting materials. The actual band structure of a material used as a semiconducting electrode is approximated by two energy bands, each with a single extremum aligned as shown in figure 40. The energy-momentum relation near an extremum at $k = 0$ can be approximated by the quadratic equation

$$E(k) = E(0) \pm \frac{h^2}{2m^*} k^2$$

where m^* is the effective mass of particles occupying states in that band. This leads to an expression for the density of states in the conduction band

$$\rho_c(E) = \begin{cases} 4\pi\left(\frac{2m_n^*}{h^2}\right)^{3/2} (E - E_C)^{1/2} & (E > E_C) \\ 0 & (E < E_C) \end{cases} \tag{A1}$$

and an expression for the density of states in the valence band

$$\rho_v(E) = \begin{cases} 0 & (E > E_V) \\ 4\pi\left(\frac{2m_p^*}{h^2}\right)^{3/2} (E_V - E)^{1/2} & (E < E_V) \end{cases} \tag{A2}$$

The density of states is represented graphically in figure 40.

APPENDIX

The equilibrium energy distribution of electrons about a Fermi energy E_F is contained in the Fermi distribution function

$$f(E) = \left[1 + \exp\left(\frac{E - E_F}{kT}\right)\right]^{-1} \tag{A3}$$

The concentration of electrons in the conduction band at thermodynamic equilibrium in the dark is given by the integral

$$n = \int_{E_C}^{\infty} \rho_c(E)\, f(E)\, dE \tag{A4}$$

and the concentration of holes in the valence band is given by the integral

$$p = \int_{-\infty}^{E_V} \rho_v(E)\left[1 - f(E)\right] dE \tag{A5}$$

After a change in variable, equations (A4) and (A5) can be rewritten as

$$n = 4\pi\left(\frac{2m_n^* kT}{h^2}\right)^{3/2} F_{1/2}\left(\frac{E_C - E_F}{kT}\right) \tag{A6}$$

and

$$p = 4\pi\left(\frac{2m_p^* kT}{h^2}\right)^{3/2} F_{1/2}\left(\frac{E_F - E_V}{kT}\right) \tag{A7}$$

The Fermi integral $F_{1/2}(x)$ is defined by

$$F_{1/2}(x) = \int_0^{\infty} s^{1/2}\left[1 + \exp(x + s)\right]^{-1} ds$$

A graph of this function appears in figure 41. If the independent variable in the Fermi integral above is larger than 3, the integral can be approximated and evaluated in closed form as

$$F_{1/2}(x) \approx \int_0^\infty s^{1/2} \exp[-x - s]\, ds = \frac{\pi}{2} \exp(-x) \tag{A8}$$

In this case the variable x is either $\frac{E_C - E_F}{kT}$ or $\frac{E_F - E_V}{kT}$. If the Fermi energy is at least 3kT away from either the conduction band edge or the valence band edge, the concentration of electrons and holes can be approximated by the Boltzmann distribution as follows:

$$n = N_C \exp\left(-\frac{E_C - E_F}{kT}\right) \tag{A9}$$

with

$$N_C = 2\left(\frac{2\pi m_n^* kT}{h^2}\right)^{3/2}$$

and

$$p = N_V \exp\left(-\frac{E_F - E_V}{kT}\right) \tag{A10}$$

with

$$N_V = 2\left(\frac{2\pi m_p^* kT}{h^2}\right)^{3/2}$$

At room temperature, the factor 3kT has a value smaller than 0.1 eV, so it is reasonable to use Boltzmann statistics in equations (A9) and (A10) to describe electron and hole concentrations at these temperatures. The product of the charge carrier concentrations gives an expression that depends simply upon the energy gap, namely

$$np = N_C N_V \exp\left(-\frac{E_G}{kT}\right) \tag{A11}$$

APPENDIX

In an intrinsic semiconductor (chemically pure, single crystal), the only charge comes from thermally excited electrons and holes. The bulk of the semiconductor must be electrically neutral. Charge neutrality is specified by the condition

$$n - p = 0$$

which we express in terms of the intrinsic carrier concentration n_i by

$$n = n_i = p \tag{A12}$$

Substituting the Boltzmann distributions for n and p, equations (A9) and (A10) into equation (A12), the Fermi energy for an intrinsic semiconducting material is related to the semiconductor parameters by

$$E_{F,I} = \frac{1}{2}(E_V + E_C) + \frac{kT}{2} \ln\left(\frac{N_V}{N_C}\right) \tag{A13}$$

or

$$E_{F,I} = \frac{1}{2}(E_V + E_C) + \frac{3kT}{4} \ln\left(\frac{m_p^*}{m_n^*}\right) \tag{A14}$$

This value of the intrinsic Fermi energy provides a reference level against which other energies can be conveniently measured. Its value is approximately half way between the energies of the valence and the conduction band edges so that it satisfies the conditions required for the use of Boltzmann statistics. The intrinsic carrier concentration, defined by equation (A12), can be expressed in terms of the energy gap using equation (A11) as follows:

$$n_i = \sqrt{N_C N_V} \exp\left(-\frac{E_G}{2kT}\right) \tag{A15}$$

In a semiconducting crystal that is not chemically pure or nonstoichiometric (a nonintrinsic semiconductor), the condition of charge neutrality in the bulk given by equation (A12) must be modified to reflect the statistical charge distribution associated with impurities or imperfections within the crystal. This modification depends upon structural details of the nonintrinsic semiconductor which are not often available. In this paragraph, a simple picture of donor- and acceptor-atom occupation statistics that provides an approximate treatment of the problem of occupation statistics of impurity levels is described. This description is similar to that in references 57 through 60, but other more exact treatments can be found elsewhere (refs. 61 and 62). If the nonintrinsic effects are considered to be caused by a single localized one-electron state of energy E_s communicating with the crystal by

electron transfer, the probability that the level is occupied by an electron or hole is given by

$$f(E) = \left[1 + \frac{g}{g^*} \exp\left(\frac{E_s - E_F}{kT}\right)\right]^{-1}$$

where g is the number of degenerate states associated with the vacant level, and g^* is the number of states associated with the occupied level. By representing the ratio of degeneracy in the form

$$g/g^* = \exp\left(\frac{\Delta E}{kT}\right)$$

the probability of occupancy can be written in terms of a single parameter, the effective energy level E_s^*, by the usual Fermi distribution function

$$f\left(E_s^*\right) = 1 + \exp\left(\frac{E_s^* - E_F}{kT}\right) \tag{A16}$$

where

$$E_s^* = E_s + \Delta E = E_s + kT \ln\left(\frac{g}{g^*}\right) \tag{A17}$$

As shown in equation (A17), the effect of the degeneracy of states at room temperature is minimal.

The semiconductor is assumed to have a concentration of acceptors N_A with energy level E_A just above the valence-band energy, and a concentration of donors N_D with energy level E_D just below the conduction-band energy. (See fig. 42.) The density of electrons occupying donor levels (un-ionized donors) n_D and the density of holes occupying acceptor levels (un-ionized acceptors) p_A obtained from equation (A16) are then expressed by the equations

$$n_D = N_D\left[1 + \exp\left(\frac{E_D^* - E_F}{kT}\right)\right]^{-1} \tag{A18}$$

and

$$p_A = N_A\left[1 + \exp\left(\frac{E_F - E_A^*}{kT}\right)\right]^{-1} \tag{A19}$$

The condition for charge neutrality in the bulk requires that the total number of negative charges, electrons plus ionized acceptors $n + N_A - p_A$ be equal to the total number of positive charges, holes, and ionized donors $p + N_D - n_D$ This condition can be expressed by the equation

$$n - p = N_A\left\{1 - \left[1 + \exp\left(\frac{E_A^* - E_F}{kT}\right)\right]^{-1}\right\} - N_D\left\{1 - \left[1 + \exp\left(\frac{E_F - E_D^*}{kT}\right)\right]^{-1}\right\} \tag{A20}$$

When the Fermi energy differs from either effective ionization energy (E_A or E_D) and is between them, complete ionization is expected, and in this case the condition for charge neutrality becomes

$$n - p = N_D - N_A \tag{A21}$$

Assuming that the electron and hole concentrations are governed by Boltzmann statistics (eqs. (A9) and (A10)), the following relation involving the Fermi energy and the other characteristics of the semiconductor can be derived:

$$\sinh\left[\frac{E_G}{kT}(P - \delta)\right] = \frac{N_D - N_A}{2n_i} \tag{A22}$$

where

$$P = \frac{E_F - E_V}{E_C}$$

and

$$\delta = \frac{1}{2}\left[1 + kT\ \ln\left(\frac{N_C}{N_V}\right)\right]$$

APPENDIX

By solving for the Fermi energy directly, we obtain for the case of an n-type semiconductor

$$E_F = E_{F,I} + kT \ln\left(\frac{n}{n_i}\right) \tag{A23}$$

and a p-type semiconductor

$$E_F = E_{F,I} - kT \ln\left(\frac{p}{n_i}\right) \tag{A24}$$

is obtained.

REFERENCES

1. Fujishima, Akira; and Honda, Kenichi: Electrochemical Photolysis of Water at a Semiconductor Electrode. Nature, vol. 238, no. 5358, July 7, 1972, pp. 37-38.

2. Fujishima, Akira; and Honda, Kenichi: Photosensitive Electrode Reactions. III. Electrochemical Evidence for the Mechanism of the Primary Stage of Photosynthesis. Bull. Chem. Soc. Japan, vol. 44, no. 4, 1971, pp. 1148-1150.

3. Bard, Allen J.: Photoelectrochemistry. Science, vol. 207, no. 4427, Jan. 11, 1980, pp. 139-144.

4. Nozik, A. J.: Photoelectrochemical Cells. Philos. Trans. R. Soc. London, ser. A, vol. 295, no. 1414, Feb. 7, 1980, pp. 453-470.

5. Tomkiewicz, M.; and Fay, H.: Photoelectrolysis of Water With Semiconductors. Appl. Phys., vol. 18, no. 1, Jan. 1979, pp. 1-28.

6. Harris, L. A.; and Wilson, R. H.: Semiconductors for Photoelectrolysis. Annual Review of Materials Science, Volume 8, Robert A. Huggins, ed., Annu. Rev., Inc., 1978, pp. 99-134.

7. Thomchick, John; and Buoncristiani, A. M.: An Alternative Approach to Charge Transport in Semiconducting Electrodes. J. Appl. Phys., vol. 51, no. 12, Dec. 1980, pp. 6265-6272.

8. Thomchick, John; and Buoncristiani, A. M.: Field-Dependent Transport Through the Depletion Layer of a Semiconducting Electrode. J. Appl. Phys., vol. 52, no. 12, Dec. 1981, pp. 7296-7303.

9. Maruska, H. Paul; and Ghosh, Amal K.: Photocatalytic Decomposition of Water at Semiconductor Electrodes. Sol. Energy, vol. 20, no. 6, 1978, pp. 443-458.

10. Delahay, Paul: Double Layer and Electrode Kinetics. Interscience Pub., c.1965.

11. Parsons, Roger: Equilibrium Properties of Electrified Interphases. Modern Aspects of Electrochemistry, J. O'M. Bockris, ed., Butterworths Scientific Publ., 1954, pp. 103-179.

12. Bootsma, G. A.; De Rooij, N. F.; and Van Silfhout, A.: The Solid/Liquid Interface. Sens. & Actuators, vol. 1, no. 2, Apr. 1981, pp. 111-136.

13. Gerischer, Heinz: Electrochemical Photo and Solar Cells. Principles and Some Experiments. J. Electroanal. Chem. Interfacial Electrochem., vol. 58, no. 1, 1975, pp. 263-274.

14. Morrison, S. Roy: Study of Semiconductors Using Electrochemical Techniques. J. Vac. Sci. Technol., vol. 15, no. 4, July/Aug. 1978, pp. 1417-1421.

15. Watanabe, Tadashi; Fujishima, Akira; and Honda, Kenichi: Photoelectrochemical Reactions at a Strontium Titanate Single Crystal Electrode. Bull. Chem. Soc. Japan, vol. 49, no. 2, 1976, pp. 355-358.

16. Wrighton, Mark S.; Ellis, Arthur B.; Wolczanski, Peter T.; Morse, David L.; Abrahamson, Harmon B.; and Ginley, David S.: Strontium Titanate Photoelectrodes. Efficient Photoassisted Electrolysis of Water at Zero Applied Potential. J. American Chem. Soc., vol. 98, no. 10, May 12, 1976, pp. 2774-2779.

17. Mavroides, J. G.; Kafalas, J. A.; and Kolesar, D. F.: Photoelectrolysis of Water in Cells with $SrTiO_3$ Anodes. Appl. Phys. Lett., vol. 28, no. 5, Mar. 1, 1976, pp. 241-243.

18. Bocarsly, Andrew B.; Bolts, Jeffrey M.; Cummins, Phillip G.; and Wrighton, Mark S.: Photoelectrolysis of Water at High Current Density: Use of Ultraviolet Laser Excitation. Appl. Phys. Lett., vol. 31, no. 9, Nov. 1, 1977, pp. 568-570.

19. Valdes, L. B.: Resistivity Measurements on Germanium for Transistors. Proc. IRE, vol. 42, no. 2, Feb. 1954, pp. 420-427.

20. Capizzi, M.; and Frova, A.: Determination of the Nature of the Optical Gap of $SrTiO_3$ Nuovo Cimento Soc. Ital. Fis. B, vol. 5, no. 2, Oct. 11, 1971, pp. 181-203.

21. Cohen, M. I.; and Blunt, R. F.: Optical Properties of $SrTiO_3$ in the Region of the Absorption Edge. Phys. Rev., vol. 168, no. 3, Apr. 15, 1968, pp. 929-933.

22. Wemple, S. H.: Polarization Fluctuations and the Optical-Absorption Edge in $BaTiO_3$. Phys. Rev., ser. B, vol. 2, no. 7, Oct. 1, 1970, pp. 2679-2689.

23. Moss, T. S.; Burrell, G. J.; and Ellis, B.: Semiconductor Opto-Electronics. John Wiley & Sons, Inc., c.1973.

24. Neville, R. C.; and Mead, C. A.: Surface Barrier Energies on Strontium Titanate. J. Appl. Phys., vol. 43, no. 11, Nov. 1972, pp. 4657-4663.

25. Butler, M. A.; and Ginley, D. S.: Correlation of Photosensitive Electrode Properties With Electronegativity. Chem. Phys. Lett., vol. 47, no. 2, Apr. 15, 1977, pp. 319-321.

26. Butler, M. A.; and Ginley, D. S.: Prediction of Flatband Potentials at Semiconductor-Electrolyte Interfaces From Atomic Electronegativities. J. Electrochem. Soc., vol. 125, no. 2, Feb. 1978, pp. 228-232.

27. Butler, M. A.; and Ginley, D. S.: Temperature Dependence of Flatband Potentials at Semiconductor-Electrolyte Interfaces. Nature, vol. 273, no. 5663, June 15, 1978, pp. 524-525.

28. Byvik, Charles E.; Koons, Lawrence F.; and Reichman, Benjamin: Photocurrent Response of TiO_2 and $SrTiO_3$ Anodes in a High-Temperature Photoelectrochemical Cell. Abstract No. 356, The Electrochemical Society - 157th Meeting, May 1980, pp. 885-887.

29. Reichman, Benjamin; and Byvik, Charles E.: Photovoltage Response to Temperature Change at Oxide Semiconductor Electrodes. J. Electrochem. Soc., vol. 128, no. 12, Dec. 1981, pp. 2601-2603.

30. Tomkiewicz, Micha: The Nature of Surface States on Chemically Modified TiO_2 Electrodes. J. Electrochem. Soc., vol. 127, no. 7, July 1980, pp. 1518-1525.

31. Frank, Steven N.; and Bard, Allen J.: Semiconductor Electrodes. 12. Photoassisted Oxidations and Photoelectrosynthesis at Polycrystalline TiO_2 Electrodes. J. American Chem. Soc., vol. 99, no. 14, July 6, 1977, pp. 4667-4675.

32. Fujishima, Akira; Inoue, Tooru; and Honda, Kenichi: Competitive Photoelectrochemical Oxidation of Reducing Agents at the TiO_2 Photoanode. J. American Chem. Soc., vol. 101, no. 19, Sept. 12, 1979, pp. 5582-5588.

33. Kraeutler, Bernhard; and Bard, Allen J.: Heterogeneous Photocatalytic Synthesis of Methane From Acetic Acid - New Kolbe Reaction Pathway. J. American Chem. Soc., vol. 100, no. 7, Mar. 29, 1978, pp. 2239-2240.

34. Kraeutler, Bernhard; and Bard, Allen J.: Heterogeneous Photocatalytic Preparation of Supported Catalysts. Photodeposition of Platinum on TiO_2 Powder and Other Substrates. J. American Chem. Soc., vol. 100, no. 13, June 21, 1978, pp. 4317-4318.

35. Kraeutler, Bernhard; and Bard, Allen J.: Heterogeneous Photocatalytic Decomposition of Saturated Carboxylic Acids on TiO_2 Powder. Decarboxylative Route to Alkanes. J. American Chem. Soc., vol. 100, no. 19, Sept. 13, 1978, pp. 5985-5992.

36. Frank, Steven N.; and Bard, Allen J.: Heterogeneous Photocatalytic Oxidation of Cyanide Ion in Aqueous Solutions at TiO_2 Powder. J. American Chem. Soc., vol. 99, no. 1, Jan. 5, 1977, pp. 303-304.

37. Frank, Steven N.; and Bard, Allen J.: Heterogeneous Photocatalytic Oxidation of Cyanide and Sulfite in Aqueous Solutions at Semiconductor Powders. J. Phys. Chem., vol. 81, no. 15, July 28, 1977, pp. 1484-1488.

38. Reiche, H.; and Bard, A. J.: Heterogeneous Photosynthetic Production of Amino Acids From Methane-Ammonia-Water at Pt/TiO_2. Implications in Chemical Evolution. J. American Chem. Soc., vol. 101, no. 11, May 23, 1979, pp. 3127-3128.

39. Izumi, Ikuichiro; Dunn, Wendell, W.; Wilbourn, Keith O.; Fan, Fu-Ren F.; and Bard, Allen J.: Heterogeneous Photocatalytic Oxidation of Hydrocarbons on Platinized TiO_2 Powders. J. Phys. Chem., vol. 84, no. 24, Nov. 27, 1980, pp. 3207-3210.

40. Reiche, Harold; Dunn, Wendell W.; and Bard, Allen J.: Heterogeneous Photocatalytic and Photosynthetic Deposition of Copper on TiO_2 and WO_3 Powders. J. Phys. Chem., vol. 83, no. 17, Aug. 23, 1979, pp. 2248-2251.

41. Inoue, Tooru; Fujishima, Akira; Konishi, Satoshi; and Honda, Kenichi: Photoelectrocatalytic Reduction of Carbon Dioxide in Aqueous Suspensions of Semiconductor Powders. Nature, vol. 277, no. 5698, Feb. 22, 1979, pp. 637-638.

42. Reichman, Benjamin; and Byvik, Charles E.: Photoproduction of I_2, Br_2, and Cl_2 on n-Semiconducting Powder. J. Phys. Chem., vol. 85, no. 15, July 23, 1981, pp. 2255-2258.

43. Wrighton, Mark S.; Wolczanski, Peter T.; and Ellis, Arthur B.: Photoelectrolysis of Water by Irradiaton of Platinized n-Type Semiconducting Metal Oxides. J. Solid State Chem., vol. 22, 1977, pp. 17-29.

44. Laser, Daniel; and Bard, Allen J.: Semiconductor Electrodes. VI. A Photoelectrochemical Solar Cell Employing a TiO_2 Anode and Oxygen Cathode. J. Electrochem. Soc., vol. 123, no. 7, July 1976, pp. 1027-1030.

45. Kautek, W.; Gobrecht, J.; and Gerischer, H.: The Applicability of Semiconducting Layered Materials for Electrochemical Solar Energy Conversion. Ber. Bunsenges. Phys. Chem., vol. 84, no. 10, 1980, pp. 1034-1040.

46. Tributsch, H.: Solar Energy-Assisted Electrochemical Splitting of Water. Z. Naturforsch., Teil A, vol. 32, no. 9, Sept. 1977, pp. 972-985.

47. Tributsch, H.; and Bennett, J. C.: Electrochemistry and Photochemistry of Molybdenum Disulfide Layer Crystals. I. J. Electroanal. Chem. Interfacial Electrochem., vol. 81, no. 1, 1977, pp. 97-111.

48. Tributsch, Helmut: The Molybdenum (IV) Selenide Electrochemical Solar Cell: Anodic Coupling of Electron Transfer to d → d Photo-Transitions in Layer Crystals. Ber. Bunsenges. Phys. Chem., vol. 82, no. 2, 1978, pp. 169-174.

49. Tributsch, Helmut: Hole Reactions From d-Energy Bands of Layer Type Group VI Transition Metal Dichalcogenides: New Perspectives for Electrochemical Solar Energy Conversion. J. Electrochem. Soc., vol. 125, no. 7, July 1978, pp. 1086-1093.

50. Fan, Fu-Ren F.; White, Henry S.; Wheeler, Bob; and Bard, Allen J.: Semiconductor Electrodes. XXIX. High Efficiency Photoelectrochemical Solar Cells with n-WSe_2 Electrodes in an Aqueous Iodide Medium. J. Electrochem. Soc., vol. 127, no. 2, Feb. 1980, pp. 518-520.

51. Fornarini, L.; Stirpe, F.; Scrosati, B.; and Razzini, G.: Electrochemical Solar Cells With Layer-Type Semiconductor Anodes. Performance of n-MoS_2 Cells. Sol. Energy Mater., vol. 5, no. 1, June/July 1981, pp. 107-114.

52. Byvik, Charles E.; Reichman, Benjamin; and Coleman, David W.: Photoelectrochemical Response of Some Layered Chalcogenophosphate Compounds (MPX3). J. Electrochem. Soc., vol. 129, no. 1, Jan. 1982, pp. 237-238.

53. Nitsche, R.; and Wild, P.: Crystal Growth of Metal-Phosphorous-Sulfur Compounds by Vapor Transport. Mater. Res. Bull., vol. 5, no. 6, June 1970, pp. 419-424.

54. Nitsche, Rudolf: Crystal Growth From the Gas Phase by Chemical Transport Reactions. Fortschr. Mineral., vol. 44, no. 2, 1967, pp. 231-287.

55. Stern, Frank: Elementary Theory of the Optical Properties of Solids. Solid State Physics, Vol. 15, Frederick Seitz and David Turnbull, eds., Academic Press, Inc., 1963, pp. 299-408.

56. Johnson, Earnest J.: Absorption Near the Fundamental Edge. Semiconductors and Semimetals. Volume 3 - Optical Properties of III-V Compounds, R. K. Willardson and Albert C. Beer, eds., Academic Press, Inc., 1967, pp. 153-258.

57. Many, A.; Goldstein, Y.; and Grover, N. B.: Semiconductor Surfaces. North-Holland Pub. Co. (Amsterdam), 1971.

58. Sze, S. M.: Physics of Semiconductor Devices. John Wiley & Sons, Inc., c.1969.

59. Morrison, S. Roy: The Chemical Physics of Surfaces. Plenum Press, Inc., c.1977.

60. Madelung, O. (B. C. Taylor, transl.): Introduction to Solid-State Theory. Springer-Verlag Berlin Heidelberg, 1978.

61. Seitz, Frederick: The Modern Theory of Solids. McGraw-Hill Book Co., Inc., 1940.

62. Shockley, W.; and Last, J. T.: Statistics of the Charge Distribution for a Localized Flaw in a Semiconductor. Phys. Rev., vol. 107, no. 2, July 15, 1957, pp. 392-396.

TABLE I.- COMPARISON OF pH AT POINT OF ZERO ZETA POTENTIAL (pH_{pzzp}) DETERMINED FOR TWO-SOLUTION pH VALUES WITH VALUES CITED IN LITERATURE FOR OXIDE-SEMICONDUCTOR ELECTRODES

Electrode	pH at 25°C	V_{FB} ref. RHE[a] at 25°C	Slope,[b] mV/deg	n,[c] cm^{-3}	N_C, cm^{-3}	pH_{pzzp}	Average pH_{pzzp}	Literature pH_{pzzp}
Fe_2O_3	2 13	0.5 .4	2.9 2.7	5.1×10^{17}	2.4×10^{22}	9.8 8.8	9.3	8.6
$SrTiO_3$	2 13	-0.18 -.24	2.25 2.4	3.2×10^{17}	6.8×10^{19}	8.9 9.7	9.3	8.6
TiO_2	2 13	0.11 -.07	1.15 1.5	6.2×10^{17}	3.0×10^{21}	4.1 5.8	5.0	5.8
WO_3	2	0.53	0.1	7.6×10^{19}	9.8×10^{18}	0.5	0.5	0.43

[a]Semiconductor parameter used in equation (8.2).
[b]Taken from figure 20.
[c]Determined from Mott-Schottky plots.

TABLE II.- COMPARISON OF HALOGEN PRODUCTION FOR CATALYSTS AND pH VALUES

Solution	pH[a]	Catalyst[b]	Irradiation time,[c] hours	Amount produced, micromole
1.7 M KBr	[d]7.0	100 mg Pt-TiO_2	1	[e]140
1.7 M NaCl	[d]7.0	100 mg Pt-TiO_2	1	[e]98
2.0 M KI	5.5	None	2	1.4
2.0 M KI	5.5	150 mg Al_2O_3	2	2.3
2.0 M KI	5.5	150 mg TiO_2	2	3.5
2.0 M KI	5.5	150 mg Pt-TiO_2	2	4.9
2.0 M KI	5.5	150 mg Pt-TiO_2	4	[f]10.8
2.0 M KI	2.0	150 mg Pt-TiO_2	2	158
3.0 M KBr	5.5	150 mg TiO_2	40	1.3
3.0 M KBr	5.5	150 mg Pt-TiO_2	3	.9
3.0 M KBr	5.5	150 mg Pt-TiO_2	23	6.2
3.0 M KBr	1.8	150 mg Pt-TiO_2	3	11
3.0 M NaCl	5.5	150 mg Pt-TiO_2	3	0.9
3.0 M NaCl	5.5	200 mg Pt-TiO_2	24	2.6
3.0 M NaCl	1.2	150 mg TiO_2	40	4
3.0 M NaCl	1.2	150 mg Pt-TiO_2	3	13
3.0 M NaCl	1.2	150 mg Pt-TiO_2	20	40

[a]Adjusted by adding H_2SO_4 or $NaHCO^3$.

[b]Pt-TiO_2 prepared according to reference 34 with doped TiO_2 anatase. TiO_2 powder was undoped anatase.

[c]1000-W high-pressure Hg lamp irradiated through glass window.

[d]Adjusted by adding $NaHCO_3$.

[e]Determined by initially introducing a known amount of As(III) to the cell. The As(III) also reacted, but at a lower rate than the halide as determined by blank experiments.

[f]Determined by continuously passing oxygen through the cell and through two external traps, each containing 35 ml of 2-M KI solution, and by titrating with As(III) both the I_2 in the irradiated cell and the I_2 trapped in the two external traps.

TABLE III.- CRYSTAL GROWTH CONDITIONS, ONSET POTENTIALS, BANDGAP, AND CONDUCTIVITY TYPE OF LAYERED TRANSITION-METAL THIOPHOSPHATES

Material	T_{high}, °C	T_{low}, °C	V_{op} ref. SCE at pH-2	E_{gap}, eV	Conductivity type
$SnPS_3$	630	600	0	2.15	n, p
$FePS_3$	670	620	0	2.18	p
$NiPS_3$	670	620	.2	2.0	p
$SnPSe_3$	630	600	0	(a)	n
$MnPS_3$	700	620	-.1	↓	n
$BiPS_4$	660	610	-.3	↓	Intrinsic
$CoPS_2$	670	620	(b)	(b)	(b)
$CrPS_3$	670	620	↓	↓	↓
$FePSe_3$	670	620			
$GaPS_2$	450	430			

[a]Undertermined.
[b]No photoresponse.

TABLE IV.- MAXIMUM LASER-TO-CHEMICAL ENERGY CONVERSION EFFICIENCIES FOR SEMICONDUCTOR-BASED PHOTOELECTROLYTIC CELLS

Semiconductor	V_{FB} ref. RHE	Bias, V	Laser photon energy, eV	Maximum efficiency, percent
WO_3	0.4	4	2.8	6
TiO_2	-.1	1.5 to 2	3.5	33
$SrTiO_3$	-.4	1.5 to 2	3.8	38
α-Fe_2O_3	.4	2	3.5	15
$BaTiO_3$	-.2	1.5 to 2	3.9	
$KTaO_3$	-.3	1.5	5.0	15
$KTa_{0.77}Nb_{0.23}O_3$	-.3	1.5	5.0	10

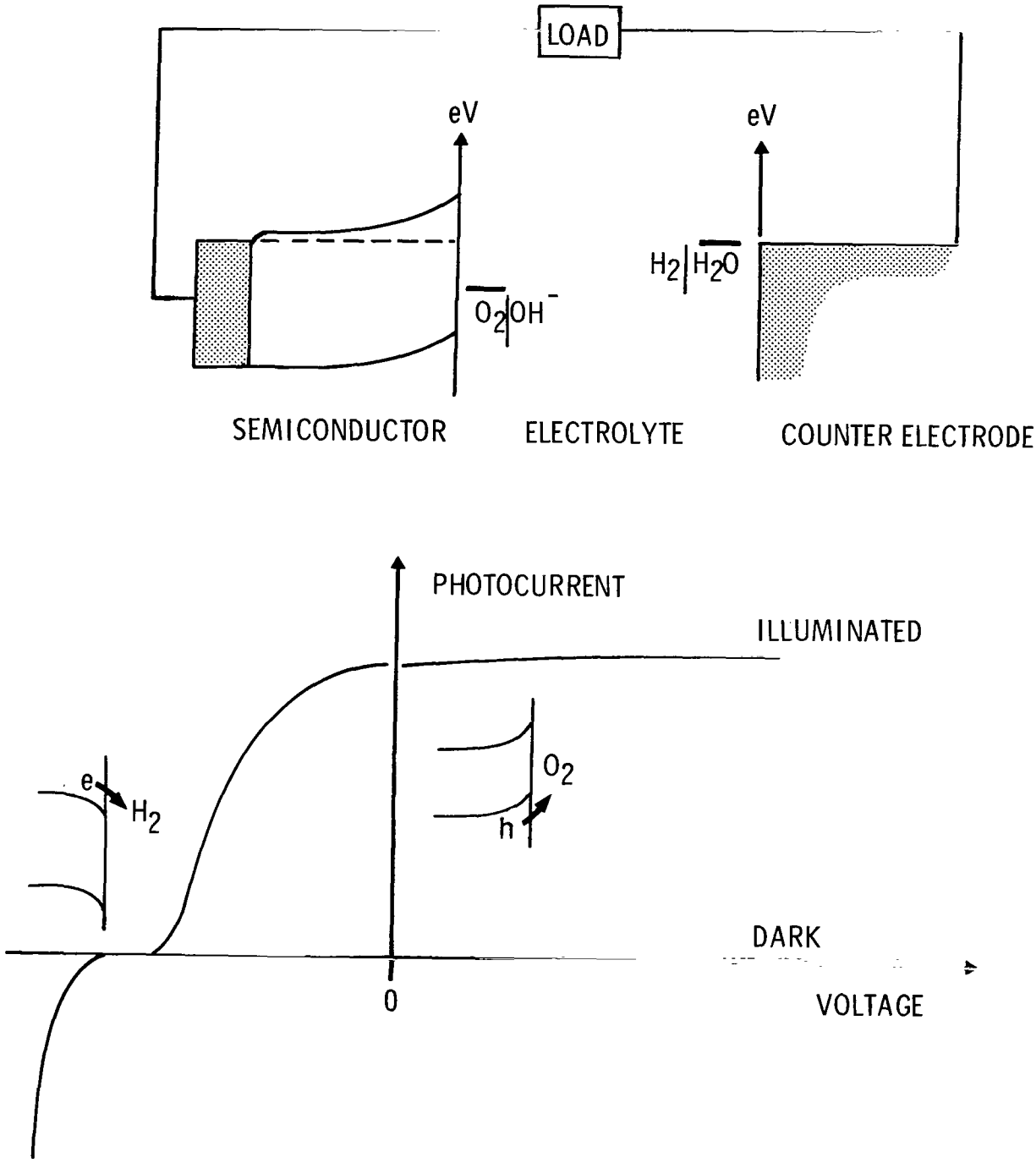

Figure 1.- Schematic of a photoelectrochemical cell and current-voltage response for dark and illuminated conditions.

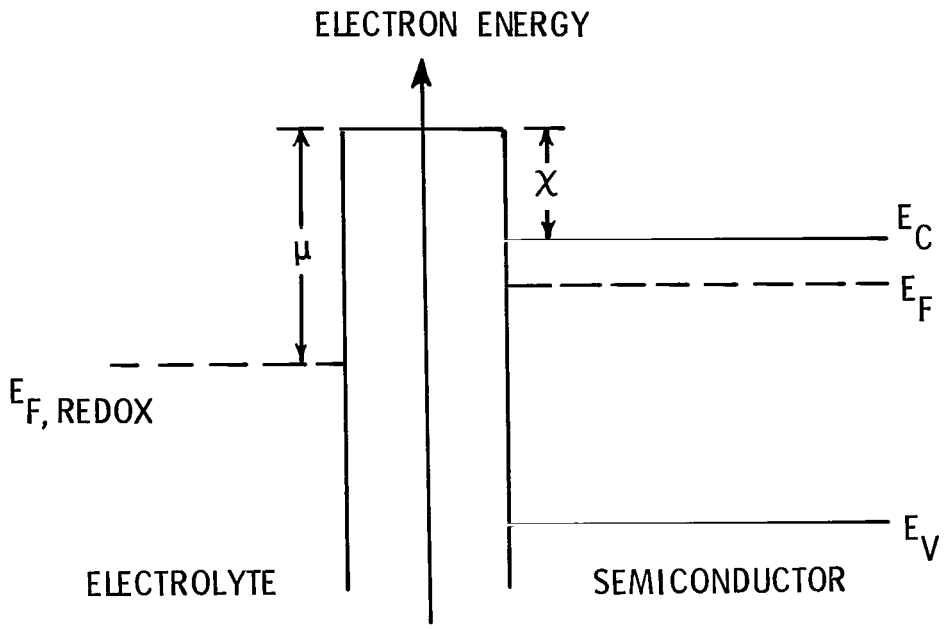

(a) Before charge redistribution.

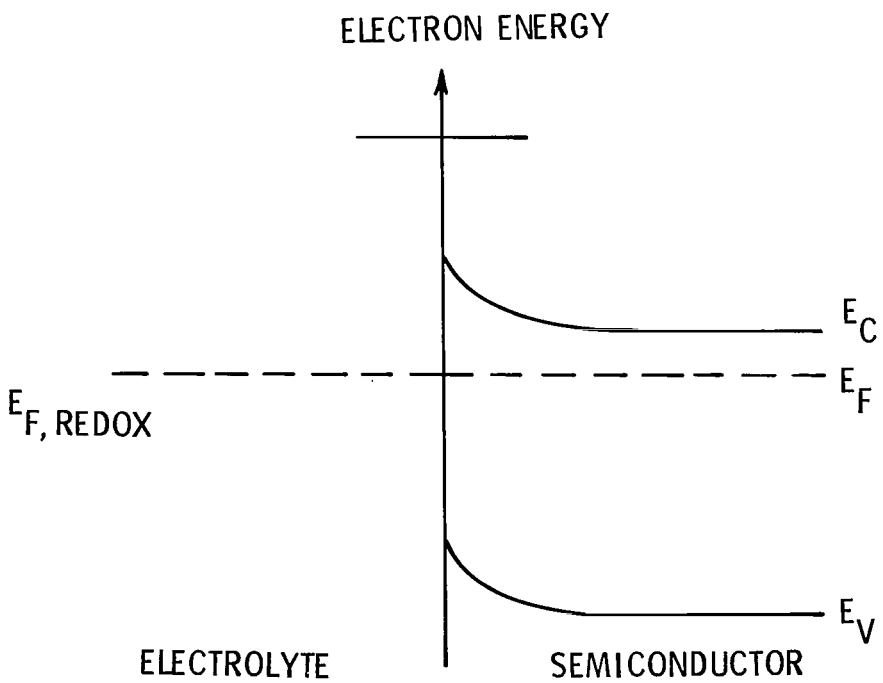

(b) After charge redistribution.

Figure 2.- Schematic of energy levels in an n-type semiconductor electrode and electrolyte.

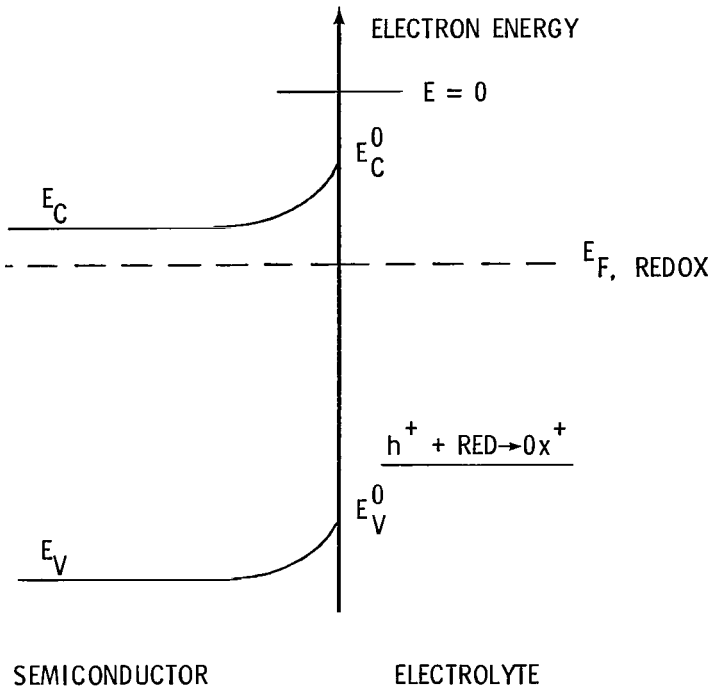

Figure 3.- Energy-band diagram of an n-type semiconductor-electrolyte interface.

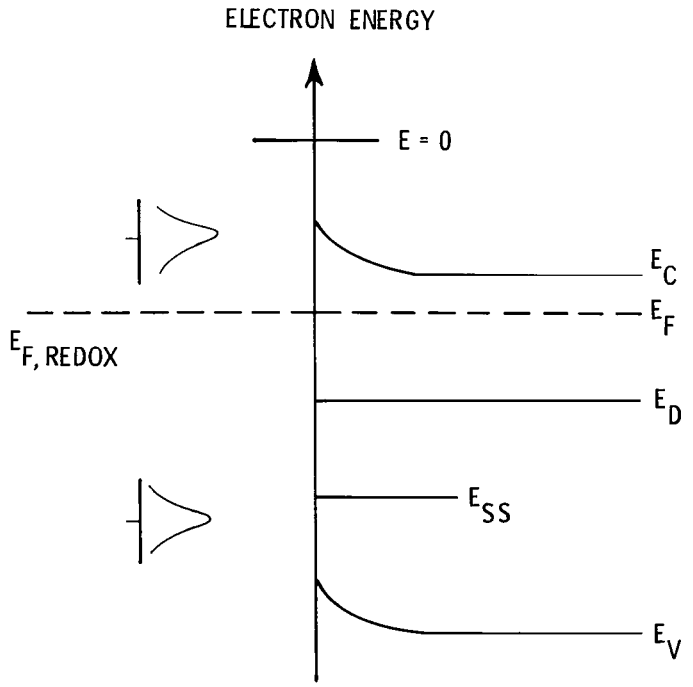

Figure 4.- Schematic of redox levels in electrolyte showing dissociation energy and surface states.

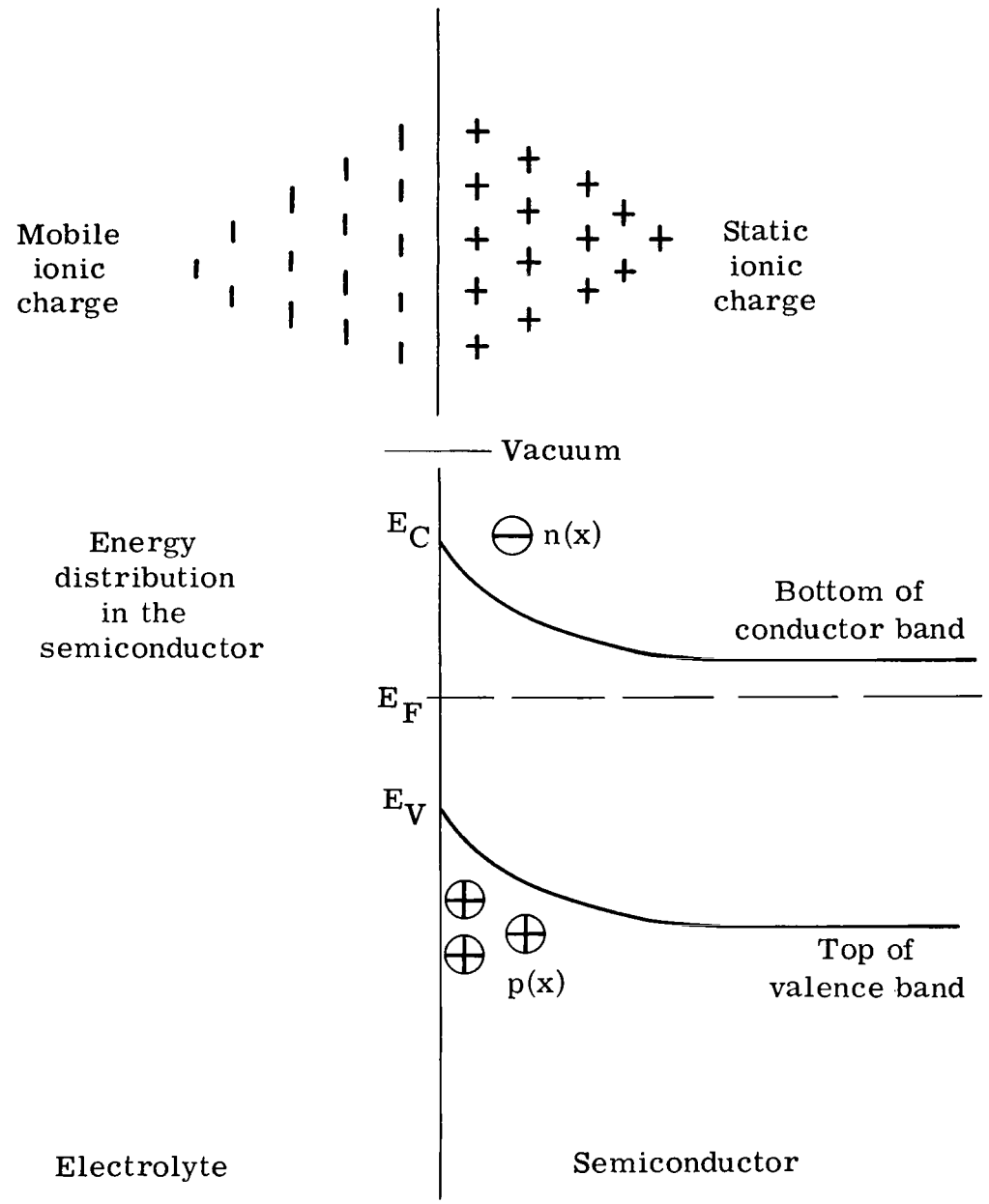

Figure 5.- Ionic charge distribution in the semiconductor-electrolyte interfacial region. Potential of this electrostatic field due to ionic and mobile charge distributions is shown in bottom half of sketch. An n-type semiconductor depletion region is assumed.

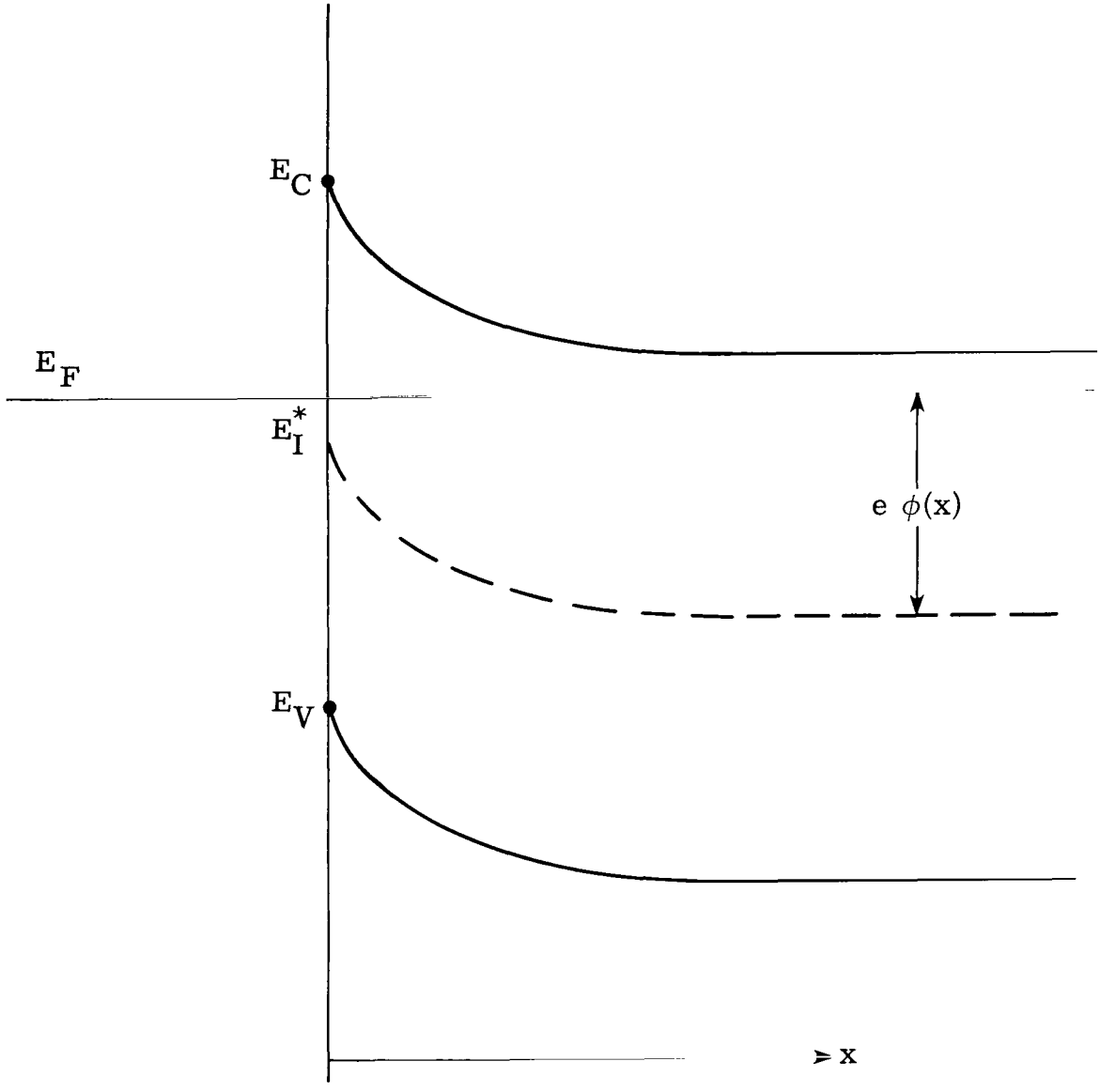

$$e\,\phi(x) \equiv E_F - E_I^*(x)$$

Figure 6.- Schematic of band bending at surface of n-type semiconductor.

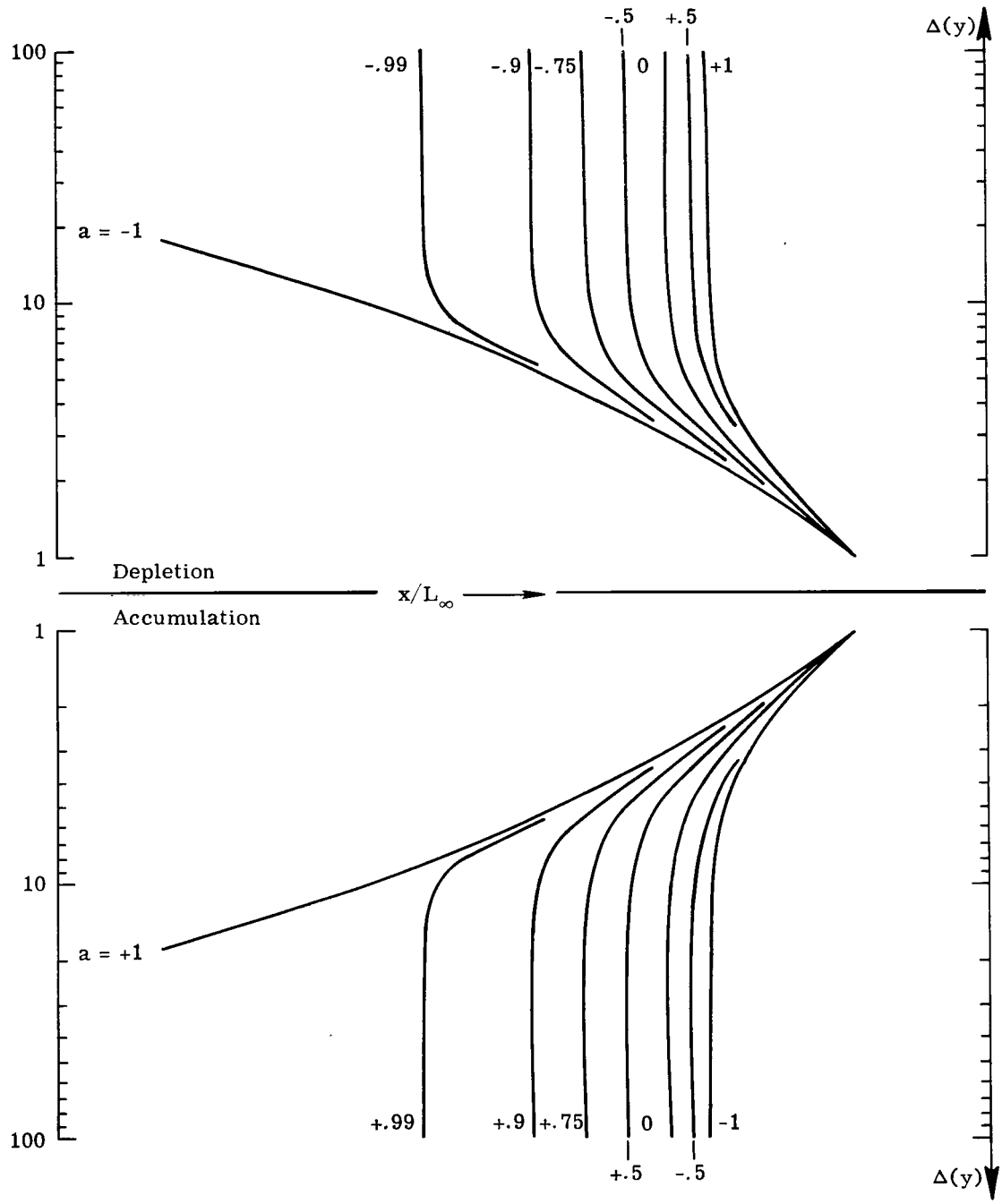

Figure 7.- Solutions to Poisson-Boltzmann equation. Dimensionless penetration parameter is plotted along abscissa. No origin of this coordinate is defined in graph, so $y = 0$ can be established beneath any specified initial value of $\Delta(0)$. Upper curves represent charge distribution in depletion region. Lower curves represent charge distribution in accumulation region.

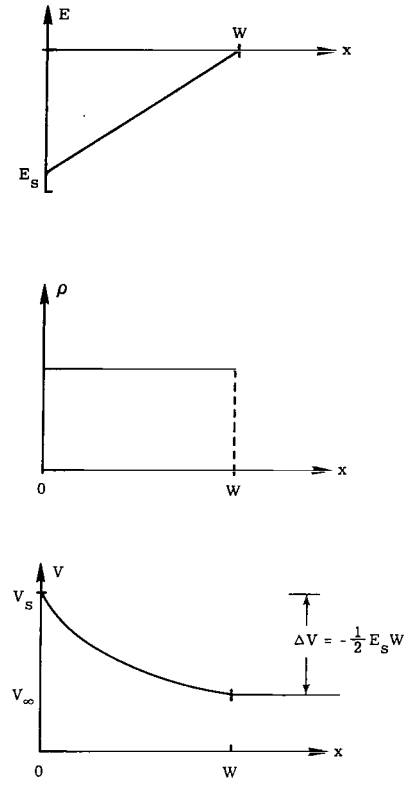

Figure 8.- Electric field, charge density, and potential distribution for abrupt approximation.

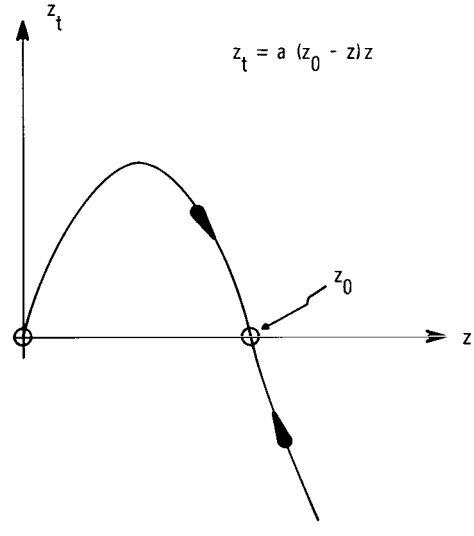

Figure 9.- Quadratic nonlinear equation of charge concentration and its phase portrait.

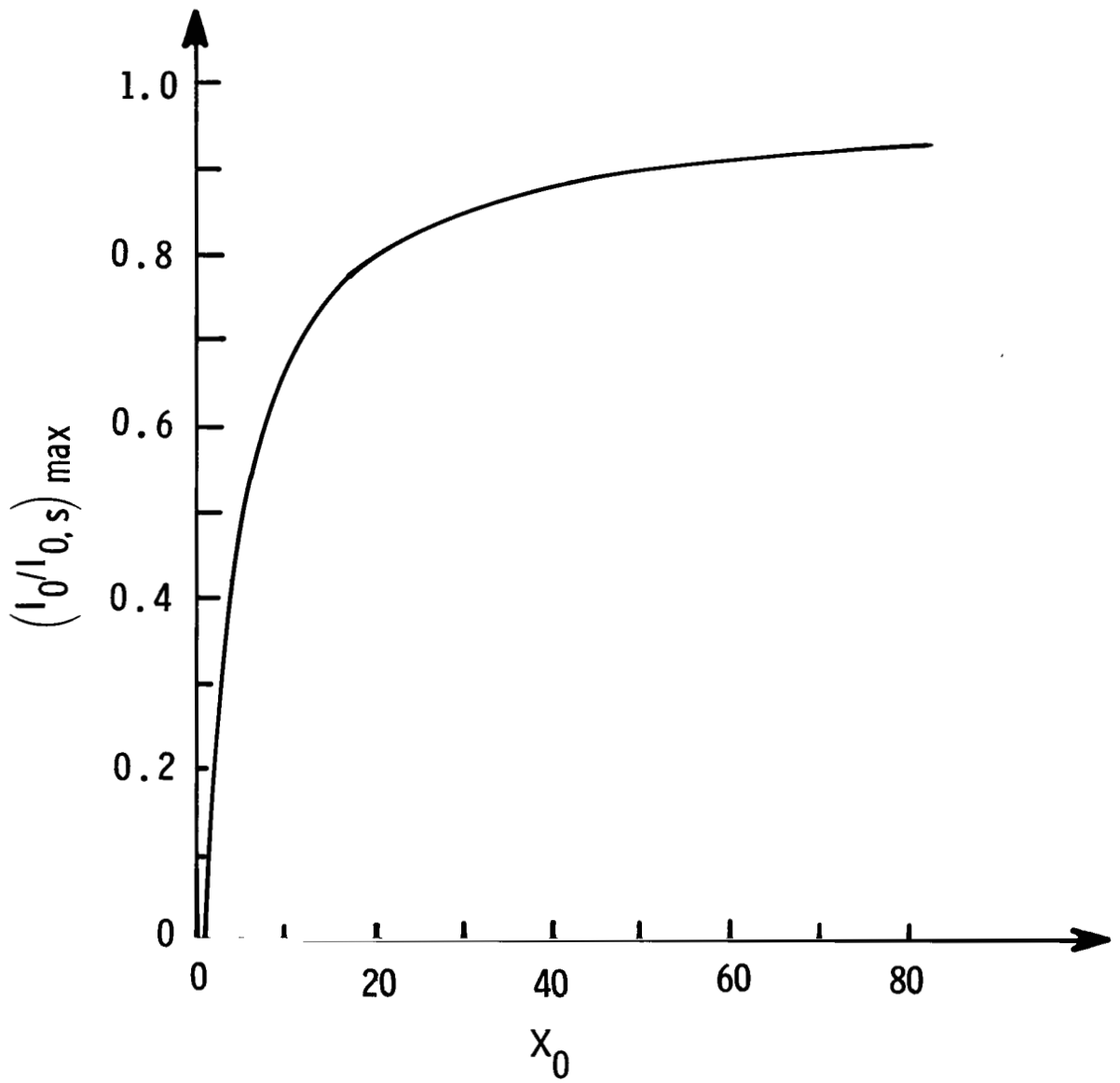

Figure 10.- Behavior of incident light intensity as a function of parameter X_0.

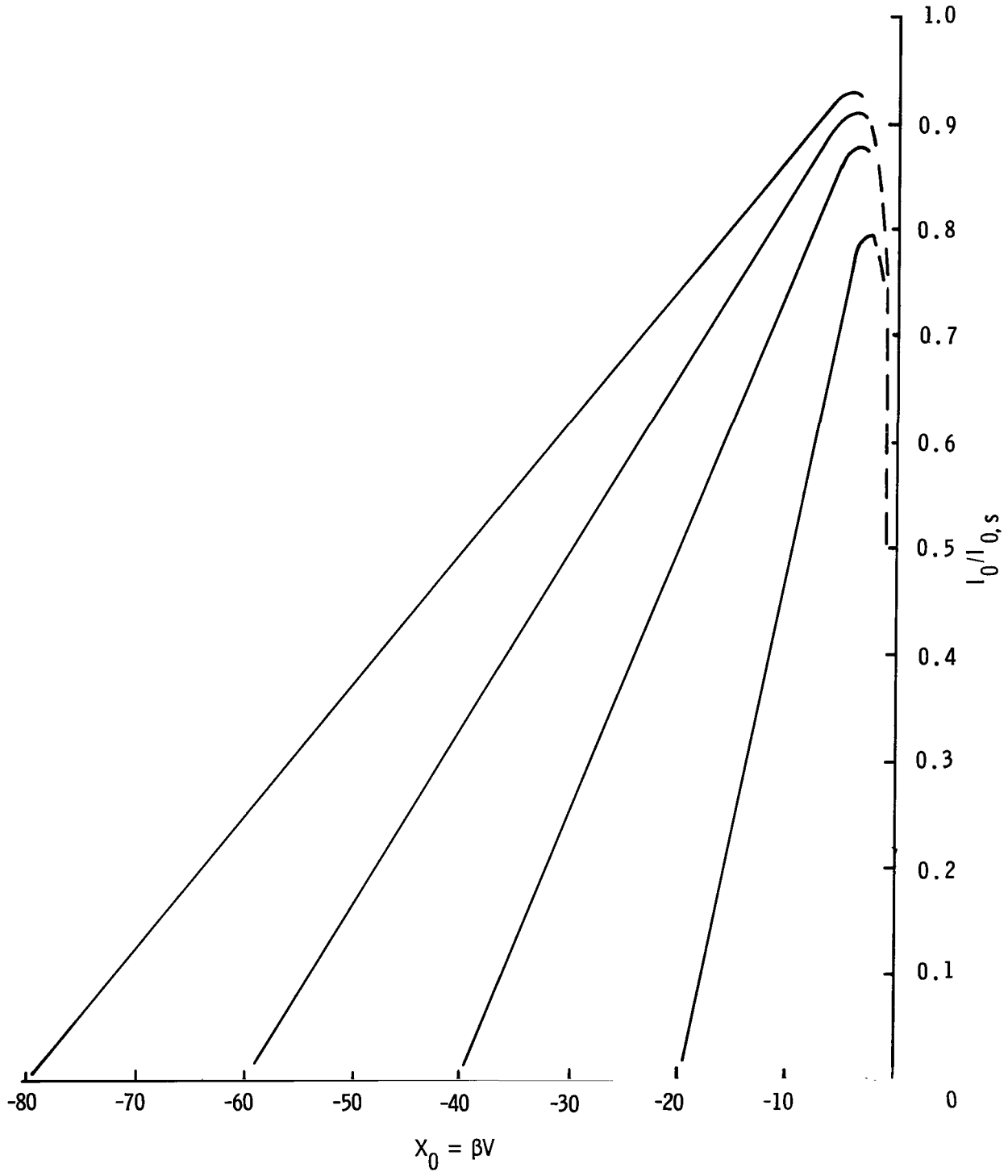

Figure 11.- Behavior of incident light intensity as a function of band-bending parameter.

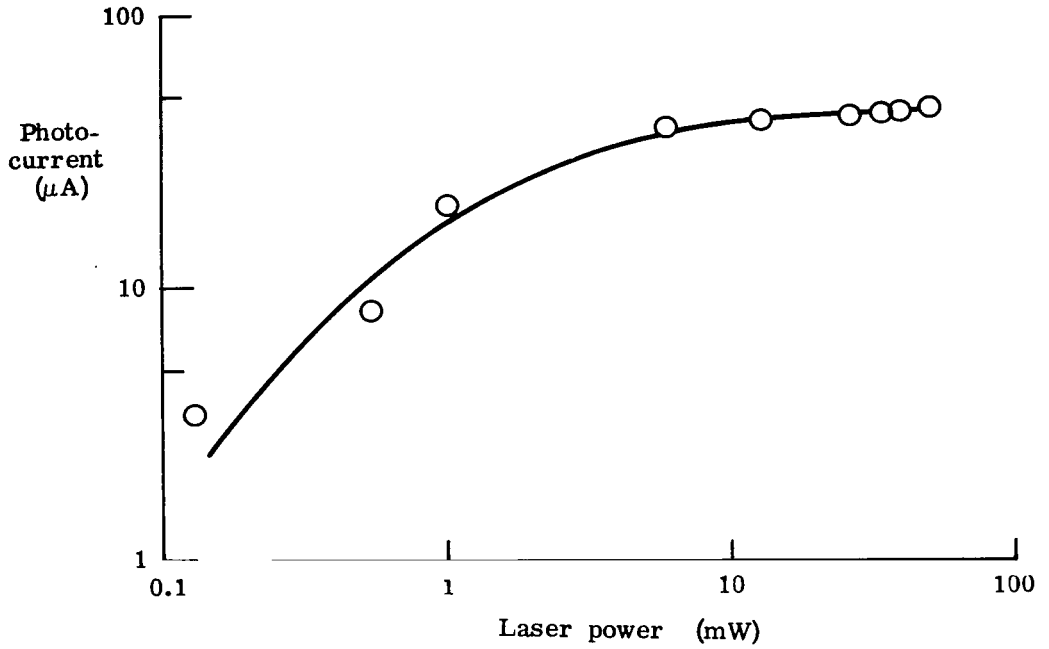

Figure 12.- Photocurrent as a function of incident laser power at 351 and 364 nm for a $SrTiO_3$-based photoelectrochemical cell showing saturation.

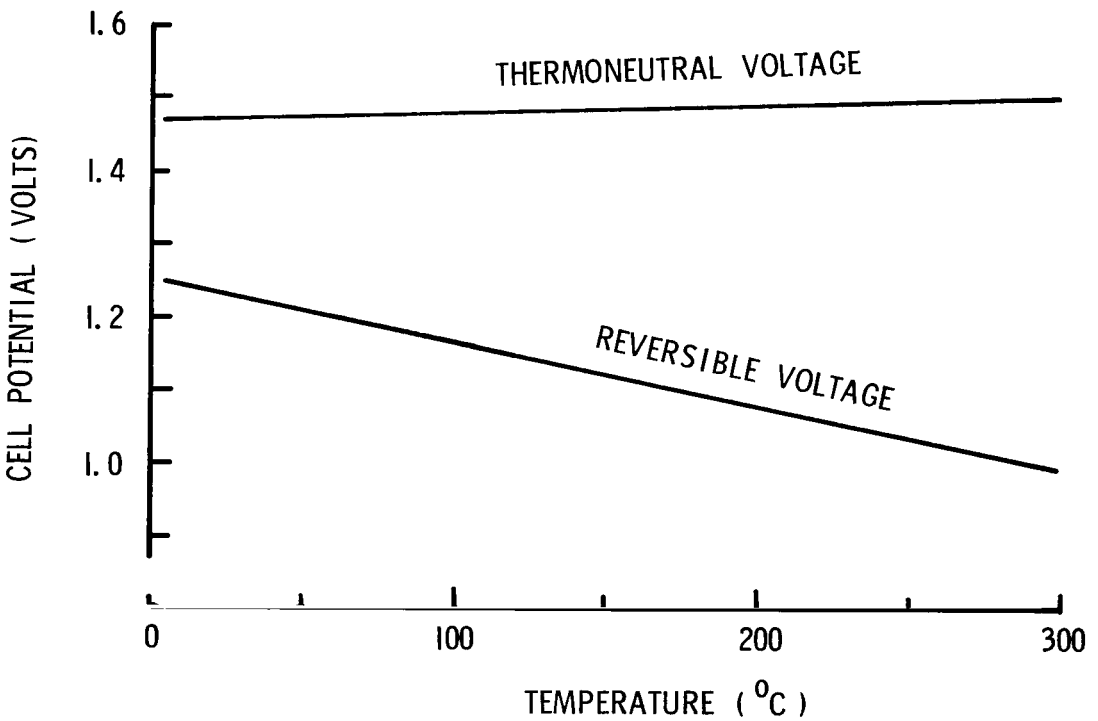

Figure 13.- Ideal electrolytic voltage for water.

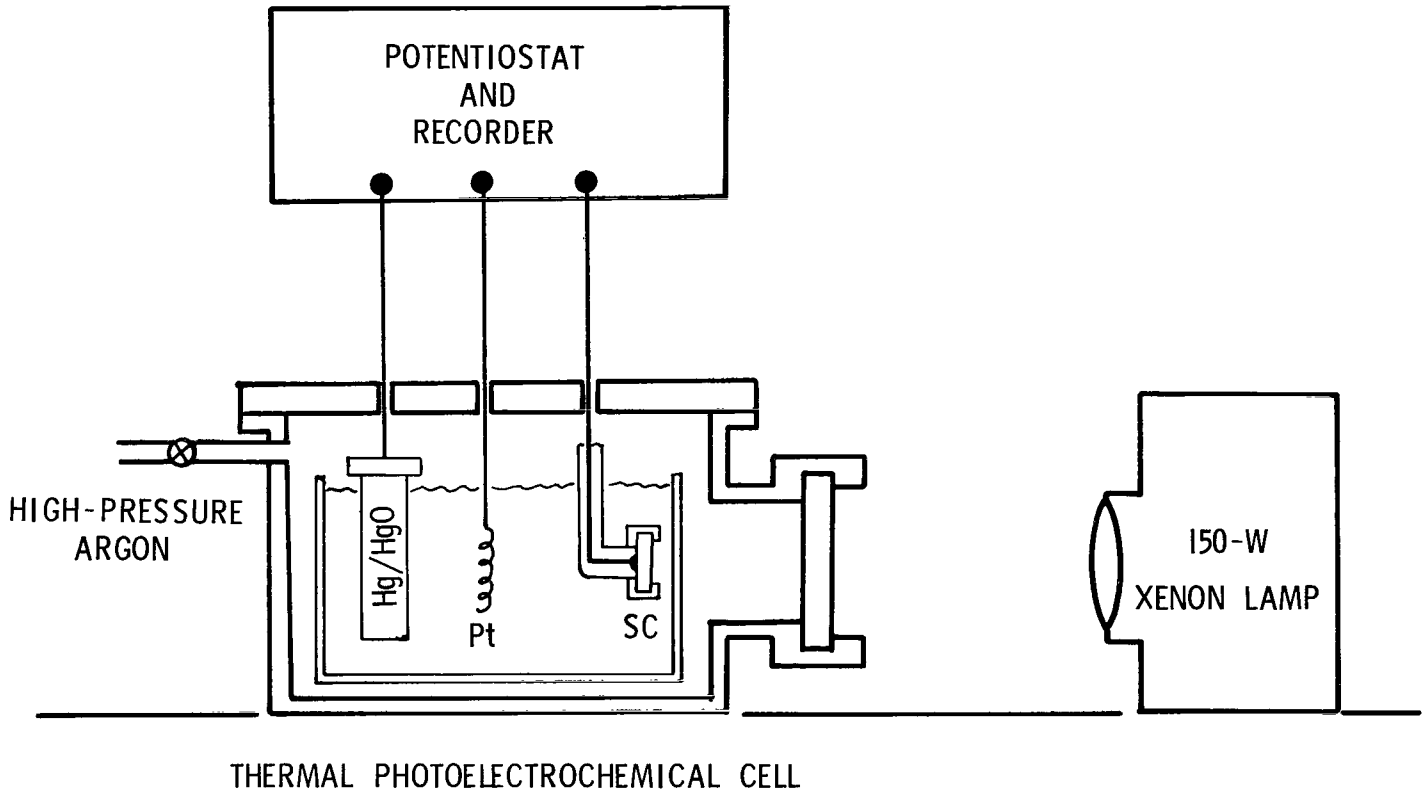

Figure 14.- Schematic of experimental setup of a thermal photoelectrochemical cell.

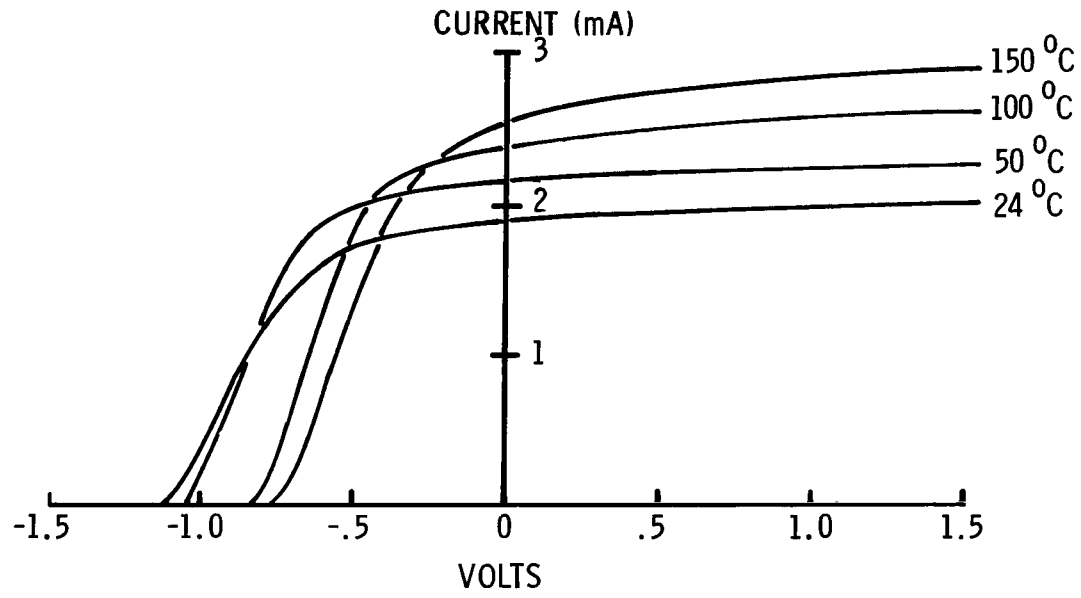

Figure 15.- Typical photocurrent-voltage curves for a $SrTiO_3$-based photoelectrolytic cell in 0.1 M NaOH for four temperatures. Potential is referenced to Hg/HgO electrode.

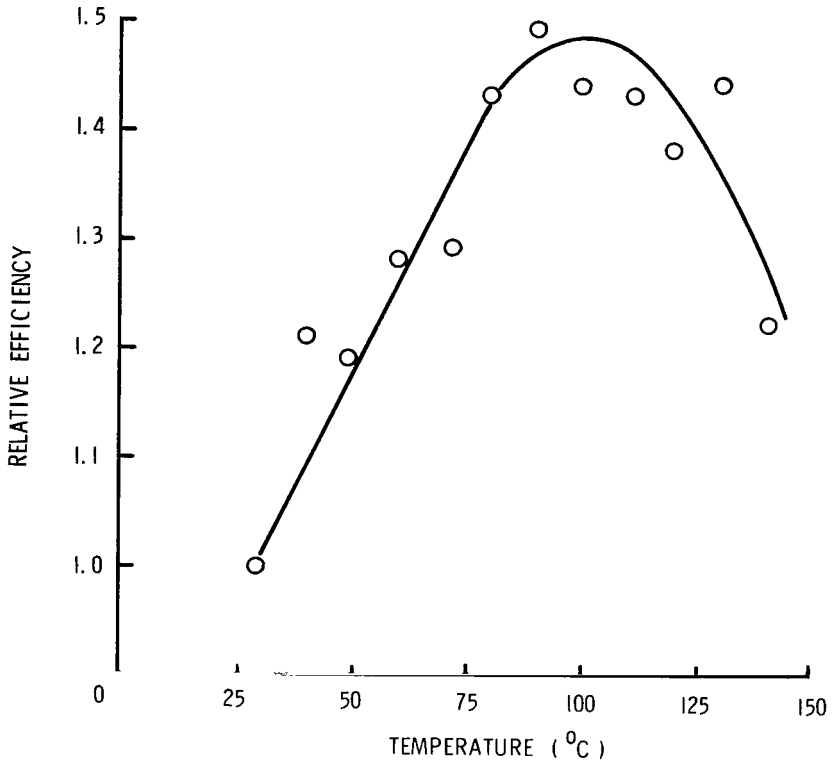

Figure 16.- Relative power conversion efficiency of an $SrTiO_3$-based photoelectrolytic cell as a function of cell temperature.

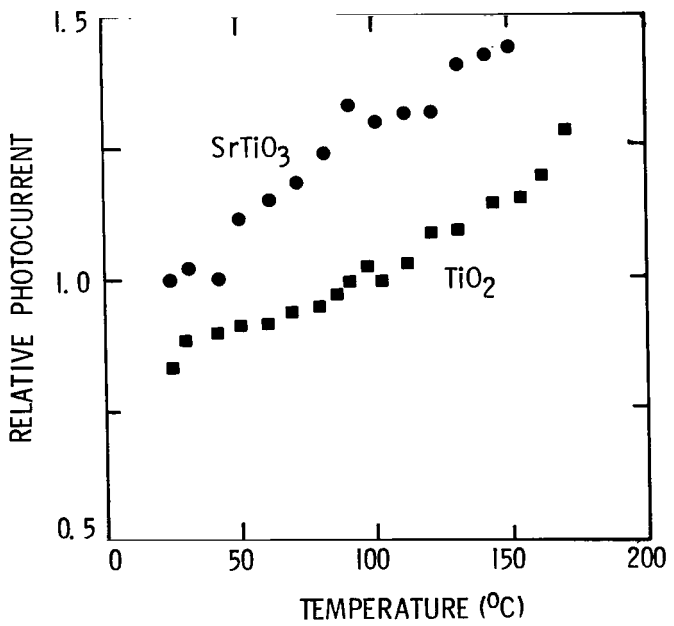

Figure 17.- Photocurrent response at 1.5 V (referenced to Hg/HgO) to broadband radiation plotted against cell temperature for $SrTiO_3$ and TiO_2 photoanodes.

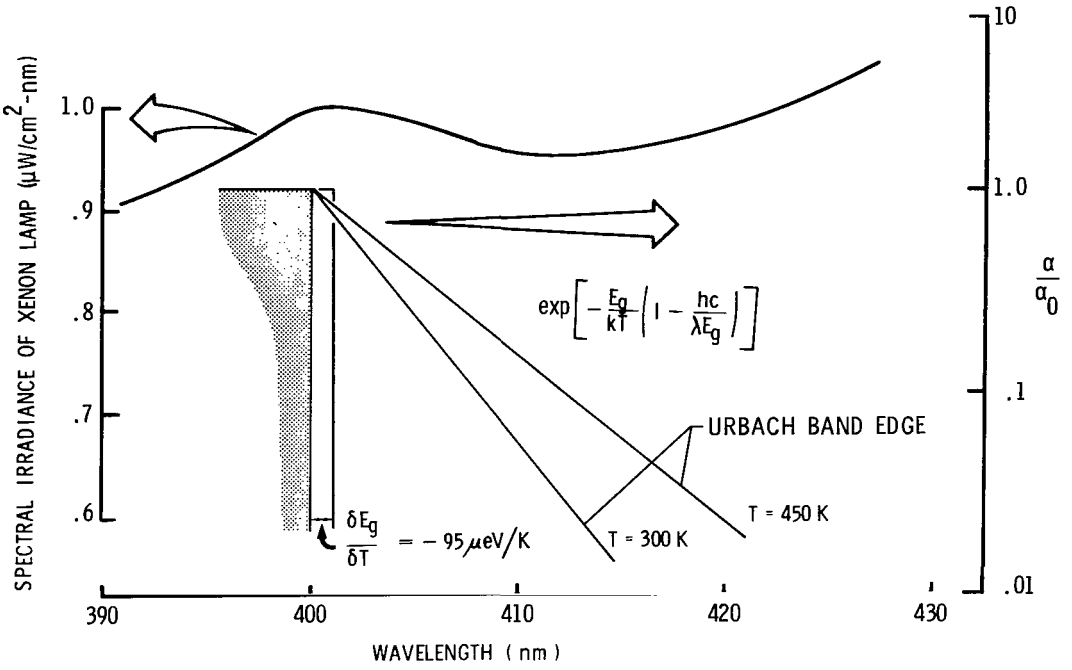

Figure 18.- Light-source spectrum and calculated thermal bandgap shift for $SrTiO_3$ at two temperatures.

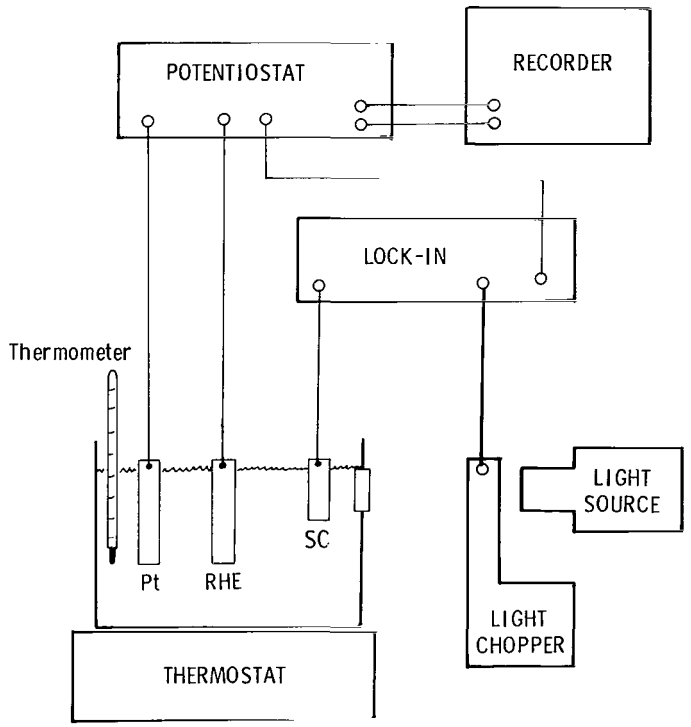

Figure 19.- Schematic of experimental setup to determine onset potential as a function of temperature.

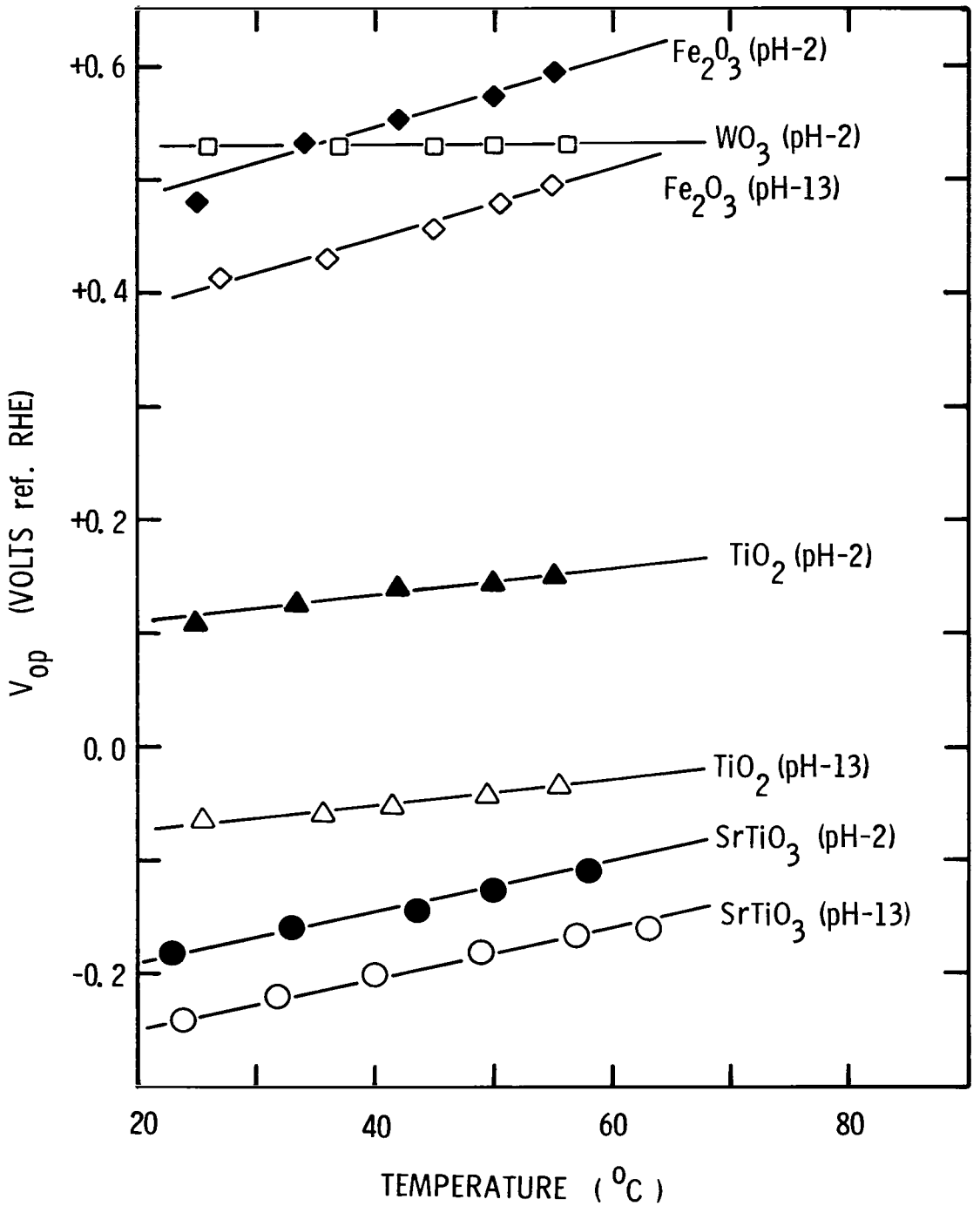

Figure 20.- Temperature dependence of onset potential for TiO_2, $SrTiO_3$, WO_3, and Fe_2O_3.

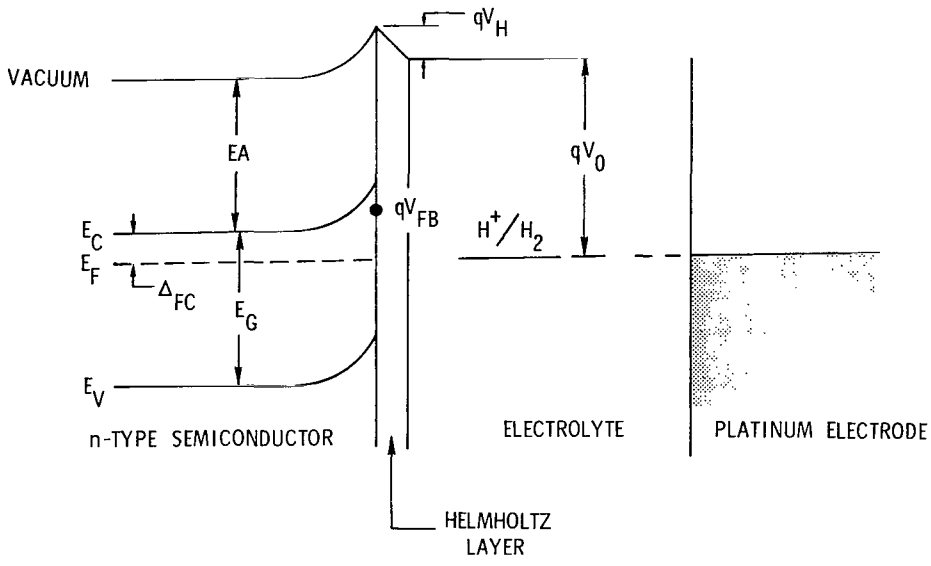

Figure 21.- Energy-level diagram for a semiconductor-electrolyte junction in equilibrium with a reversible hydrogen electrode.

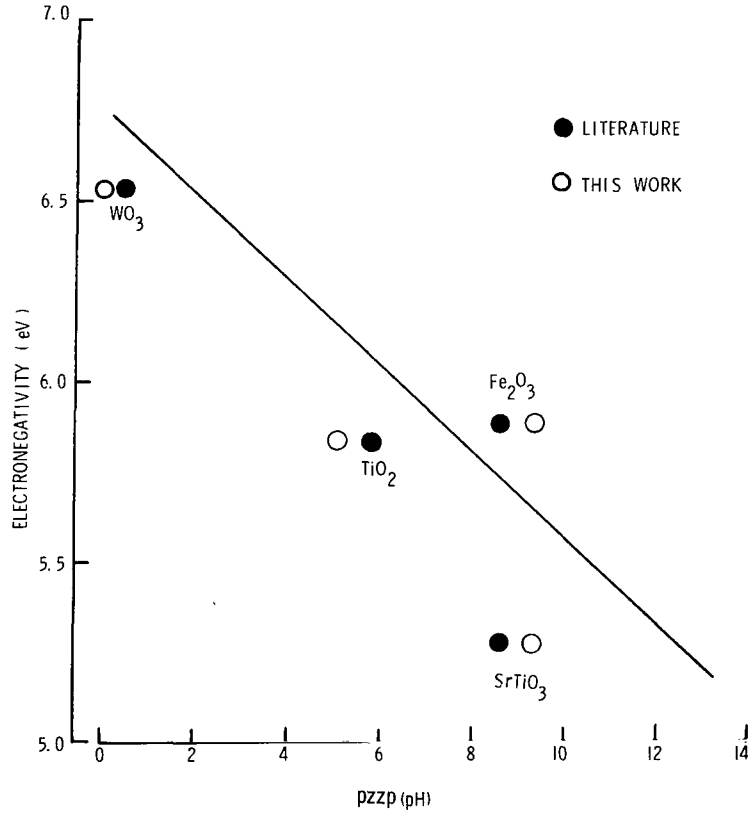

Figure 22.- Comparison of literature values of pH_{pzzp} with values determined in this work as a function of electronegativity. Curve is taken from reference 24.

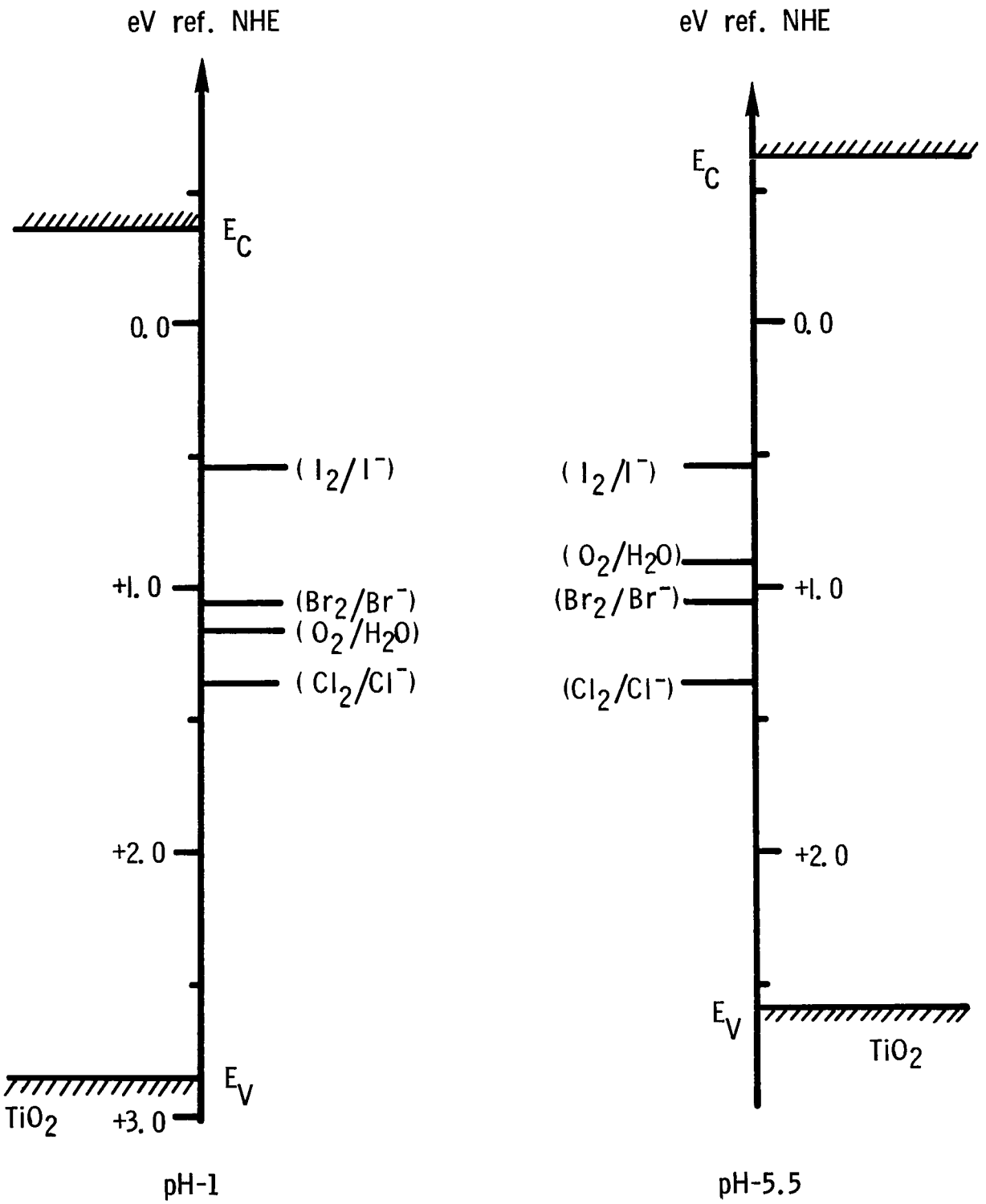

Figure 23.- Oxidation levels of halides, water, and band edges of TiO_2 at pH-1 and pH-5.5.

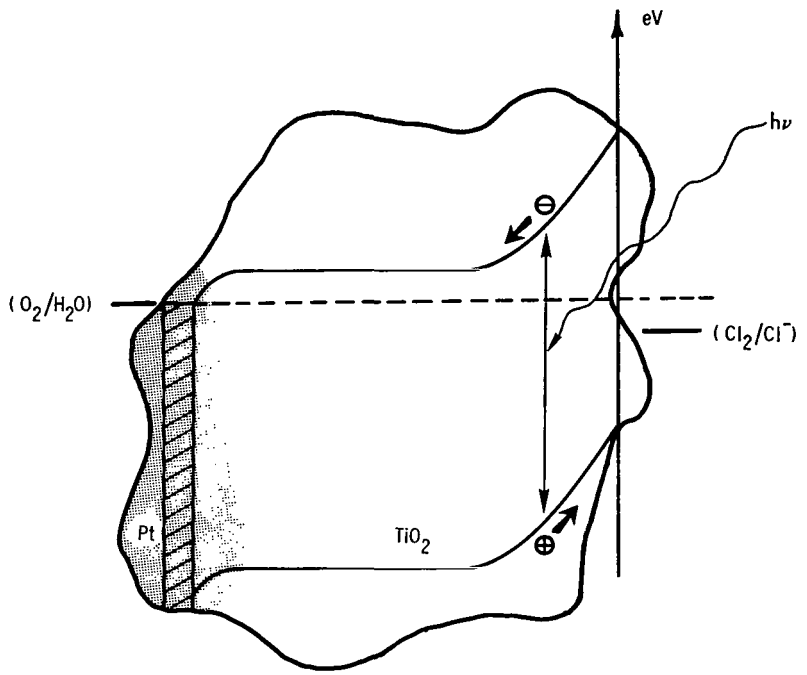

Figure 24.- Schematic of kinetics of photocatalytic production of chlorine at a platinized TiO_2 particle in an oxygen-saturated aqueous solution of chloride ion.

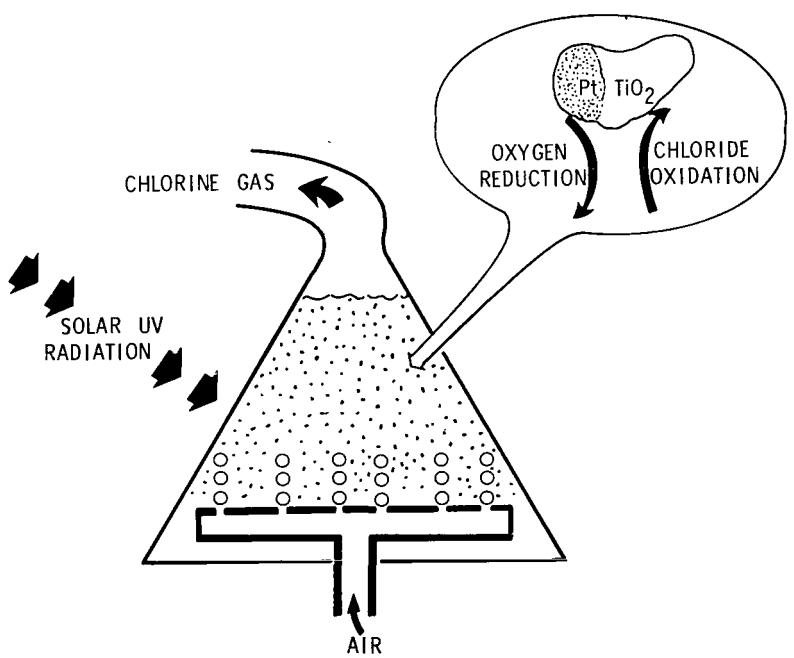

Figure 25.- Schematic of a halogen photoelectrochemical cell.

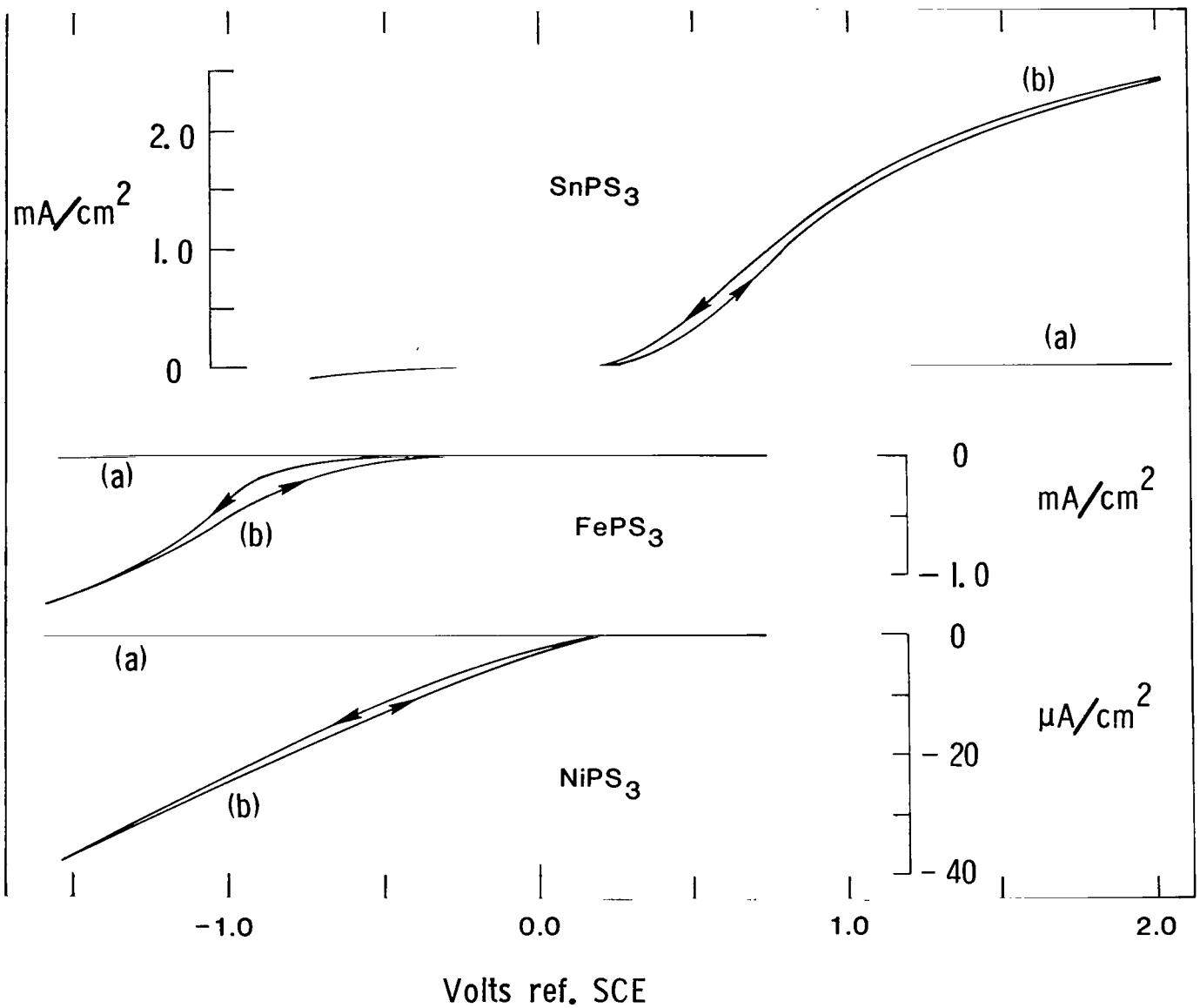

Figure 26.- Typical current-voltage response of $SnPS_3$, $FePS_3$, and $NiPS_3$ crystals in pH-2 aqueous solutions for dark current conditions (a) and under illumination (b).

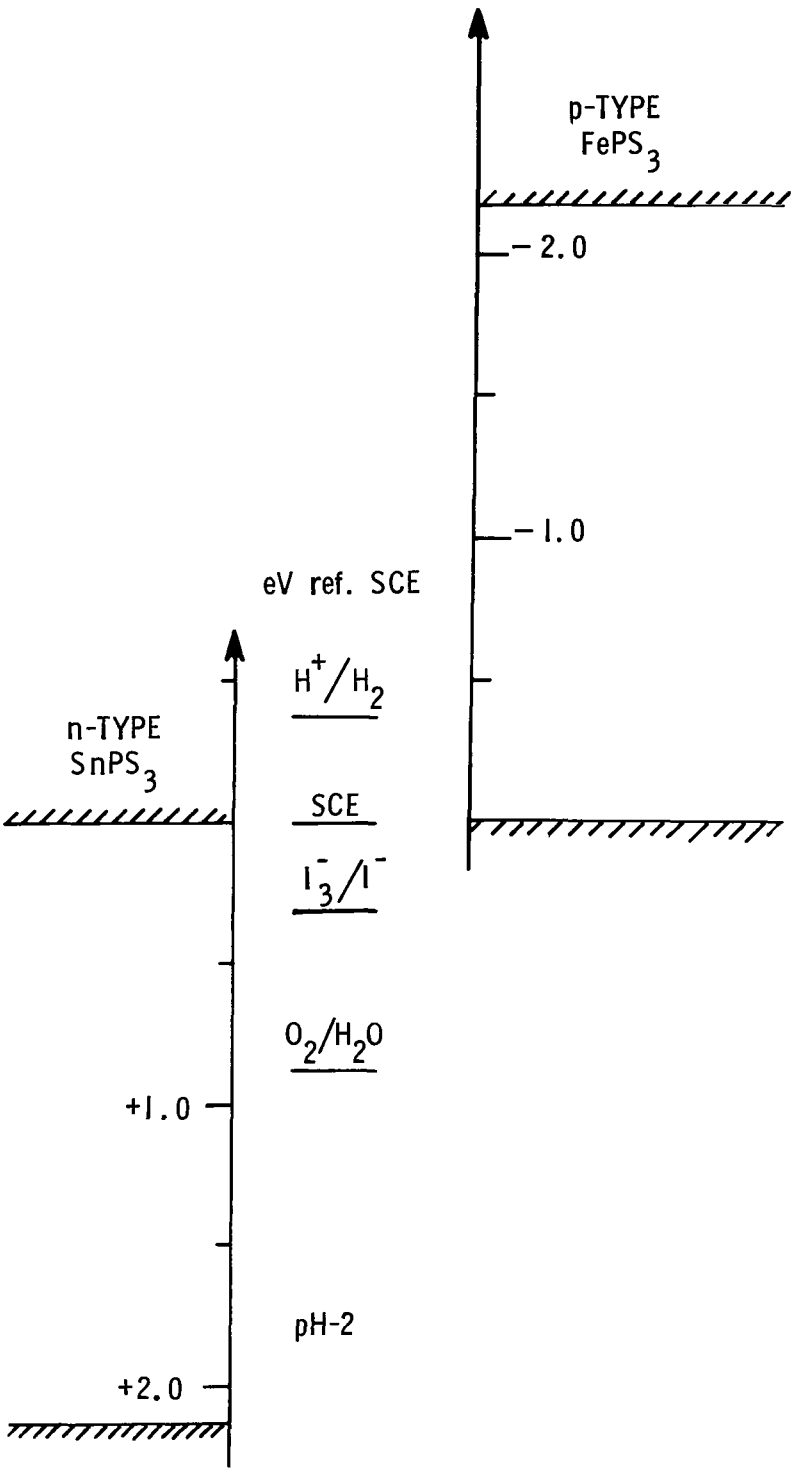

Figure 27.- Band edge of n-type $SnPS_3$ and p-type $FePS_3$ crystals in relation to redox levels of water, SCE, and the redox couple iodide and tri-iodide at pH-2.

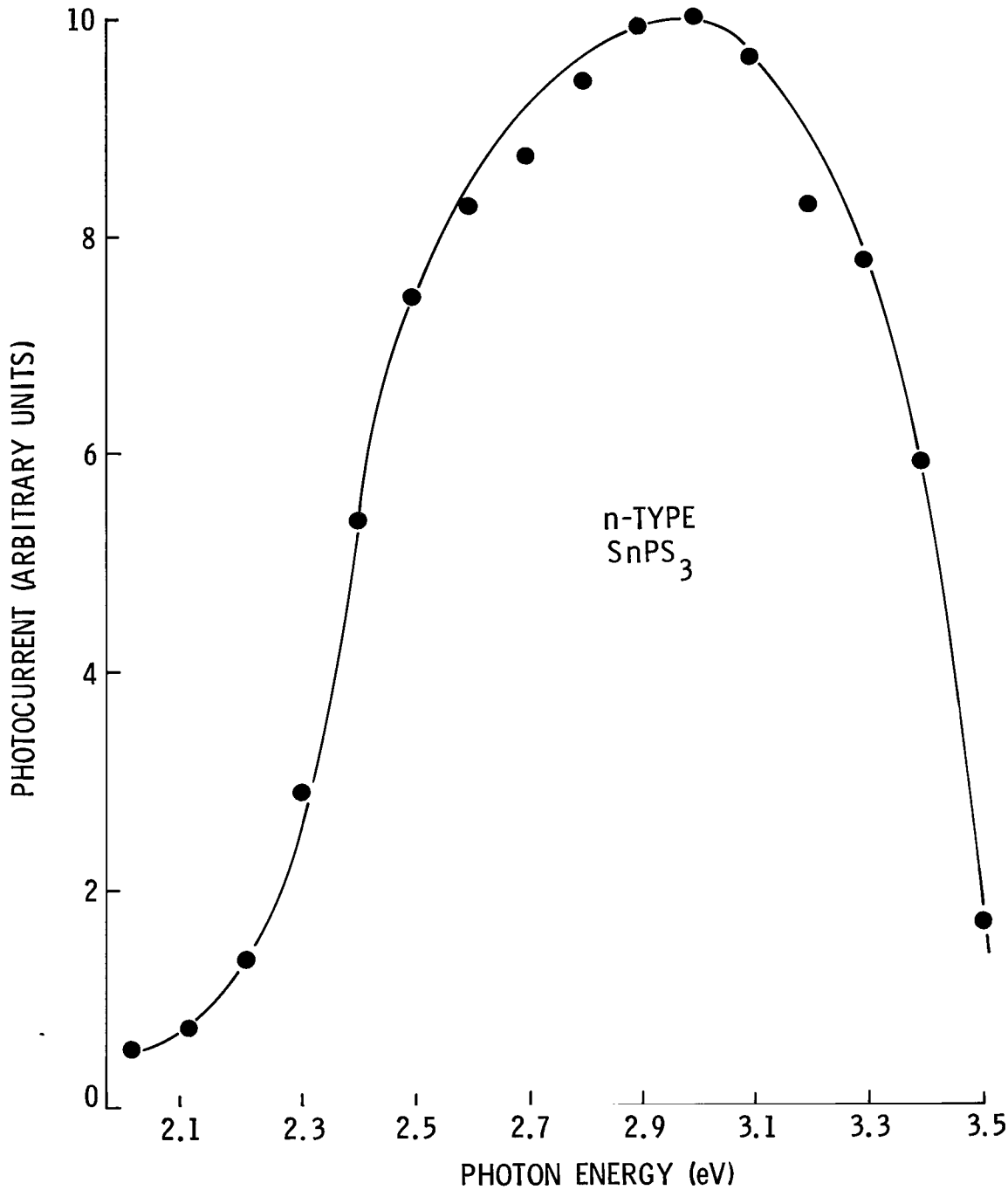

Figure 28.- Spectral photocurrent response of n-type $SnPS_3$ at 0.6 V referenced to SCE.

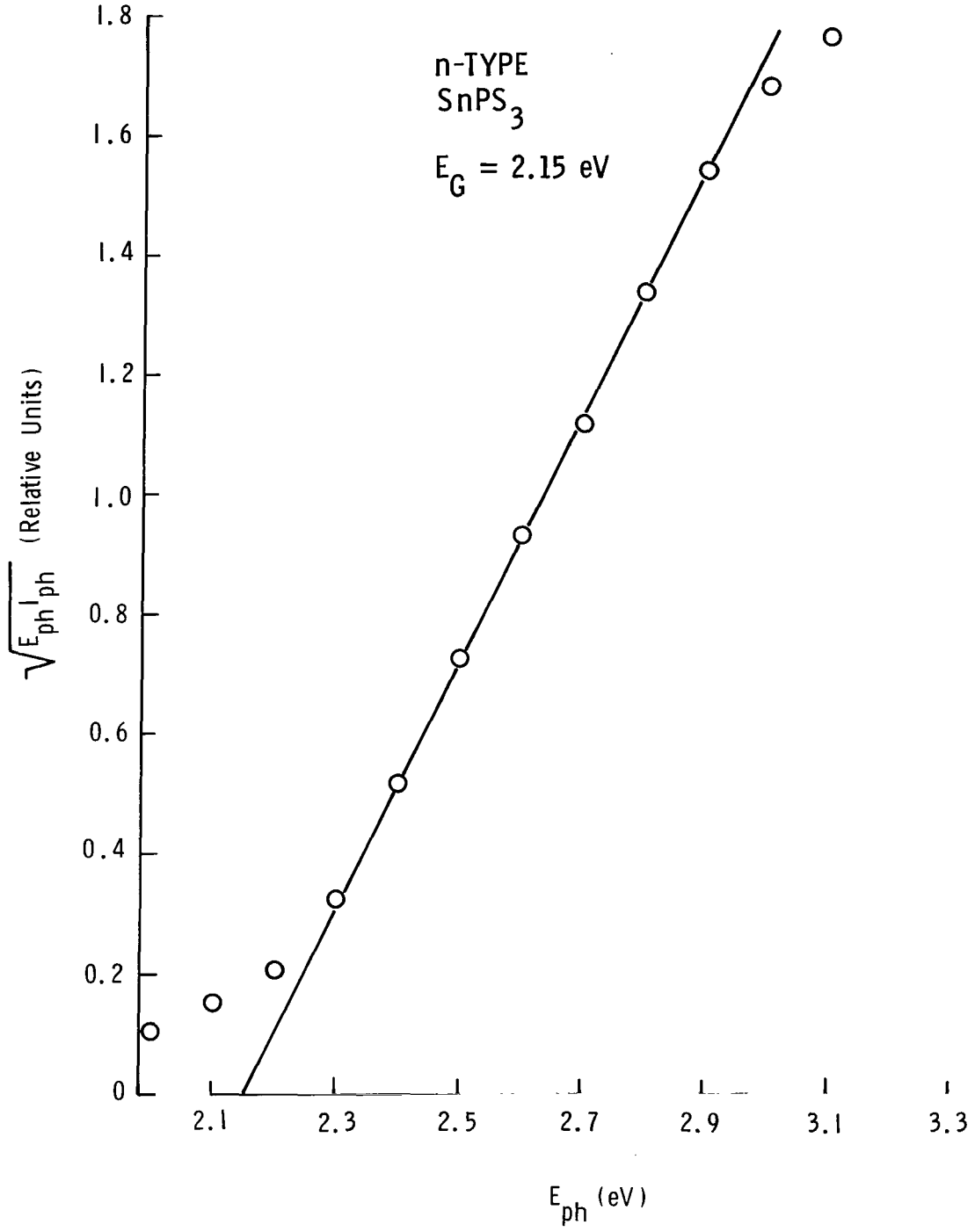

Figure 29.- Spectral photocurrent response of n-type $SnPS_3$ at 0.6 V referenced to SCE. Linear dependence indicates an indirect bandgap, and the intercept gives the bandgap energy.

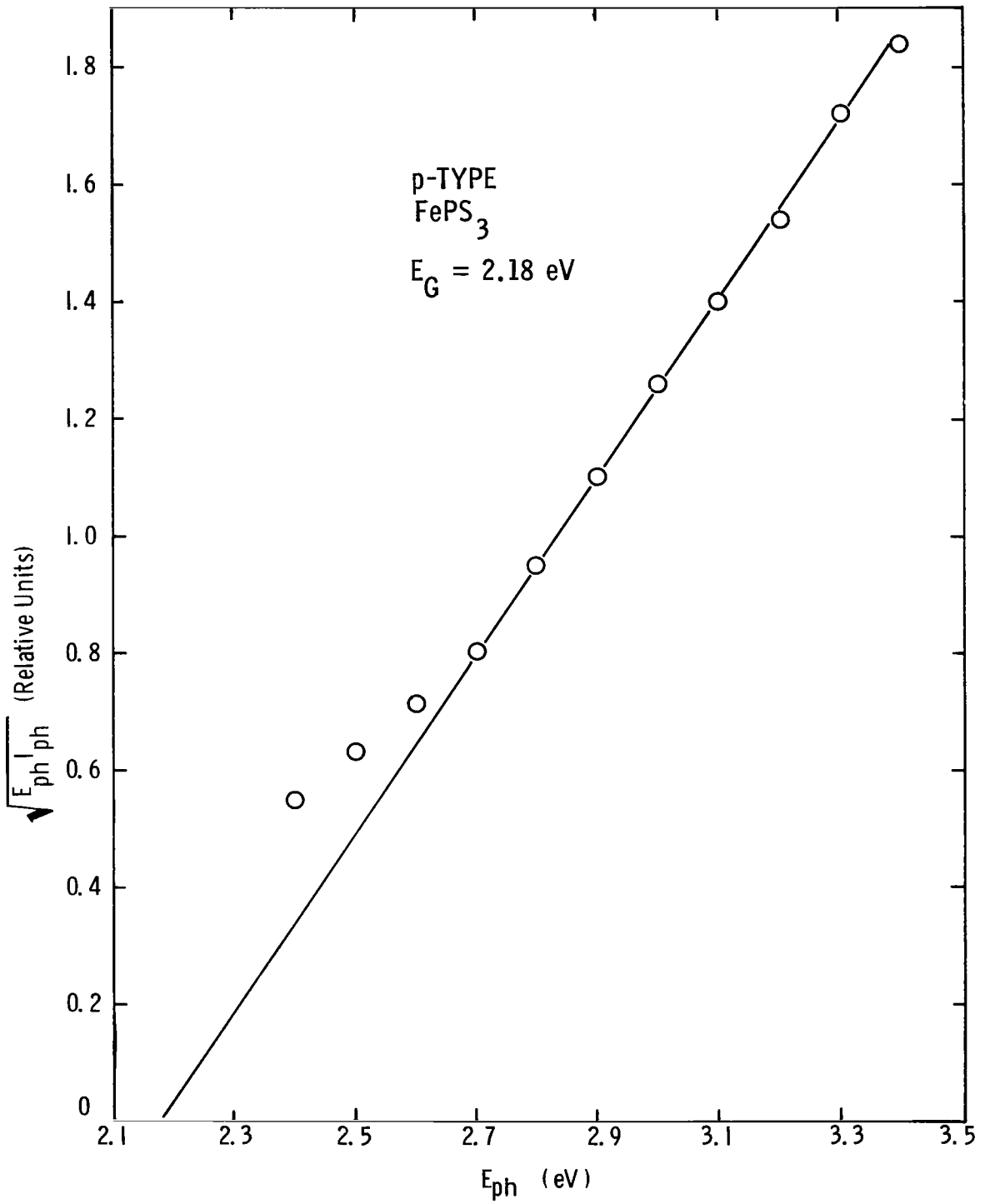

Figure 30.- Spectral photocurrent response of p-type $FePS_3$ at -1.5 V referenced to SCE. Straight-line dependence indicates an indirect bandgap, and the intercept gives the bandgap energy.

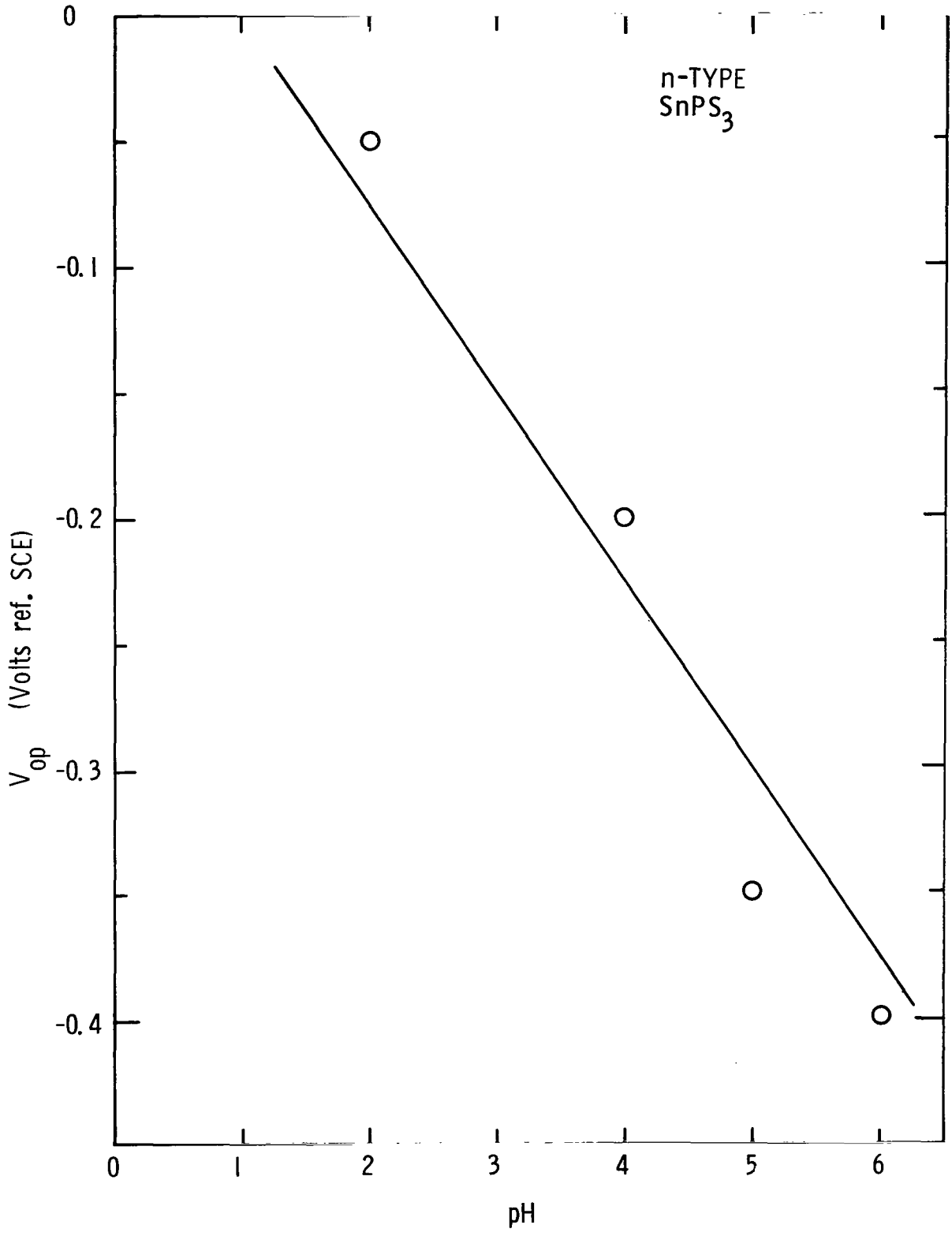

Figure 31.- Onset potential for n-type $SnPS_3$ plotted against solution pH. Slope of curve is 59 mV/pH.

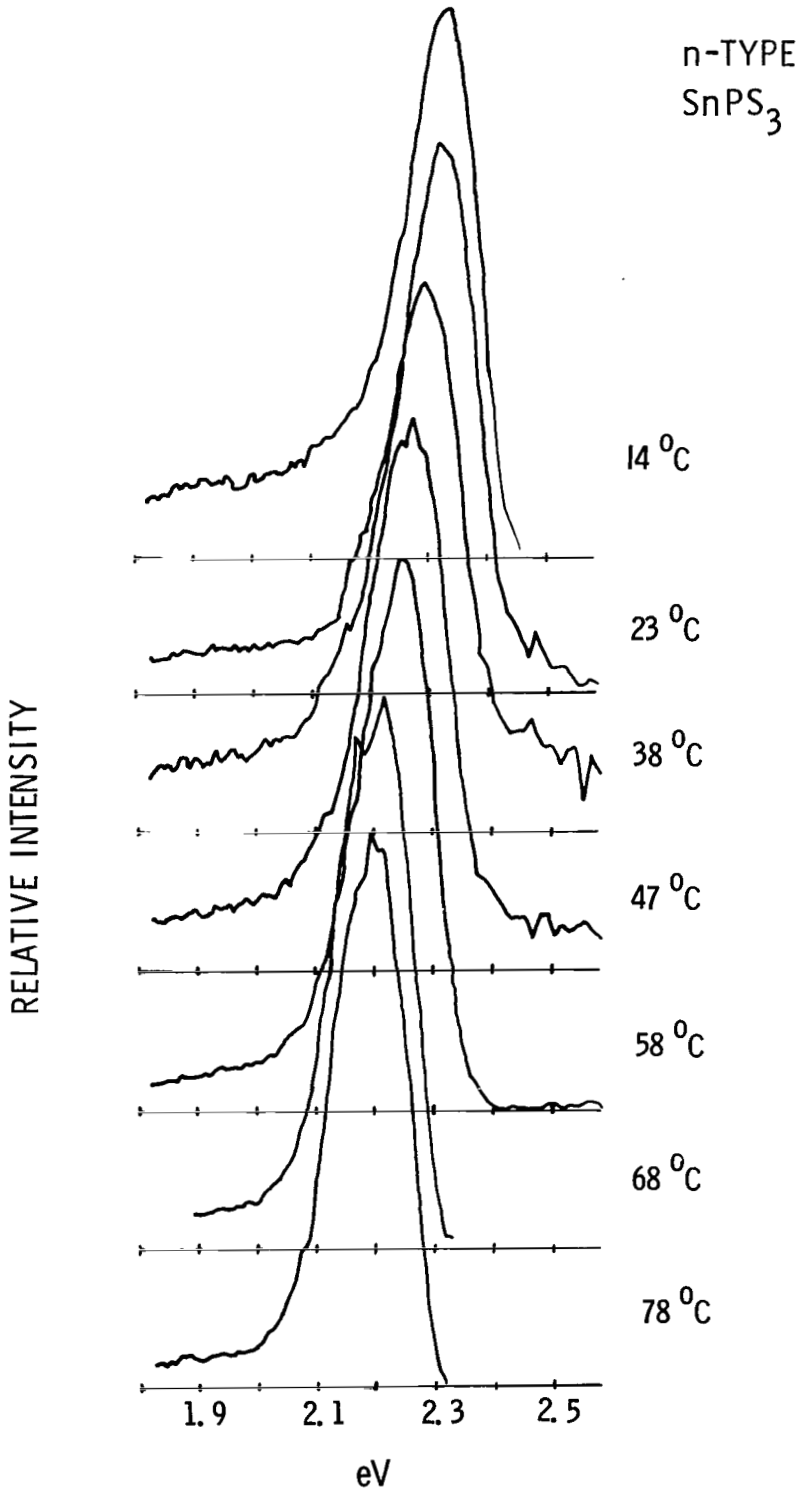

Figure 32.- Spectral response of n-type $SnPS_3$ as a function of cell temperature.

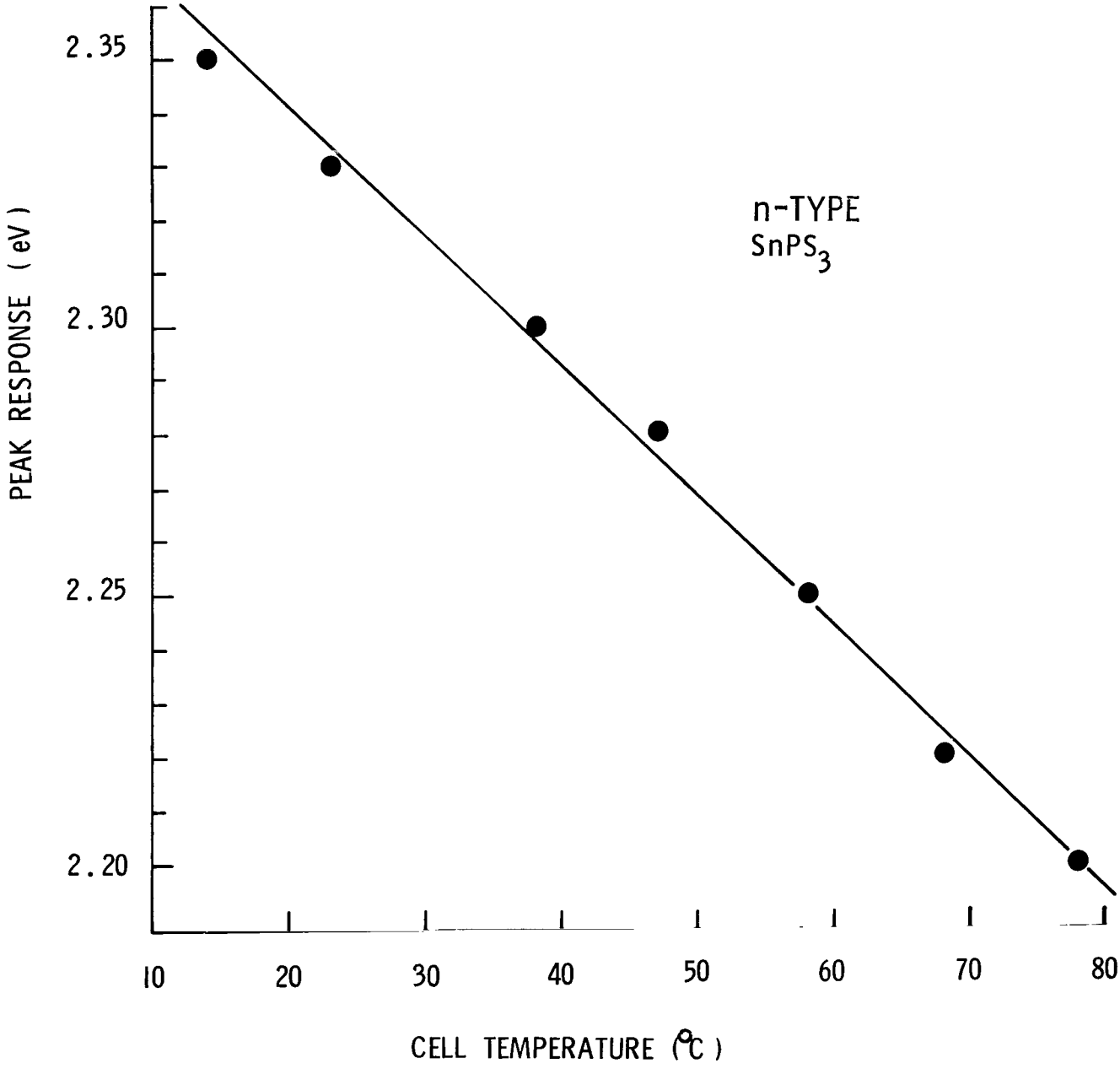

Figure 33.- Spectral response peak as a function of cell temperature for n-type $SnPS_3$.

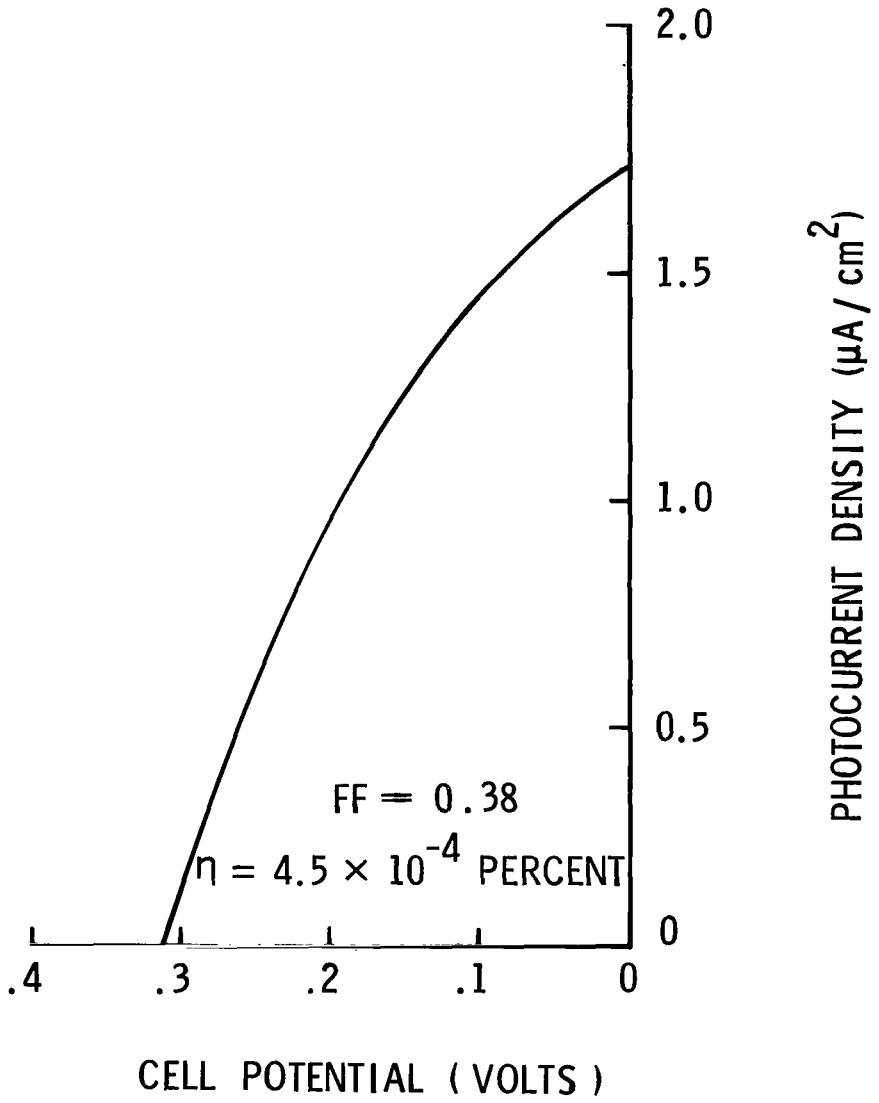

Figure 34.- Photocurrent density plotted against cell potential for n-type $SnPS_3$ in a solution of 1 M H_2SO_4, 0.025 M I_3, and 1 M I^- with a platinum counter electrode under white-light illumination.

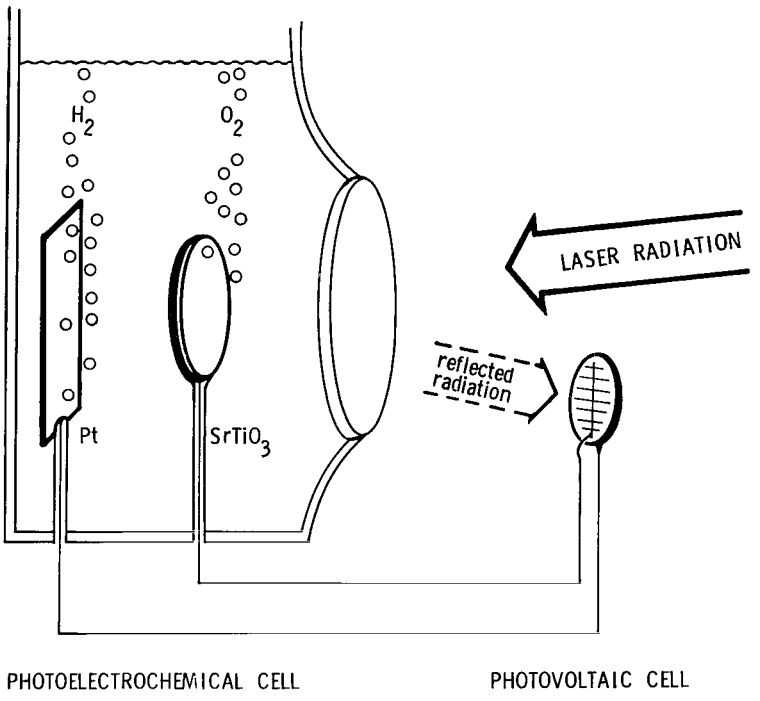

Figure 35.- Schematic of high-efficiency photoelectrolytic system for laser energy conversion.

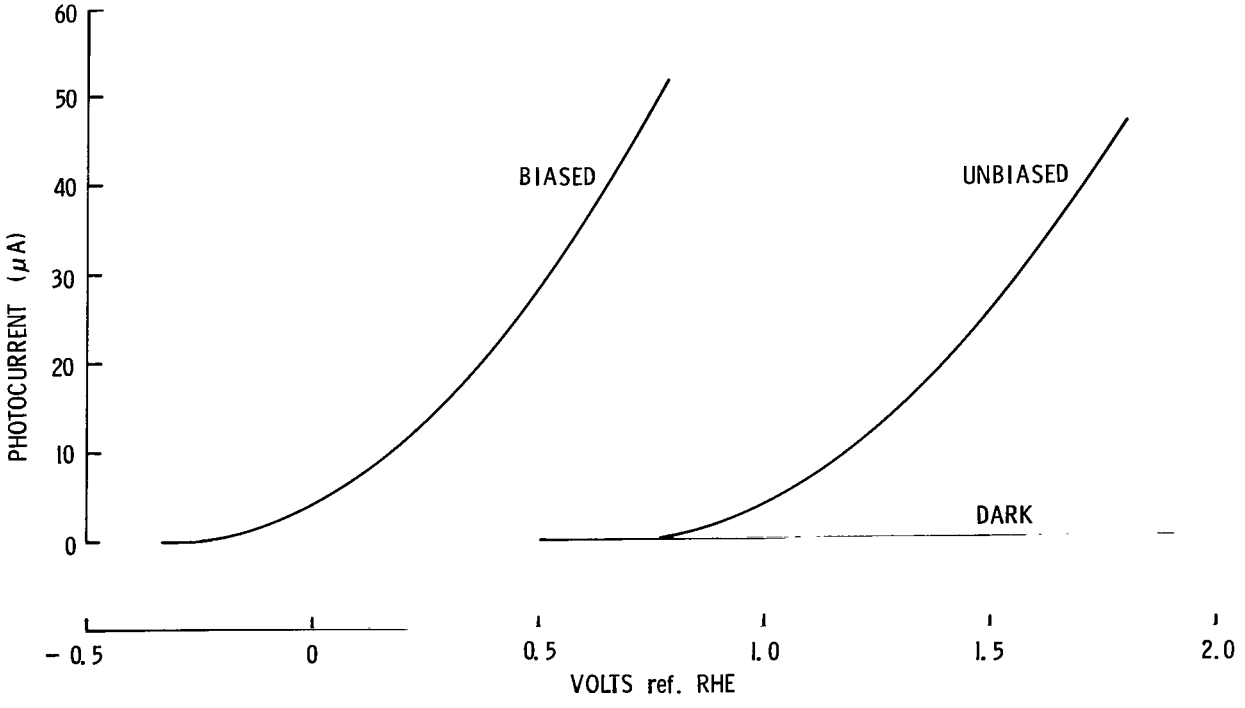

Figure 36.- Experimental current-voltage curves for an α-Fe_2O_3 based photoelectrochemical cell. Unbiased and biased by reflected radiation on a silicon solar cell.

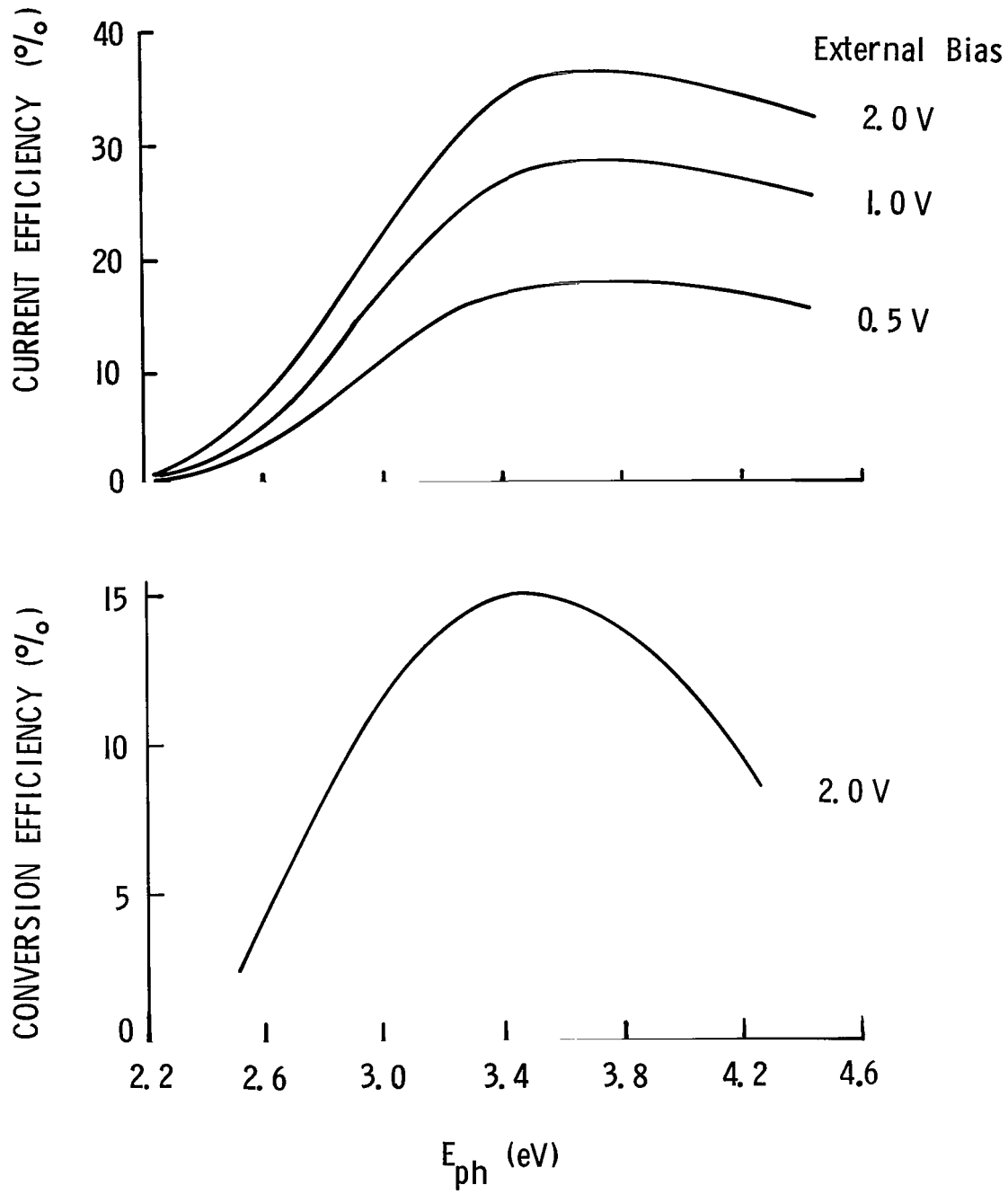

Figure 37.- Spectral current efficiency and energy conversion efficiency for α-Fe_2O_3.

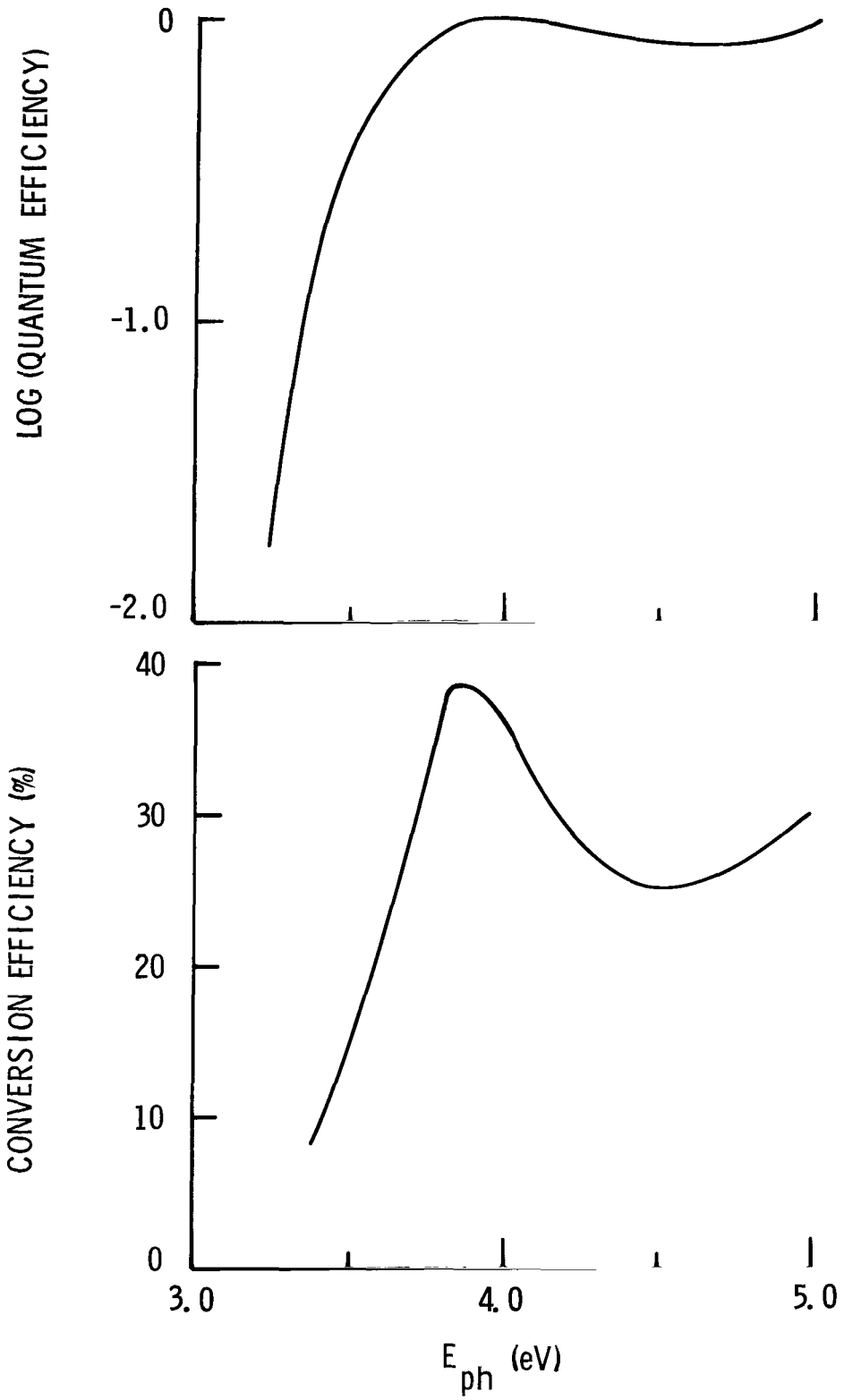

Figure 38.- Quantum efficiency and conversion efficiency as a function of incident photon energy for single-crystal $SrTiO_3$.

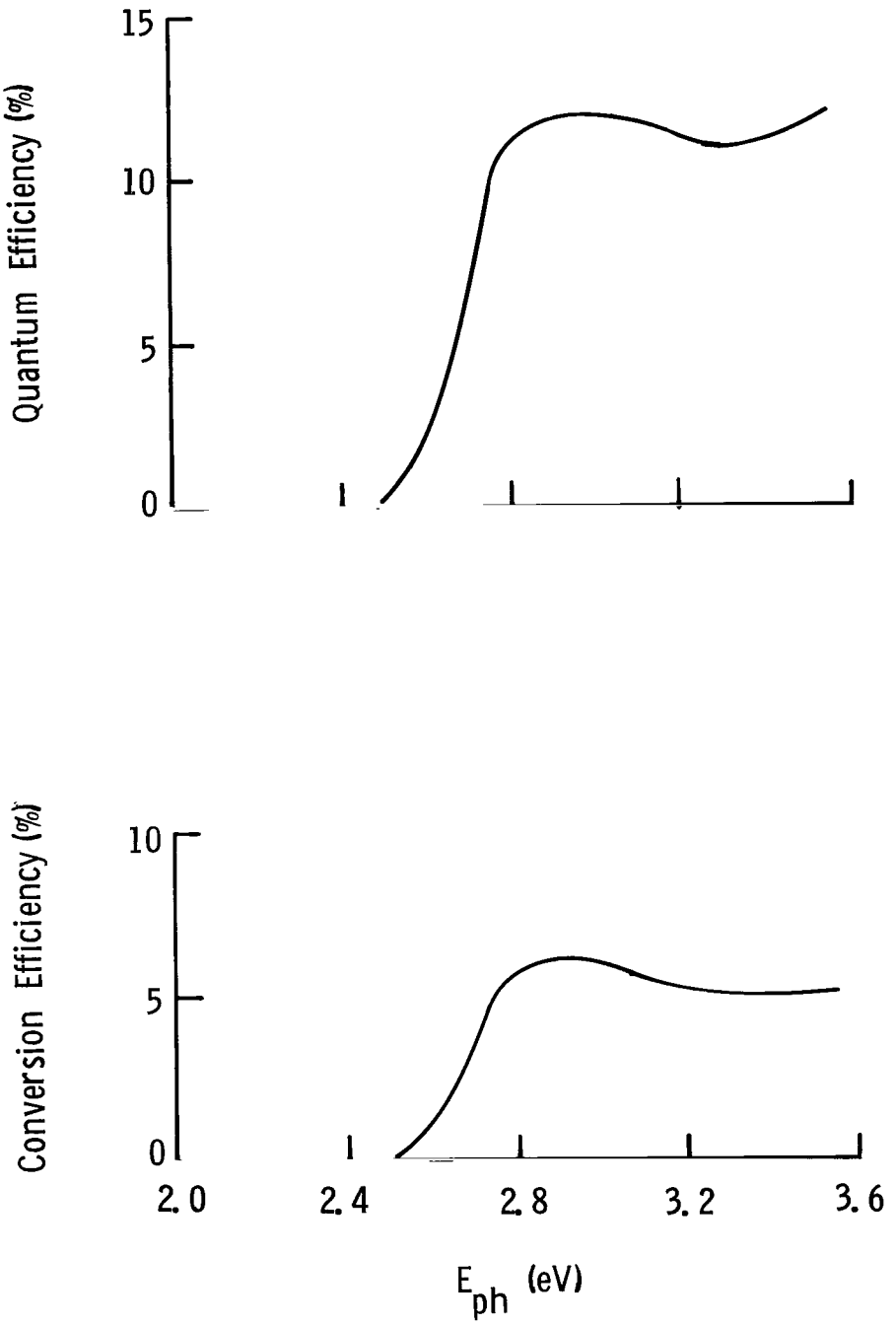

Figure 39.- Quantum and conversion efficiency for thermally grown WO_3.

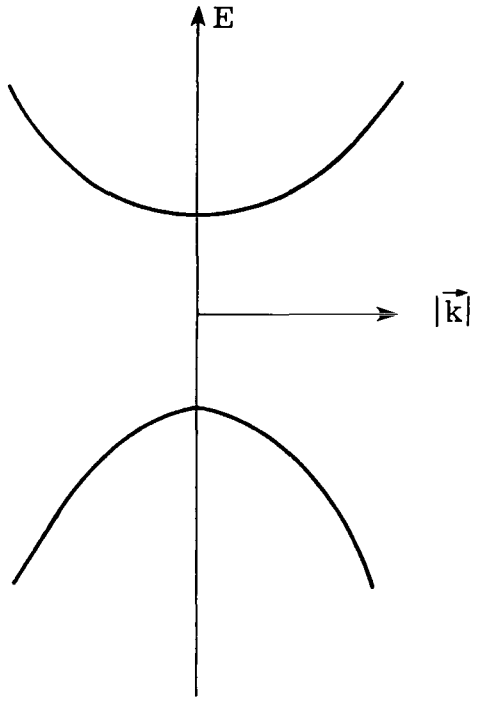

Energy-momentum relation for conduction and valence bands near their extreme values

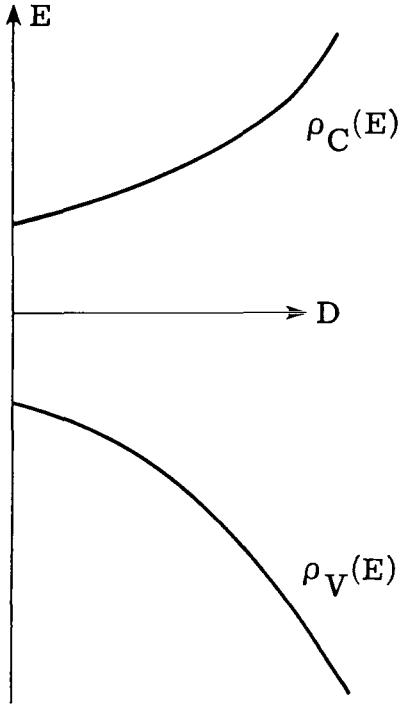

Density of electronic states near the conduction and valence band edges

Figure 40.- Conduction and valence band edges bent by deviations from charge neutrality near surface of semiconductor. Bending is depicted by plotting the energy of an electron against depth in semiconductor. Function $\phi(x)$ is a normalized potential function used to describe shape of energy curve.

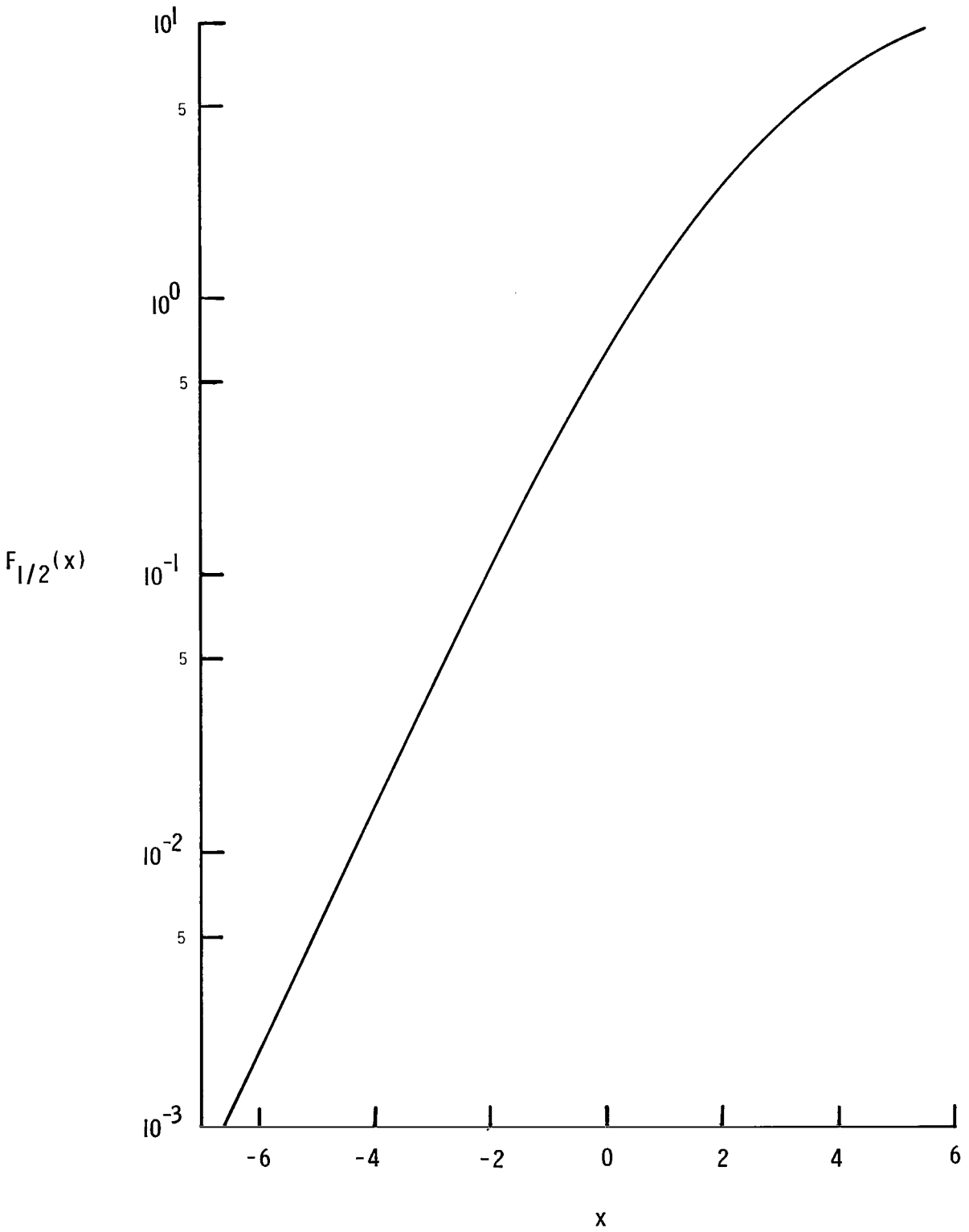

Figure 41.- Graph of Fermi integral $F_{1/2}(x)$.

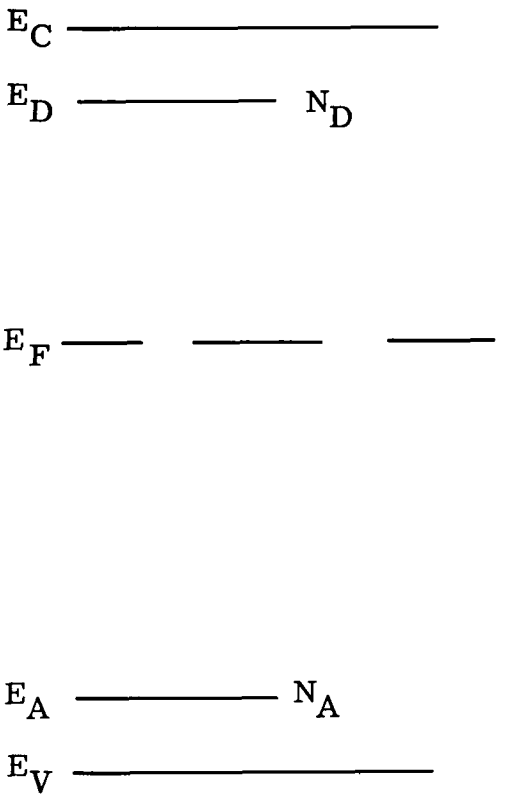

Figure 42.- Energy levels in a semiconductor showing conduction and valence bands, Fermi level, and location of donor and acceptor levels.

1. Report No.	2. Government Accession No.	3. Recipient's Catalog No.
NASA TP-2088		

4. Title and Subtitle

SEMICONDUCTOR PHOTOELECTROCHEMISTRY

5. Report Date	
January 1983	
6. Performing Organization Code	
506-55-13-03	
8. Performing Organization Report No.	
L-15495	
10. Work Unit No.	
11. Contract or Grant No.	
13. Type of Report and Period Covered	
Technical Paper	
14. Sponsoring Agency Code	

7. Author(s)
A. Martin Buoncristiani and Charles E. Byvik

9. Performing Organization Name and Address
NASA Langley Research Center
Hampton, VA 23665

12. Sponsoring Agency Name and Address
National Aeronautics and Space Administration
Washington, DC 20546

15. Supplementary Notes

A. Martin Buoncristiani: Christopher Newport College, Newport News,Virginia
work performed under NASA Grant NSG-1514.
Charles E. Byvik: Langley Research Center.

16. Abstract

Theoretical and experimental results of semiconductor photoelectrochemical research are presented. A model of the charge transport processes in the semiconductor, based on semiconductor device theory, is presented. It incorporates the nonlinear processes characterizing the diffusion and reaction of charge carriers in the semiconductor. The model is used to study conditions limiting useful energy conversion, specifically the saturation of current flow due to high light intensity. Numerical results describing charge distributions in the semiconductor and its effects on the electrolyte are obtained. Experimental results include: an estimate rate at which a semiconductor photoelectrode is capable of converting electromagnetic energy into chemical energy; the effect of cell temperature on the efficiency; a method for determining the point of zero zeta potential (pzzp) for macroscopic semiconductor samples; a new technique using platinized titanium dioxide powders and ultraviolet radiation to produce chlorine, bromine, and iodine from solutions containing their respective ions; the photoelectrochemical properties of a new class of layered compounds called transition-metal thiophosphates; and a technique used to produce high conversion efficiency from laser radiation to chemical energy.

17. Key Words (Suggested by Author(s))	18. Distribution Statement
Photoelectrochemistry Energy conversion Radiant energy conversion	Unclassified - Unlimited Subject Category 44

19. Security Classif. (of this report)	20. Security Classif. (of this page)	21. No. of Pages	22. Price
Unclassified	Unclassified	93	A05

For sale by the National Technical Information Service, Springfield, Virginia 22161 NASA-Langley, 1983

2 1 1U,E, 530125 S00903DS
DEPT OF THE AIR FORCE
AF WEAPONS LABORATORY
ATTN: TECHNICAL LIBRARY (SUL)
KIRTLAND AFB NM 87117

S